Characterisation of the anisotropic mechanical properties of carbon fibre reinforced thermoplastic composites

GA Potgieter

orcid.org/0000-0001-6229-783X

Dissertation submitted in fulfilment of the requirements for the degree *Master of Engineering in Mechanical Engineering* at the North-West University

Supervisor: Mr CP Kloppers

Co-supervisor: Dr JJ Janse van Rensburg

Graduation ceremony: May 2019

Student number: 23449810

ACKNOWLEDGEMENTS

I would first like to thank my LORD and saviour Jesus Christ who died for me on the cross, went to hell and rose again on the third day, and in doing so paid the price that I was supposed to pay for my sins (1 Corinthians 15:1-4). Now that I am saved He lives in me and gave me the opportunity and strength to complete this study.

Secondly, I would like to thank Prof DJ de Beer, Chief Director: Technology Transfer and Innovation Support Office at the North-West University Potchefstroom campus for providing me with a bursary for two years from the Collaborative Programme in Additive Manufacturing to complete my studies. Thanks are given also to the North-West University for their master degree student bursary.

I would also like to thank my dissertation advisors Mr CP Kloppers and Dr J.J. Janse van Rensburg of the Faculty of Mechanical Engineering at the North-West University Potchefstroom campus. They were always available whenever I had a question about my research or writing.

I also would like to acknowledge the Faculty of Mechanical Engineering' laboratory manager, Mr Sarel Naude, and his workshop assistant, Mr Thabo Diobe, for their support and helping hands whenever I needed them. Thank you to Dr Anine Jordaan, senior subject specialist at the laboratory for Electron Microscopy Chemical Recourse Beneficiation (CRB) at the Potchefstroom campus of the North-West University for her support with the SEM pictures.

Finally, I must express my gratitude to my loving parents (Gustav and Henna), to my kind-hearted sister (Mardi), and to my wonderful wife (Lineke) for providing me with dependable support and continuous inspiration throughout my years of study and the process of researching and writing this dissertation. This accomplishment would not have been possible without them. Thank you.

ABSTRACT

Fused filament fabrication (FFF) is an additive manufacturing (AM) process of creating solid, three-dimensional objects from a digital file. During this additive process an object is created by laying down successive layers of material (thermoplastic filament) until the entire object is formed. Each of these layers can be seen as a thinly sliced, horizontal cross-section of the final object [1]. A technology called *continuous fibre fabrication* or *composite filament fabrication* (CFF) ensures reinforcement of these objects by means of in-layer fibre AM.

This CFF technology is prominent at Markforged Inc., where reinforced fibres (carbon, fibreglass or Kevlar) are thoroughly ironed against core materials such as nylon or onyx. From this definition it may appear evident that classical laminate theory (CLT) should be used for the simulation and analysis purposes of these kinds of composites. An investigation was done on the anisotropic effects (specifically carbon fibre with nylon) and was compared with the CLT by means of the Laminated Analysis Program, and the results are thought-provoking.

The findings revealed that the CFF technology can be seen as a composite material only for a unidirectional layout combination. For all other combinations a new database was created together with a proposed mathematical model to predict the material properties with different fibre angle combinations. The experimental data in this model revealed an average percentage error of only 9.4 with seven different layout combination categories.

Keywords: Anisotropic material; Carbon fibre; Characterisation; Classical laminate theory; Composites; Continuous fibre fabrication; Fibre-reinforced thermoplastic composites; Laminated Analysis Program; Markforged Mark Two; Material properties; Mathematical modelling; UTS prediction.

TABLE OF CONTENTS

LIST OF TABLES

LIST OF FIGURES

LIST OF ABBREVIATIONS

ABS	Acrylonitrile butadiene styrene
AM	Additive manufacturing
ASTM	American Society for Testing and Materials
CFF	Continuous fibre fabrication / Composite filament fabrication
CFR	Continuous fibre reinforcement
CFRTP	Continuous fibre-reinforced thermoplastic
CLPT	Classical laminated plate theory
CLT	Classical laminate theory
FDM	Fused deposition modelling
FFF	Fused filament fabrication
FRTP	Fibre-reinforced thermoplastic
HTGF	High-temperature glass fibre
LAP	Laminated Analysis Program
NWU	North-West University
PAN	Polyacrylonitrile
PLA	Polylactic acid
SEM	Scanning electron microscope
TLCP	Thermotropic liquid crystal polymers
UCS	Ultimate compression strength
UTS	Ultimate tensile strength
VAS	Visual analogue scale
YS	Yield strength

CHAPTER 1

INTRODUCTION

Although there exist numerous additive manufacturing processes of rapid prototyping, only the fused filament fabrication (FFF) / fused deposition modelling (FDM) together with the continuous fibre fabrication (CFF) process is discussed in this chapter, as these are the main focal point of the whole dissertation.

1.1 Background

Fused filament fabrication (FFF) is an additive manufacturing (AM) process of creating solid, three-dimensional objects from a digital file. During this additive process an object is created by laying down successive layers of material (thermoplastic filament) until the entire object is formed. Each of these layers can be seen as a thinly sliced, horizontal cross-section of the final object [1]. A technology called *continuous fibre fabrication* or *composite filament fabrication* (CFF) ensures reinforcements of these objects by means of in-layer fibre AM. One machine that operates using this technology is the Markforged Mark Two printer.

Optimising any component design in AM requires investigating the interior structural properties together with the printed material. The interior structures can be explained as the pattern by which an object is being manufactured layer by layer with the toolpath in the same way one would use a piping bag to decorate a cake with icing. These patterns include a honeycomb, grid, concentric, and triangular pattern to name but a few. In the same way that a baker uses their own creativity to decorate a cake, an FFF machine's toolpath can also be controlled according to the user's desired infill pattern.

The most applicable method for determining the basic material property data for component design and service performance assessment is tensile testing [2–8], which has been selected as the testing method to achieve the objectives set out for this investigation project.

1.2 Problem statement

During the design process of any engineering project, the material properties must be known before any simulation or analysis can be executed. This is especially true when it comes to designing for additive manufacturing. Due to the relatively young AM industry (compared with the more traditional manufacturing processes), most of the material properties are not yet known. The same is true for the Markforged Mark Two and its CFF technology, which makes accurate and proper designing problematic. No characterisation of mechanical properties in respect to the

reinforced material (carbon fibre) exists. Furthermore, it is not clear whether or not this new technology complies with the usual laminate composite theory.

1.3 Research aim

To ascertain the material properties of CFF technology and whether it exhibits the behaviour of composite laminates.

1.4 Research objectives

1.4.1 Main objectives

1) To obtain all necessary material properties according to several selected printing layup orientations by subjecting nylon with carbon fibre reinforcement to tensile tests.
2) To statistically analyse data gathered from these tests and compare them with usual laminate composite theory.

1.4.2 Secondary objective

1) Constructing a mathematical model to predict test results by using appropriate methods.

1.5 Research methodology

This study involved the testing and investigation of nylon with carbon fibre reinforcement specimens that are printed with a Markforged Mark Two printer, using Eiger as its slicing software. All necessary internal structure orientations are controlled by using this program, and the material is limited to nylon (only core material that this particular machine can print) and carbon fibre (selected reinforced material of interest).

Tensile tests were done according to ASTM standards to obtain valuable material properties of different printing layup orientations. These property values were used as input values for a recognised composite laminate analysis program whereby a comparison between the experimental and theoretical data were evaluated. Where the results correlate, the CFF technology can most possibly be seen as a laminate composite. However, where the results do not correlate, an alternative approach (in the form of a mathematical model) is required and constructed. This model is based purely on analytical mathematics.

1.6 Contributions and limitations

The main contribution towards the broad field of study is a database according to selected interior layup structure angles and their related mechanical properties. This ensures that future design

considerations for objects to be printed on the Markforged Mark Two will have a suitable material property data foundation. Furthermore, it will enhance the philosophy and magnificence of layup orientations in FFF.

The limitations of this study are narrowed down to the material, the printer, and its slicing software (with a few set parameters). These set parameters include the layer thickness, nozzle diameter, raster width range, and number of contours. Furthermore, all material testing is done on the MTS Landmark® (100kN) machine situated at North-West University Potchefstroom campus.

1.7 Chapter layout

Chapter 2 provides a literature review on the CFF technology, Markforged Mark Two, composite materials, and the similarity between the latter and FFF/CFF. Chapter 3 deals with the theory of composite material properties along with the determination of these properties. In Chapter 4 the experimental procedures of the tensile tests are discussed. Chapter 5 gives a summary of the results with discussions of these experimental outcomes. In Chapter 6 discusses and compares the CFF and classical laminate theory (CLT). Chapter 7 presents a possible mathematical module to predict the ultimate tensile strength results for areas in which laminate theory has failed. Chapter 8 concludes all the previous chapters and summarises the findings of this dissertation together with recommendations and future work. The appendices follow.

Chapter 1 briefly explained the background, problem statement, research methodology and objectives, contributions and limitations of this dissertation.

CHAPTER 2

LITERATURE REVIEW

This chapter discusses six of the main elements of the study's literature review, namely CFF technology, the 3D printer that was used, composite materials, the similarities between FFF and composites, fibre reinforcement in FFF technology, and the similarities between CFF and laminate composites.

2.1 CFF technology

CFF is an additive manufacturing technology that reinforces an object with fibres during a typical FFF process. Usually, the printer consists of two nozzles – one for the core matrix material and the other for the reinforced fibre material. The reinforced fibre is 'ironed' onto the previous layer – this process is illustrated in Figure 2-1 below:

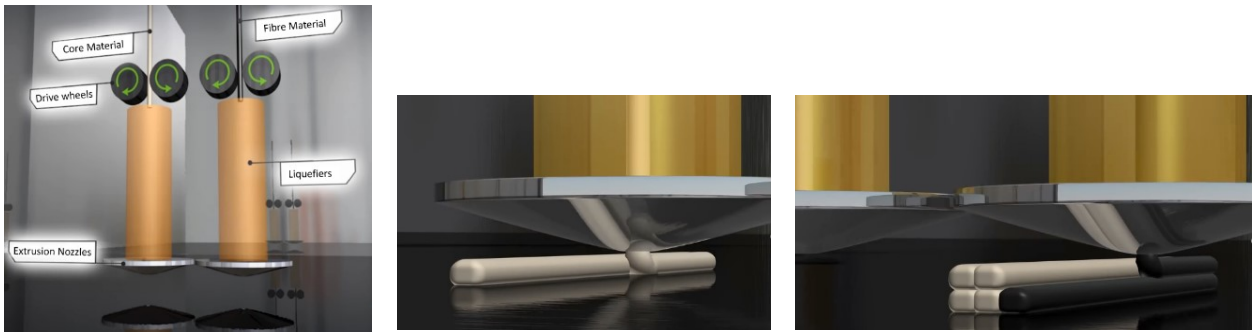

Figure 2-1: Visual representation of the continuous fibre fabrication process [9]

The fibre material comprises long continuous fibre strands that are pre-impregnated with resin (see Figure 2-2) to ensure complete bondage between each of the adjacent layers. Literature shows that fibre-reinforced thermoplastics are indeed much stronger in several directions than regular FFF material and objects without reinforced materials (see section 2.5).

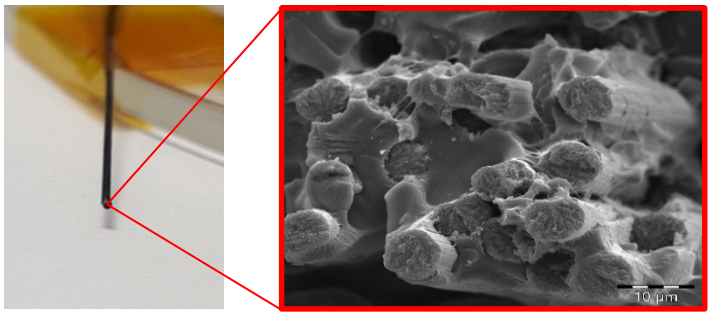

Figure 2-2: Markforged's carbon fibre filament [10]

2.2 Markforged Mark Two 3D Printer

Founded in 2013 and based in Cambridge in the United States, Markforged Inc. is a company that designs, develops and manufactures 3D printers. They ensure in-layer fibre additive manufacturing by using a technology called CFF. As the name indicates, the fibre is continuous and thus not cut into short strands like other fibre-reinforced composites. This greatly improves the mechanical properties of the final printed product.

With a build volume of 320 (l) x 132 (w) x 160 (h) mm and a layer height of 0.125 mm, the Mark Two is ideal for printing large components with endless geometric possibilities limited only to the user's imagination. It has a dual extrusion head – one for the core materials and the other for the fibres (see Figure 2-1). The fibre nozzle includes a cutting mechanism that cuts the fibres every time it lays a consecutive layer of fibre. Furthermore, this machine uses a three-point magnetic location mechanism that enables it to hold the built plate in place perfectly.

The Mark Two uses the Eiger slicing software with superbly optimised preset parameters which include the number of wall layers, infill density, infill style (triangular, hexagonal, or concentric) and the top and bottom layers. With wireless connectivity, cloud-based pre-processing and job management systems, and a user-friendly interaction display, this is any AM designer's software of choice.

Eiger enables the user to parametrically manage every layer independently by making use of the internal view option. The wall thickness can be managed as well as the internal fills on a layer-to-layer basis. The internal fill can be either concentric or isotropic or a combination of both. The *use fibre* option automatically sandwiches the fibre layer arrangements for any kind of build. This fibre deposition is done in a single 2D plane; thus no fibre plies are being laid over a previous layer. Furthermore, Eiger allows the user to pause the printing process at any time, which is ideal when wanting to insert additional parts into the printed build.

The core materials used by this printer are nylon and onyx. Markforged's onyx is a material that combines nylon with micro carbon reinforcement [11]. These two core materials can be reinforced with the following fibres: glass fibre, Kevlar, carbon fibre, and high-temperature glass fibre (HTGF). The glass fibre is the cheapest while the HTGF can be used in applications over 105 °C, with a heat deflection point of 150 °C. The selection of material combinations depends completely on the user's objectives.

A reliable machine such as the Mark Two requires working with the Eiger software to ensure that the final reinforcement of the printed parts is suited for certain applications. Engineering decisions

on the form of any part and the key material control are of utmost importance when it comes to the printing of useable parts [11].

2.3 Composite materials

A composite material is a combination of two or more dissimilar components or phases, and must meet the following three criteria before it can be classified as such:

- The proportions of each element in the overall material must be reasonable (usually more than 5%);
- The properties of the composite as a whole must differ from that of its individual elements;
- Manufacturing of the composite must be done by mixing or combining the elements in different manners [12].

From the above criteria it is clear that CFF might be viewed as a composite material, with point three as a debatable characteristic. It is therefore important to investigate whether CFF technology complies with classical laminate theory (CLT). The diagram in Figure 2-3 below shows the classification of composites, illustrating that CFF might even be a combination of continuous, discontinuous, and laminate types of composites altogether.

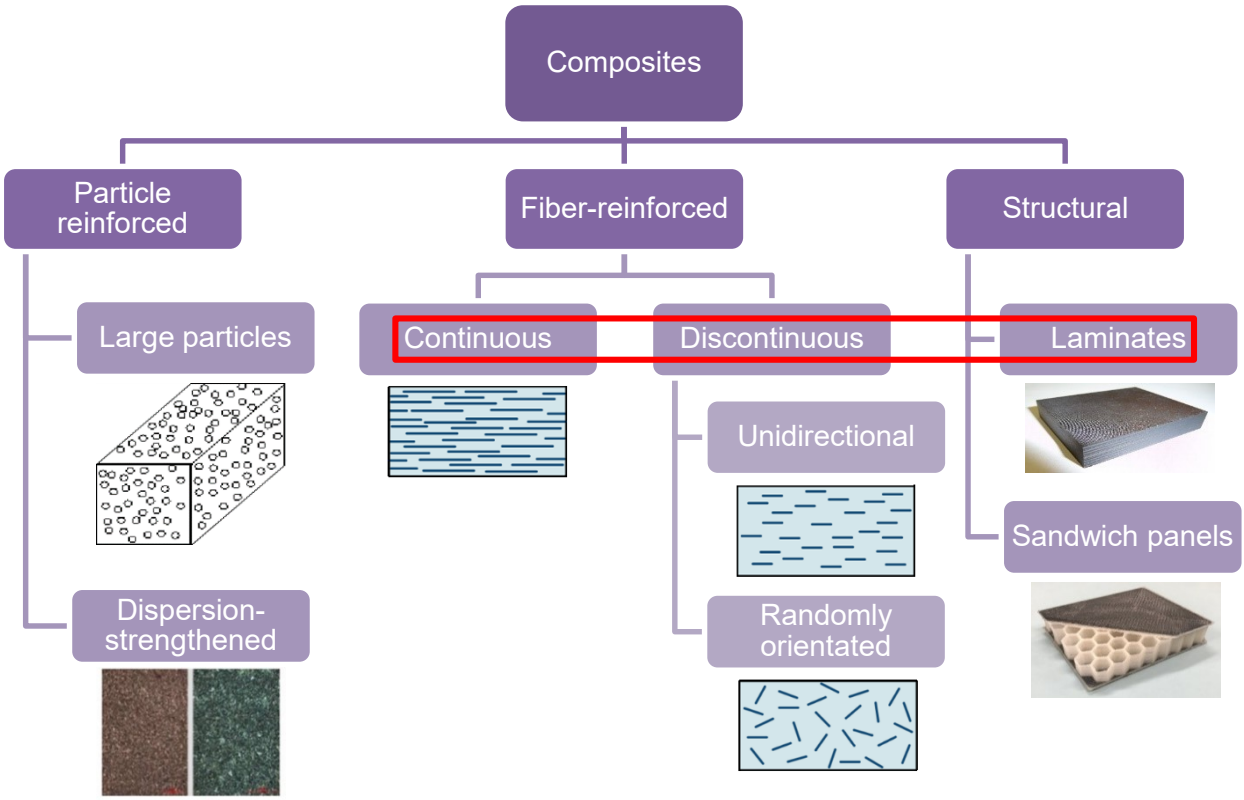

Figure 2-3: Categories of composites

The Figure 2-4 below gives a broad overview of the composition of fibre-reinforced composites. The fibre, in this case, is Markforged's own carbon fibre filament and the resin is a combination of Markforged nylon thermoplastic and the resin already present in the carbon fibre strands (see Figure 2-2). From this one might conclude that CFF technology does indeed comply with the CLT. However, an in-depth study is required, for which the theoretical calculations can be seen in Chapter 3.

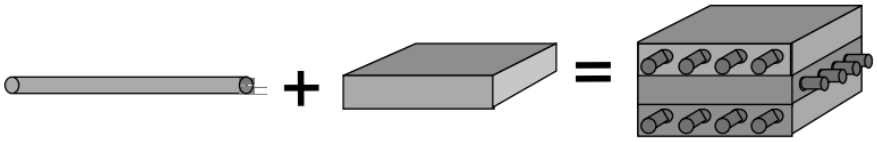

Figure 2-4: Basic composite of fibre-reinforced composites (fibre with resin)

2.4 Similarities between FFF and composites

Previous findings on the similarities between FFF and composites and whether this additive manufacturing technology does or does not comply with the theory of composite structures are discussed in this section, which reveals whether the applicable study does support this idea or not.

According to Tekinalp [13], having FFF rules of conduct is important for rendering this technology suitable for producing functional parts and for future development in the manufacturing of composite products. Before mechanical property prediction of FFF parts can be done it is necessary to understand the behaviour of the material itself and the effects that FFF build parameters have on this composite material [14].

In his study, Kruth [15] presumes that FFF can be considered as a composite material on the basic premise that gradually adding material is similar to that of the manufacturing process of composites. Furthermore, a study by Sun [16] states that FFF prototypes can indeed be viewed as composite structures on the premise that it is composed of partially bonded filaments.

However, there do exist some slight differences between the mechanical properties of FFF and composites, according to Guessasma [17] – he attributes these differences to the weak bonding between the layers and structured porosity. Both these parameters depend on the building direction, which is a similar phenomenon in composite theory.

The interpretation of Bagsik's [18] study suggests that acrylonitrile butadiene styrene (ABS) FFF parts can be seen as a composite material although the layer-to-layer bonding will not reach a complete adhesion condition. It is also evident from a study by Li and Sun [19] that FFF prototypes

are orthotropic composites and that the material can be viewed and analysed as a composite at different levels and scales, all of which depend on the specific behaviour under certain conditions.

Although Li and Sun's study explores treating an ABS FFF printed material as a composite, the authors argue that composite theory requires perfect bonding between the layers, which assumes that the plastic filaments are perfectly bonded, and any voids left between the filaments are analogous to the voids in the matrix material itself [20].

Trends to overcome anisotropy in the development of future composites by means of FFF were investigated in the study by Torrado [21], which found that microvoids are a key characteristic of FFF parts, as the significant bonding factor is that between the filaments and these voids. At the microlevel, each layer property is a function of the filament property and void density, whereas at the macrolevel it can be viewed as laminates of bonded laminar [22].

A similar conclusion was made by Huang [23] in his study of Alternate Slicing and Deposition Strategies for Fused Deposition Modelling, from which it appears that FFF technology and material might be viewed as a laminate composite (see Figure 2-3). This was also the finding in the study by Belter [24], who investigated which filling technique is best suited for bending forces on FFF materials. Another study that shares this conclusion is that by Chaturvedi [25], which states that these fabricated parts do take the form of laminate composites with vertically stacked layers, each consisting of adjacent material fibres or raster groups with forming voids.

According to Sayre III [20], prior research on FFF modelling indicates that the assumption of perfect bonding in composite theory is inaccurate and proposes modifications to the theory. Treating FFF printed parts as composites with a few simple modifications to the material properties appears to agree better with the experimental data than the isotropic model. Modelling an FFF part as a layered composite with modified properties is an appropriate tool with which to simulate real-world conditions. Being deposited in layers, FFF printed materials may lend themselves to composite theory, where the stack of printed layers in FFF is almost analogous to a composite laminar that is contained within a laminate. In his study, Sayre III made use of the CLT to analyse composite materials.

The study of the influence of processing and orientation print effects on the mechanical and thermal behaviour of 3D-Printed ULTEM 9085 Material done by Zaldivar [26] suggests that FFF materials do behave more like laminate composite structures than isotropic cast resins. However, from this study of Zaldivar it should be noted that the behaviour displayed by FFF materials are also observed in composites even when porosity levels are as low as 0.5%.

A study by Zaldivar used the ASTM D638 standard designed for testing polymeric bulk materials, in which FFF parts resemble more of a composite structure. Zaldivar further suggests that the ASTM D3039 (a method specifically designed to test composite materials) needs to be followed rather than D638. It is also evident from a study by Smith et al. [27] that a decrease in variability is achieved by improved gripping when using D638. They noted that the clamp compression for specimens need to be well-controlled to reduce possible damage.

In their study of the material properties of FFF materials, Ahn et al. [28] applied a computer model of FFF ABS parts to predict the failure of parts by using laminate theory. They found that there was a good correlation between the experimental and the theoretical failure loads. This is exactly what is done in this dissertation in using the Laminate Analysis Program (LAP – see Chapter 6 for details).

As an introduction to Section 2.5, which deals with fibre reinforcements within FFF technology, this section concludes with a quotation from a portion of Ahn's [28] study: "The extruded fibre used to manufacture the part has some level of anisotropy, the build process results in a polymeric oriented microstructure similar to the cross-sections of fibre-reinforced composite structures, and the limited degree of fusion between the fibres also results in a patterned void distribution, all of which may contribute in a non-linear manner to the mechanical and thermal expansion response of the material." Thus far, it appears that CFF technology may be seen as a non-linear laminate composite material.

2.5 Fibre-reinforced in FFF technology

Although additive manufacturing by means of FFF does have its benefits, the end product is usually not strong enough for real-life applications. Hence, a reinforcement during one of the multiple AM processes is highly recommended, and its improved strength is evident in previous research studies. The following two subsections discuss previous studies on fibre-reinforced FFF parts, from which it is evident that fibre reinforcements enhance the strength of printed parts. Short fibres are discussed first, followed by a discussion on continuous fibres.

2.5.1 Short/chopped fibres

This section focuses on the studies that were done on short or chopped fibre reinforcements, thus, fibre reinforcements that include techniques used before the printer's nozzle, while Section 2.5.2 focuses on the studies done on continuous fibres (techniques used after the nozzle).

Matsuzaki [29] used direct fabrication without the use of moulds, with the core material being PLA. The fibre-reinforced material that was used is carbon fibre and twisted yarns of natural jute

fibres. To improve the mechanical properties of the end product, the objects were reinforced with unidirectional carbon fibre, which included both the jute-reinforced and unreinforced thermoplastics. The study found that carbon fibre reinforcement improves the tensile strength of the printed composites.

Furthermore, it was found that normal FFF printed parts are not as strong as CFR parts, which can be ascribed to the thermoplastic resins. Two elements found to further improve the mechanical properties of thermoplastic resin parts are the lamination direction and the laminate thickness.

Carbon fibre composites have excellent mechanical performance, and it is clear from Matsuzaki's study that the higher the carbon fibre content, the higher the strength and stiffness will be. However, the traditional fabrication methods for constructing composites requires exclusive facilities and machinery, hence a more affordable technique (such as CFF) will be highly valued. Reinforcement techniques such as carbon black, carbon nanotubes, glass fibres, and reinforced platelets are blended into thermoplastic filaments before being loaded into the printer.

The Markforged Mark Two has a dual extruder (one for the core and one for the reinforced material) and will thus greatly add to the various reinforcement techniques. With this technology the only fibre variable parameter is its direction during the printing process. Hence, the raster/infill angles are the main focus of this dissertation.

During Matsuzaki's study, the Blade1 3D printer was modified to implement CFF technology, though the study only briefly mentions the influence of the printing orientations on the mechanical properties of the printed parts. Nevertheless, tensile testing was done on PLA, the continuous fibre-reinforced thermoplastic composites (CFRTP), and the jute fibre-reinforced thermoplastic composites (FRTP), with the results showing that the CFRTP is much stronger than the rest.

Figure 6 on page 5 of Matsuzaki's study reveals that a combination of CFF and FDM technologies will result in noticeably stronger printed objects, and that is exactly what Markforged managed to accomplish with their Mark Two printer.

According to Ning et al. [30], there is a critical need to advance mechanical properties of FFF-processed thermoplastic parts, and one of the possible methods that can be used is carbon fibre-reinforced plastics within the part. They used carbon fibre-reinforced plastic feedstock filament in their studies and did tensile tests according to the ASTM D3039 and flexural tests according to the ASTM D790-10 standards. The core material that was used is ABS, where they mixed virgin ABS thermoplastic pellets together with carbon fibre powders for the feedstock material.

Further investigation was done on the carbon fibre content (wt%) and the results show that a value of 5–7 wt% has the highest tensile strength with a carbon fibre length of 150 µm. This combination produced the highest flexural stress, modulus, and toughness but not the highest yield strength. A 10 wt% carbon fibre content in the ABS yielded no improvements.

Short fibre (0.2–0.4 mm) reinforced ABS feedstock material was investigated in a study by Tekinalp [13]. The fibre breakage was found to have increased as the fibre loading increased due to the increased fibre-to-fibre interaction. FFF processing with 5 to 7 µm diameter short CFR resin has not yet been reported on.

Tensile tests were done according to the ASTM D638 Type V standards and FFF technology was compared with compression moulding. The percentage of carbon fibre in the ABS was set to 0%, 10%, 20%, and 30%. However, the possibility of fibre breakage exists during the compounding/mixing of fibres with resin resulting from the interactions between fibres and the instrument surfaces, resin, or other fibres. Furthermore, FFF samples are expected to have a lower average fibre length even at equivalent fibre loading.

It was found that the specimens fabricated by using FFF have similar strength values to those manufactured by compression moulding because the FFF samples compensate for the negative effects of porosity fibre bonding. Tekinalp's study states: "The FFF process not only increases the orientation of the polymer molecules but it also improves the fibre dispersion and uniformity at the parts that are manufactured layer by layer". However, it was evident that the porosity of tensile properties has a more dominant effect on the fibre orientation aspect. Thus, the minimisation of the pore formation during printing plays an important role in the mechanical properties of the end parts and needs to be investigated for future reference, hence the importance of the fill density and orientation of CFF technology.

2.5.2 Continuous fibres

Sandwiching carbon fibre between the lower and upper plastic parts of a certain specimen was performed during the studies of Mori et al. [31]. Static and fatigue tests were then performed to evaluate the mechanical properties of these specimens. First, the lower section of the specimen was printed, then carbon fibre was placed on top of the lower section and then, to finish the specimen, they printed on top of the carbon fibre layers, hence the name sandwiching. However, these specimens did undergo heat treatment afterwards for the carbon fibre to fuse properly with the ABS and to improve the strength. The study of Mori et al. proves that technology such as CFF can benefit the whole AM industry.

Studies by Chapiro [32] found that combining composite materials with 3D printing is the additive manufacturing method of the future. Furthermore, fibre length was found to play a critical role in the mechanical properties of the final part, although Markforged is currently the only company that offers a CFF process (the printers use a fibre filament with a volume fraction of 34%) in which the printer cuts the carbon fibre below the critical fibre length, as claimed by Chapiro.

Further investigations showed that some of the Cosine additive printers do not cut the carbon fibre strands too short, and Stratasys has developed a new FDM method similar to that of Arevo Labs, of which the latter has developed a curved FFF printing technique.

The elastic properties of fibre-reinforced 3D printed structures were predicted in the studies by Melenka et al. [33] by using the volume average stiffness method. Three different volume fraction values of fibres (4.04, 8.08, and 10.1%) were tested, and it was found that the highest value resulted in the highest Young's Modulus (9.001 GPa). In general, FFF printed parts have lower elastic properties than injection moulded components of the same thermoplastics.

One essential claim of Melenka et al. is the fact that continuous fibre-reinforced 3D printed parts have not been extensively investigated in previous literature. Recognising the use of CFF for functional parts must be preceded by determining and evaluating the mechanical properties. One of the first steps involves certain tests (such as tensile, compression, and flexural). The second step usually involves the prediction of these, and future, tests. Some prediction models may include classical laminate plate theory (CLPT) and the visual analogue scale (VAS) method.

The core material that was used in the study of Melenka et al. was nylon reinforced with Kevlar fibre. These fibres were printed concentrically, up to a maximum of 5 rings. Only tensile tests (ASTM D638) were performed on these specimens and the micromechanical properties were managed by using a model developed by Rodriguez [34], which treats FFF-printed parts as a plastic/void composite. During this dissertation the void density is set at 100%.

Melenka et al. found that these FFF-printed specimens act as a transversely isotropic material. Furthermore, the fibre waviness was found to affect the mechanical properties of the 3D printed specimens, as the embedded fibres are not entirely aligned with the loading axis of these specimens, thus supporting the goal of this dissertation. The VAS method did have some differences resulting from the waviness of the Kevlar fibres, as the VAS method assumes that these yarns are straight. The differences in predictions and experimental values can also be attributed to the relatively low volume fraction (4%). It is noticeable that composite material models assume that fibres are bonded perfectly.

The VAS method further shows that a higher fibre volume fraction (more than 8%) will result in a higher prediction accuracy. Melenka et al. only examined concentric fibre reinforcement, although the Eiger software is capable of full layer reinforcement, which is dealt with in this dissertation.

A study by Yao et al. [35] reveals that reinforcing parts with carbon fibre can increase the tensile and flexural strength by up to 70% and 18.7% respectively, while a weight reduction of up to 26% can be achieved without decreasing the tensile strength. The strength of pure carbon fibre parts from TORAY Torayca Company are compared with 3D printing parts, and it was found that 3D printing parts can be made stronger by implementing the following four aspects:

1) Using ribs or internal printed supports;
2) Optimising the process parameters (such as print extrusion, temperature, build orientation, raster angle, and contour width);
3) Developing new materials – feedstock filaments made of metal or polymer composite material. Other improved materials can include thermotropic liquid crystalline polymer (TLCP) fibres and especially carbon fibre-reinforced thermoplastic filaments;
4) Developing new methods or technologies such as printing of carbon fibre composites by in-nozzle impregnation.

All four the abovementioned points only focus on reinforcing the printed structures, whereas only a few aim to reduce the amount of material, and none of them considers a self-monitoring function. However, the reinforcement of carbon fibre proofs could be one of the best options thanks to its piezo-resistive behaviour.

The core material during the study of Yao et al. was PLA, while the reinforcement material was polyacrylonitrile(PAN)-based continuous carbon fibre. Tensile and three-point bending tests were done to evaluate the mechanical properties of the specimens and it was found that carbon fibre resolves the intrinsic inadequate strength of FFF printed structures. Although the study was primarily done to test whether CFF technology can be used for manufacturing prosthesis (due to the electrical properties of carbon fibre) it still aids as a good literature platform for this dissertation.

According to a study by Tian et al. [36], a carbon fibre content of 27% and a hatch spacing of 0.4 mm resulted in the strongest parts – short fibres improved the tensile strength by up to 20%.

PLA was reinforced during the studies of Li et al. [37] and the tensile and flexural strength increased by 13.8% and 164.0% respectively. The tensile strength of short CFR resulted in 68 MPa while continuous carbon fibre reinforced resulted in 91 MPa. CFR composites can become the next-generation composite fabrication methodology and that is exactly what Markforged achieved with their products.

2.6 Similarities between CFF and laminate composites

From section 2.5 it is evident that fibre-reinforced thermoplastics are indeed much stronger than the usual FFF parts. Numerous previous studies showed that FFF technology can and cannot be seen as a composite material (see section 2.4). Furthermore, from sections 2.1, 2.2, 2.3, and the last paragraph of section 2.4, it is clear that CFF technology may have similarities when compared with CLT. It is, however, important to review the findings from previous investigations to determine whether this statement is true or not.

According to Chapiro [38], a variety of static strength properties of composites depend on the anisotropy of the material. By considering the laminated structure by which composite parts are made, large performance gaps in the strength analysis of CFRTP parts can be reconciled. It is found that carbon fibre composites can have anywhere from four to eight times the ultimate tensile strength of 6061 aluminium. Chapiro further suggested in his study that the fibres in CFRTP need to be multi-directional since many structures are stiffness-driven rather than strength-driven. For this reason, a combination of different fibre orientations are investigated in this dissertation.

To further ratify the goal of this dissertation it is necessary to make mention of the last sentence under the heading “An invalid comparison” on page 373 of Chapiro’s article, which states that an effective carbon fibre 3D printer would be advantageous when optimising the internal fibre paths for higher strength and stiffness properties. Fortunately, Markforged produced the Mark One and Mark Two printers, which are capable of reinforcing nylon or onyx with fibres (see Section 2.2) which, according to Al Dean [11], Tian et al. [39], Elasswad et al. [40], and Bland [41], can be regarded as laminate composite materials. Figure 2 on page 373 of Chapiro’s article shows that continuous carbon is much stronger than discontinuous carbon.

The microstructure and especially the interfaces of fibre-reinforced composites play a magnificent role when it comes to the macroscopic mechanical properties, according to Tian et al. [42]. Unfortunately, no comprehensive experimental investigations have reported on regarding the tensile properties in FFF of CFRP composite parts by the American Society for Testing and Materials (ASTM) for standardised methods as of yet [43]. It is therefore important to fill this gap by investigating the mechanical properties (in respect of tensile testing) of all possible lay-up orientations of CFF.

That being said, Zhang [44] noted that former methods of computing and predicting these properties according to the different orientations cannot directly be adopted, but need to be adapted. Therefore, there is a need to analyse the CFF process to develop a customised orientation optimisation method with related factors or criteria.

Another study by Melenka et al. [45] found that conventional composite material modelling techniques (such as the CLPT) can be applied to CFF materials to predict their mechanical properties. Composite material models assume that the fibres and matrices are perfectly bonded, which might not be the case in the CFF manufacturing process [46]. However, Melenka's study only investigated concentric fibre reinforcement, whereas this dissertation investigates full isotropic layers of fibre reinforcement.

This chapter discussed previous studies on mainly the comparison between FFF/CFF and composite material theory. It is not certain whether CFF technology does comply with the classical laminate theory, and this aspect requires investigating. The following chapter discusses the CLT as well as the use of tensile testing to determine the mechanical properties of specimens.

CHAPTER 3

THEORY OF COMPOSITE MATERIAL PROPERTIES

This chapter discusses the concept behind the classical laminate theory and the determination of the mechanical properties. The reason for selecting the classical laminate theory is that literature shows that the closest similarity between CFF technology and a composite analysis is that of the CLT.

3.1 Material properties

This dissertation aims to understand the behaviour of CFF material, and the best way to do this is to find its relative material properties. A lot of testing can be done on a material to obtain certain parameters and/or characteristics. As discussed in Chapter 1, only tensile testing is executed on the CFF test specimens (see Section 4.1 for details on the dimensions of the specimen).

It is, however, important to note that a variety of tensile test standards exists, and it is crucial to find the appropriate one. As it is not certain whether the CFF material does behave as a laminate composite or not, the standard that was selected for use was the standard test method for tensile properties of polymer matrix composite materials (ASTM D3039). Hence, the validation of this dissertation lies in bridging the gap that lies in the lack of known CFF material properties, while establishing whether the CFF technology's material can, in fact, be seen as a laminate composite material by using LAP.

Furthermore, a laminate composite material can also be seen and treated as a linear or non-linear material, thus emphasising the importance of the investigating the CFF material properties. The following sections discuss all the material properties that can be obtained from a tensile test, which also serve as the input values for LAP.

3.1.1 Stress

The stress (symbol: σ, unit: Pascal [Pa]) within a material can be calculated as the force (symbol: F, unit: Newton [N]) applied on a certain area (symbol: A, unit: cubic meters [m^2]). The force applied is a tensile (pulling) force in the case of a tensile test, and the final equation is plainly:

$$\sigma = \frac{F}{A} \qquad \text{Equation 3-1}$$

The force can be obtained from the tensile test machine (MTS Landmark® - 100kN) while the area is the sectional area of the specimen at the location where it breaks. For composites, this area is the same throughout the length of the specimen.

3.1.2 Strain

The strain (symbol: ε, unit: unitless [-] or percentage [%]) is the percentage of elongation of the specimen from its original length (symbol: L_i, unit: meter [m]) to the final length at which it brakes (symbol: L_f, unit: m). The equation is as follows:

$$\varepsilon = \frac{\Delta L}{L_i} = \frac{L_f - L_i}{L_i} \qquad \text{Equation 3-2}$$

Again, the MTS Landmark® measures the ΔL by means of an extension meter.

3.1.3 Stress-vs-strain graph

When the stress and strain of a tensile test experiment are obtained, these two variables can be plotted, with strain being the independent variable and the stress the dependent variable. The following graph is a typical tensile test graph, and from this graph numerous other material properties can be obtained, which are discussed in the following sections.

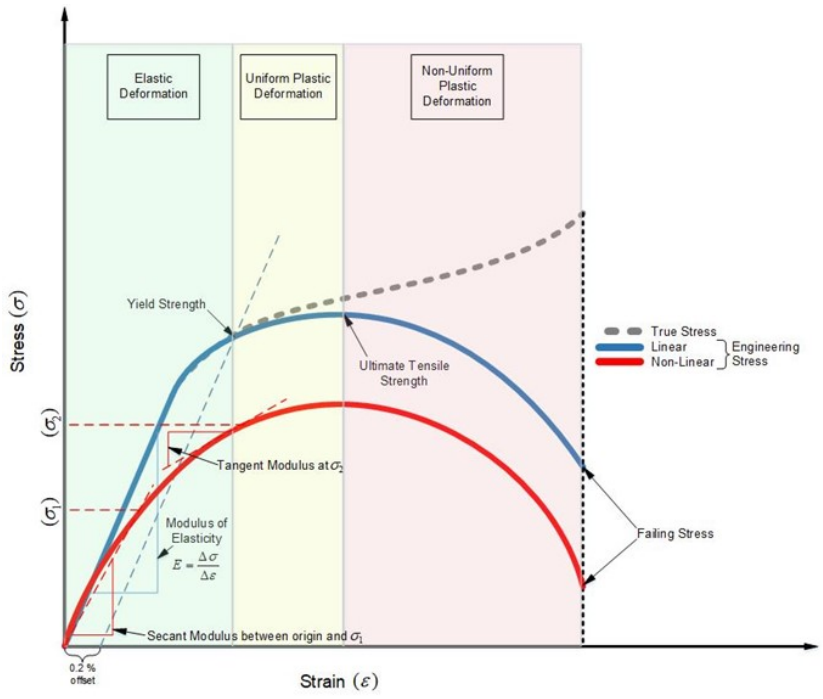

Figure 3-1: Stress vs Strain Graph

3.1.3.1 True stress vs engineering stress

Figure 3-1 shows the visual difference between true stress and engineering stress. True stress is when necking (decreasing of the sectional area) is considered. Thus, as the area decreases the total stress (with a constant force) will also increase (see Equation 3-1). Hence, the graph continues upward until breaking point. However, in the engineering environment, this decrease in the area is not taken into consideration and it is assumed constant throughout the whole tensile test experiment, with a decrease in stress as a result.

3.1.3.2 Linear vs non-linear

It is also evident from Figure 3-1 that the engineering stress can be divided into a linear and non-linear graph. When a material behaves linearly (blue line) it undergoes a constant stress-vs-strain rate (also known as modulus of elasticity) for a certain amount of strain, whereafter it deforms plastically. When a material behaves non-linearly (red line) it never (from the start) experiences a constant stress-vs-strain rate.

It is not certain whether a CFF material is linear or non-linear, and might even be a combination of the two, with the material behaving as a linear material up until a certain point after which it starts behaving as a non-linear material. As a result, the graph will be in-between the blue and red graphs.

3.1.3.3 Modulus of elasticity

The modulus of elasticity (also known as Young's modulus; symbol: E, unit: Pascal [Pa]) is the rate at which the stress changes according to its corresponding strain values. It is simply the gradient of the straight line (in the case of a linear material), or the gradient of the secant or tangent method (in the case of a non-linear material) within the elastic deformation region, and can be calculated as follows:

$$E = \frac{\Delta\sigma}{\Delta\varepsilon} \qquad \text{Equation 3-3}$$

This parameter of a material is one of the three main material properties (with the yield strength and ultimate tensile strength being the remaining two).

3.1.3.4 Elastic deformation region

A material experiences elastic deformation when it is able to return to its original shape after a force is applied and then removed. This region starts at the beginning of the graph and stretches up until the yield strength point and can be easily detected with a linear material. It is, however, more difficult to determine a non-linear material's elastic deformation region. As one of the main goals of this dissertation is to investigate whether CFF material is linear or non-linear, it is assumed that the material tends more to be linear than non-linear for all simplicity purposes.

3.1.3.5 Yield strength

The yield strength (abbreviation: YS, unit: Pascal [Pa]) is the maximum stress a material can handle before moving out of the elastic region. Thus, a stress smaller than the yield strength value will ensure that the material can return to its original shape, while a larger value will cause the material to deform plastically.

Technically speaking, the YS location will be at the exact moment where the graph's gradient starts to decrease – that means it will no longer have a constant stress-vs-strain rate. However, this location is difficult to determine and therefore an offset line is introduced. This straight line is parallel with the modulus of elasticity and is offset by a total of 0.2% (for composites, 2% for steel) to the right of the strain (see Figure 3-1). The point where this line and the graph intersect will be the YS location.

3.1.3.6 Uniform plastic deformation region

The uniform plastic deformation region is the area where the specimen has already passed its YS but not yet its ultimate tensile strength. It is called uniform because it can be seen as an orderly deformation. When a material reaches this area and the force is removed, it will be impossible for the material (or object) to return to its original shape, hence the term plastic deformation. For ductile materials, this area will always be followed by a non-uniform plastic deformation area, while for a brittle material the final failing stress will be within this area (see Figure A-1).

3.1.3.7 Ultimate tensile strength

The ultimate tensile strength (abbreviation: UTS, unit: Pascal [Pa]) is the maximum stress a given material can handle before it completely breaks (brittle material) or enters into its non-uniform plastic deformation region (ductile material). Unlike the modulus of elasticity and the yield strength, which require specific calculations to determine their values, the UTS does not require any further calculations. Therefore, to limit and reduce the enormous influence that inaccurate

successive data standard deviations can have on the final outcome, only the UTS is taken into consideration during the verification process.

3.1.3.8 Non-uniform plastic deformation region

The non-uniform plastic deformation region is the phase in which the specimen (or material) finds itself after having reached its UTS but has not yet broken completely. It is non-uniform because the failing point can occur suddenly at any strain without warning. Strictly speaking, the specimen has already broken internally but not yet externally (into two pieces). It is not desirable to design any object to operate within this area and therefore needs to be avoided by designing according to a higher safety factor to ensure that the material never reaches this area.

3.1.3.9 Failing stress

The final parameter which is directly obtainable from the stress-vs-strain graph is the failing stress. This is purely the point where the specimen breaks completely into two pieces. This parameter does not serve as one of the crucial design considerations as discussed in subsection 3.1.3.8.

Subsection 3.1.3 covered all the necessary material properties that can be obtained from only a stress-vs-strain graph. However, other material properties required by LAP, such as the Poisson ratio, shear stress, shear strain, and shear modulus are discussed in Section 3.2.

3.2 Classical laminate theory

The properties of fibre-reinforced composites are highly directional and for this reason they can be classified as anisotropic materials and more specifically, orthotropic. As discussed in Section 2.3, CFF technology might be considered as laminate-structured composites, which is also the main focus of this dissertation, namely to determine whether this statement is true or not. One of the most important mechanical properties of any material is its stress-strain relationship and in this section, this aspect is examined in respect of a single-layer as well as multiple layers.

3.2.1 Characteristics of orthotropic materials

Figure 3-2 depicts a typical internal view of a specimen with carbon fibre in the Eiger slicing online software (the white represents the nylon while the blue represents the carbon fibre). To best analyse the properties of such an orthotropic material, it is important to define a coordinate system that includes the global (x, y, and z) as well as the fibre directions (1, 2, and 3).

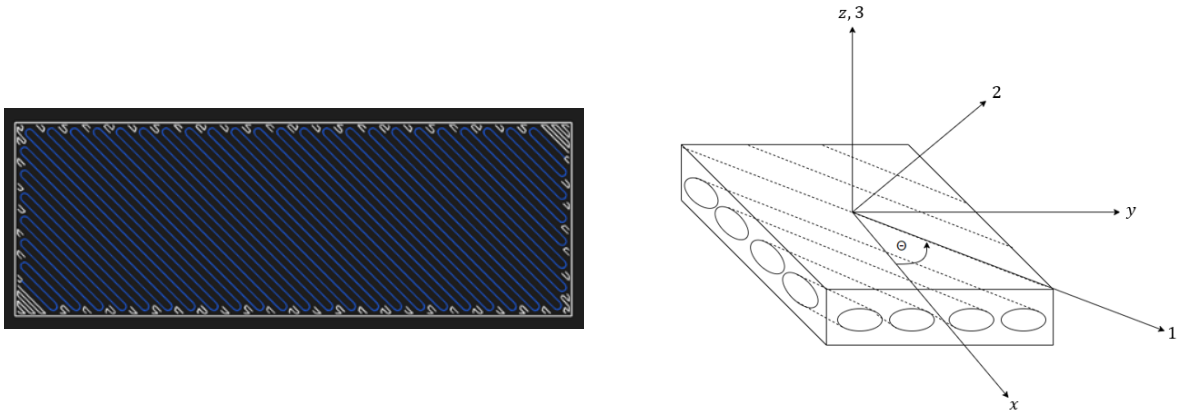

Figure 3-2: (a) Internal view of specimen, (b) Global and fibre direction coordinate system

The material properties will be different in the number 1 and 2 directions, and the stress, strain and stiffness in each direction are given by σ_1, ε_1 and E_{11}, and σ_2, ε_2 and E_{22} respectively. From this, Hook's Law for both directions and the shear strain can be determined for in-plane conditions and is given as follows:

$$\varepsilon_1 = \frac{\sigma_1}{E_{11}} \quad ; \quad \varepsilon_2 = \frac{\sigma_2}{E_{22}} \quad \text{and} \quad \gamma_{12} = \frac{\tau_{12}}{G_{12}} \qquad \text{Equations 3-4}$$

A stress in direction 1 will result in a strain in direction 2 and vice versa. This phenomenon fits right in with Poison ratio theory, and this ratio for the in-plane directions are given as follows:

$$\varepsilon_1 = -\nu_{21}\varepsilon_2 \quad \text{and} \quad \varepsilon_2 = -\nu_{12}\varepsilon_1 \qquad \text{Equation 3-5}$$

while the strain from layer to layer can be calculated as

$$\varepsilon_3 = \frac{\sigma_3}{E_{33}} \qquad \text{Equation 3-6}$$

When certain loadings are acting in on all three directions, the strain in direction 1, 2, and 3 can be calculated as:

$$\varepsilon_{xx} = \varepsilon_1 = \frac{\sigma_1}{E_{11}} - \nu_{21}\frac{\sigma_2}{E_{22}} - \nu_{31}\frac{\sigma_3}{E_{33}} \qquad \text{Equation 3-7}$$

$$\varepsilon_{yy} = \varepsilon_2 = -\nu_{12}\frac{\sigma_1}{E_{11}} + \frac{\sigma_2}{E_{22}} - \nu_{32}\frac{\sigma_3}{E_{33}} \qquad \text{Equation 3-8}$$

$$\varepsilon_{zz} = \varepsilon_1 = -\nu_{13}\frac{\sigma_1}{E_{11}} - \nu_{23}\frac{\sigma_2}{E_{22}} + \frac{\sigma_3}{E_{33}} \quad \text{Equation 3-9}$$

while the shear strain can be calculated as

$$\varepsilon_{yz} = \gamma_{23} = \frac{1}{G_{23}}\tau_{23} \quad \text{Equation 3-10}$$

$$\varepsilon_{zx} = \gamma_{31} = \frac{1}{G_{31}}\tau_{31} \quad \text{Equation 3-11}$$

$$\varepsilon_{xy} = \gamma_{12} = \frac{1}{G_{12}}\tau_{12} \quad \text{Equation 3-12}$$

with τ being the shear stress and G being the shear modulus. These six equations can be combined in a matrix with the final notation as follows:

$$\begin{Bmatrix} \varepsilon_{xx} \\ \varepsilon_{yy} \\ \varepsilon_{zz} \\ \varepsilon_{yz} \\ \varepsilon_{zx} \\ \varepsilon_{xy} \end{Bmatrix} = \begin{Bmatrix} \varepsilon_1 \\ \varepsilon_2 \\ \varepsilon_3 \\ \gamma_{23} \\ \gamma_{31} \\ \gamma_{12} \end{Bmatrix} = \begin{bmatrix} \frac{1}{E_{11}} & \frac{-\nu_{21}}{E_{22}} & \frac{-\nu_{31}}{E_{33}} & 0 & 0 & 0 \\ \frac{-\nu_{12}}{E_{11}} & \frac{1}{E_{22}} & \frac{-\nu_{32}}{E_{33}} & 0 & 0 & 0 \\ \frac{-\nu_{13}}{E_{11}} & \frac{-\nu_{23}}{E_{22}} & \frac{1}{E_{33}} & 0 & 0 & 0 \\ 0 & 0 & 0 & \frac{1}{G_{23}} & 0 & 0 \\ 0 & 0 & 0 & 0 & \frac{1}{G_{31}} & 0 \\ 0 & 0 & 0 & 0 & 0 & \frac{1}{G_{12}} \end{bmatrix} \begin{Bmatrix} \sigma_1 \\ \sigma_2 \\ \sigma_3 \\ \tau_{23} \\ \tau_{31} \\ \tau_{12} \end{Bmatrix} \quad \text{Equation 3-13}$$

Although the above matrix does consider all three directions of a laminated object, it is important to note that most of the engineering applications of laminates have negligible thicknesses when compared with their lengths and widths, and therefore, only an in-plane scenario is considered, thus resulting in a zero stress and shear stress in all z-directions ($\sigma_3 = \tau_{23} = \tau_{31} = 0$). The matrix in Equation 3-13 can be reduced to:

$$\begin{Bmatrix}\varepsilon_{xx}\\ \varepsilon_{yy}\\ \varepsilon_{xy}\end{Bmatrix} = \begin{Bmatrix}\varepsilon_1\\ \varepsilon_2\\ \gamma_{12}\end{Bmatrix} = \begin{bmatrix}\frac{1}{E_{11}} & \frac{-\nu_{21}}{E_{22}} & 0\\ \frac{-\nu_{12}}{E_{11}} & \frac{1}{E_{22}} & 0\\ 0 & 0 & \frac{1}{G_{12}}\end{bmatrix}\begin{Bmatrix}\sigma_1\\ \sigma_2\\ \tau_{12}\end{Bmatrix} \qquad \text{Equation 3-14}$$

Equation 3-14 above shows how the strain can be determined. However, this is not practical and ideal in an experimental environment, because usually a specimen's strain is determined and from this the stresses calculated. To obtain these stresses (σ_1, σ_2, and τ_{12}), the inverse of the matrix can be calculated according to the measured strains (see Chapter 4 for experimental procedures):

$$\begin{Bmatrix}\sigma_1\\ \sigma_2\\ \tau_{12}\end{Bmatrix} = \begin{bmatrix}\frac{1}{E_{11}} & \frac{-\nu_{21}}{E_{22}} & 0\\ \frac{-\nu_{12}}{E_{11}} & \frac{1}{E_{22}} & 0\\ 0 & 0 & \frac{1}{G_{12}}\end{bmatrix}^{-1}\begin{Bmatrix}\varepsilon_1\\ \varepsilon_2\\ \gamma_{12}\end{Bmatrix} \qquad \text{Equation 3-15}$$

$$\therefore \begin{Bmatrix}\sigma_1\\ \sigma_2\\ \tau_{12}\end{Bmatrix} = \begin{bmatrix}\frac{E_{11}}{1-\nu_{12}\nu_{21}} & \frac{E_{11}}{1-\nu_{12}\nu_{21}} & 0\\ \frac{E_{22}}{1-\nu_{12}\nu_{21}} & \frac{E_{22}}{1-\nu_{12}\nu_{21}} & 0\\ 0 & 0 & G_{12}\end{bmatrix}\begin{Bmatrix}\varepsilon_1\\ \varepsilon_2\\ \gamma_{12}\end{Bmatrix} \qquad \text{Equation 3-16}$$

Now that the stresses in the two global directions (x and y – see Figure 3-3) and the shear stress (xy) can be determined, it is crucial to find the properties of the fibre orientations (1, 2, and 12). One way this can be done is by transforming the global coordinates to the fibre orientation coordinates by means of Mohr's circle. The corresponding stresses with the fibre orientation coordinates can then be calculated with Equation 3-17 to 3-19.

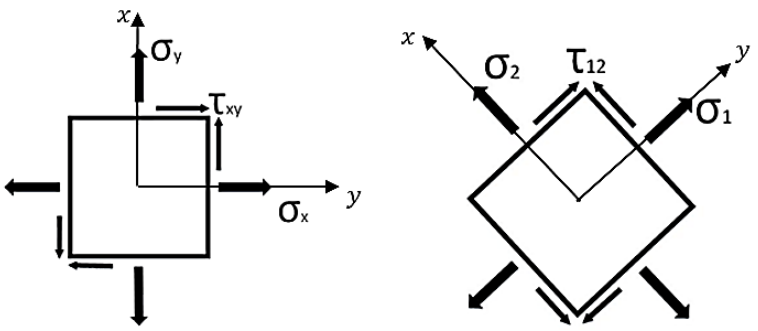

Figure 3-3: Stress and failure analysis (a) Global, (b) Fibre direction coordinate system

$$\sigma_1 = \frac{\sigma_x+\sigma_y}{2} + \frac{\sigma_x-\sigma_y}{2} cos2\theta + \tau_{xy} sin2\theta \qquad \text{Equation 3-17}$$

$$\sigma_2 = \frac{\sigma_x+\sigma_y}{2} - \frac{\sigma_x-\sigma_y}{2} cos2\theta - \tau_{xy} sin2\theta \qquad \text{Equation 3-18}$$

$$\tau_{12} = -\frac{\sigma_x-\sigma_y}{2} sin2\theta + \tau_{xy} cos2\theta \qquad \text{Equation 3-19}$$

Applying some trigonometric identities while combining the above three equations in one matrix equation renders the following matrix:

$$\begin{Bmatrix} \sigma_1 \\ \sigma_2 \\ \tau_{12} \end{Bmatrix} = \begin{bmatrix} cos^2\theta & sin^2\theta & 2sin\theta cos\theta \\ sin^2\theta & cos^2\theta & -2sin\theta cos\theta \\ -sin\theta cos\theta & sin\theta cos\theta & cos^2\theta - sin^2\theta \end{bmatrix} \begin{Bmatrix} \sigma_x \\ \sigma_y \\ \tau_{xy} \end{Bmatrix} \qquad \text{Equation 3-20}$$

Fortunately, there is a program that specifically deals with laminate theory called LAP. This program has all the previous equations built in and is henceforth used to conclude whether CFF material does indeed behave as a laminate material or not.

Chapter 3 discussed the basic theory behind the most important material property parameters and provided a brief overview of the classical laminate theory. The used for the verification purpose (LAP) was also introduced during this chapter.

CHAPTER 4

EXPERIMENTAL PROCEDURE

The ASTM D3039 standard were used to gather enough data toward contributing to the conclusion of the dissertation's main aim. This chapter discusses the specimen dimensions, variables, test bench specifications, as well as the experimental procedure.

4.1 Specimen dimensions

After investigating the ASTM D3039 standard [47] together with Tables 1 and 2 on the standard documentation pages 5 and 6 respectively, the following specimen dimensions were decided on (all dimensions in mm):

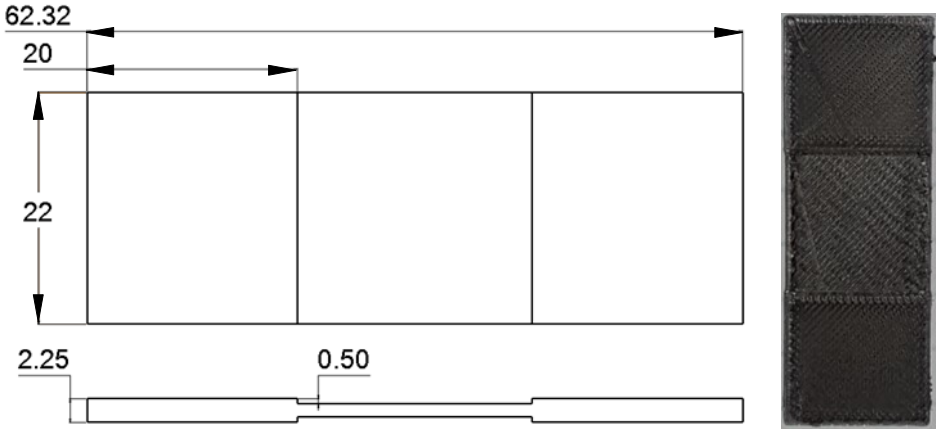

Figure 4-1: Specimen dimensions and final visual appearance

As the Markforged Mark Two printer prints nylon reinforced with carbon fibre, the following brief explanation towards the internal structure (see Section 4.2.1 on a detailed explanation of laminated orientations and layouts) of the specimen is notable:

- The outline of the specimen is covered with 0.4 mm thickness nylon strands;
- The 0.5 mm tabs consist of four layers of solid nylon (the 90° corners on the inside do not have a significant influence on the stress thanks to the FFF manufacturing process);
- The 1.25 mm thickness middle section of the specimen consists of:
  - a first layer of solid nylon (0.125 mm);
  - followed by eight layers comprising differently orientated, laminated carbon fibre (1 mm); and
  - a final layer of solid nylon (0.125 mm).

The gripping dimension is the distance between the tabs (that is equal to 22.32 mm), thus providing enough space for an extension meter (if needed). During the experimental investigation into the required gripping force, it was found that 5 MPa was sufficient as the grips penetrated the nylon without damaging the carbon fibre strands within the specimen. These carbon fibre layers were orientated at various angles and angular combinations. This internal structure is the focal point of the dissertation and is discussed under Section 4.2 below.

4.2 Variables to be changed

Only the internal layout of the carbon fibre was changed for all practical and consistency purposes. The printer and test bench settings were kept on default while the influence of the uncontrollable variables such as the weather conditions, printing and test room humidity, and the nozzle's temperature fluctuations were kept to a minimum. This was done by printing and testing the specimens in a certain timeframe of the day (between 8:00 and 13:00) during a certain season of the year (winter, June-July 2017 in Potchefstroom, South Africa).

4.2.1 Internal layout of carbon fibre

The different internal layouts of the carbon fibre are discussed in this section. The fibres were printed with a 100% density (each strand adjacent to the other) and only in an isotropic (rectangular) pattern, not concentric. An example of the different compositions of the layers together with the laminated code are illustrated in Table 4-1 below. All angles are orientated with respect to the length of the specimen in intervals of 5° until a certain orientation within the specific composition repeats itself.

Table 4-1: Internal layout combination code of carbon fibre

Category	Laminated code and description	Visual presentation
Unidirectional	$[0]_R$ 1st layer = 0° (R stands for repeat)	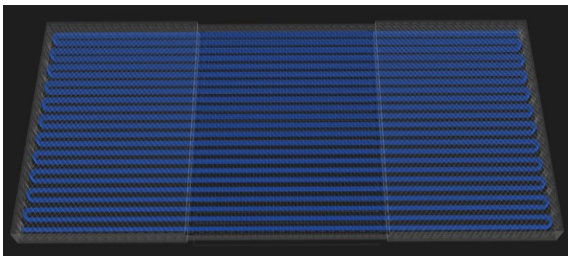
90° Combination	$[5/-85]_R$ 1st layer = 5° 2nd layer = -85° (repeat)	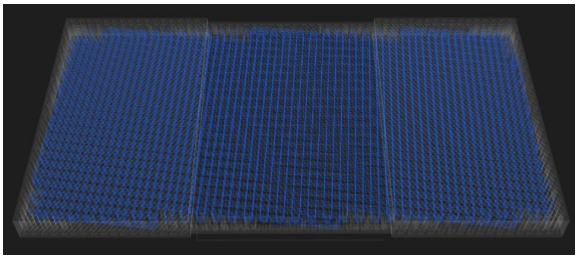

Category	Laminated code and description	Visual presentation
45° Combination	$[10/55/-80/-35]_R$ 1st layer = 10° 2nd layer = 55° 3rd layer = -80° 4th layer = -35° (repeat)	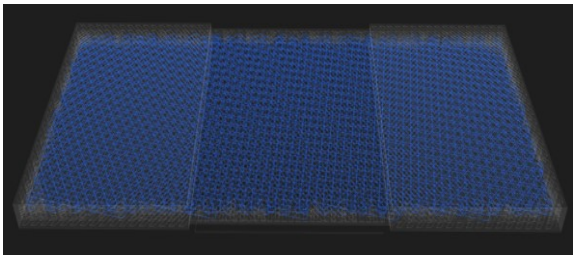
30° Combination	$[15/45/75/-75/-45/-15]_R$ 1st layer = 15° 2nd layer = 45° 3rd layer = 75° 4th layer = -75° 5th layer = -45° 6th layer = -15° (repeat)	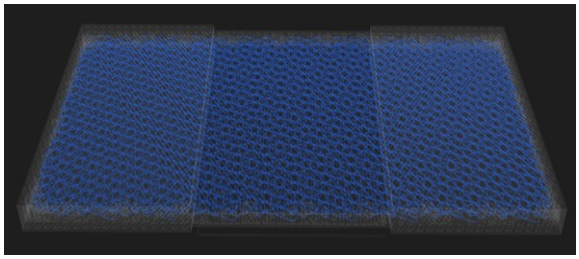

Note from Table 4-1 above that the first row can be seen as a combination of superpositioned strands with no respective difference in the angles from previous strand layers. From here on this combination category is labelled as 'unidirectional', while row two can be seen being 90° apart from the previous strand layer (known as 90° combination), row three being 45° (known as 45° combination) apart, and the final row being 30° apart (known as 30° combination).

The number of different orientations within the first row is nineteen (from $[0]_R$ up to $[90]_R$ with 5° interval), while row two would have an amount of ten ($[0/-90]_R$ up to $[45/-45]_R$ with 5° interval), row three an amount of six and row four an amount of only four different sets of orientation combinations before repetition occurs. With these arrangements, the results of the most applicable combinations of laminated orientations were obtained to construct a database that would provide information that could be used to predict the material behaviour of all other possible orientation combinations. Altogether 39 different orientation combinations were tested with the MTS Landmark® (see Chapter 5 for a summary of all these results etc.).

4.3 Test Bench – MTS Landmark®

The MTS Landmark® test machine has a maximum tensile force of 100kN and was used for all tensile testing during this investigation. The machine's operating speed was set to be 2 mm/min according to the standards while the gripping force was 5 MPa. Data was gathered for the load applied together with its corresponding extension values (in mm – the percentage elongation can then be calculated). From here all necessary calculations could be made to obtain the material properties (see Section 3.1)

4.4 Experimental procedure

The tensile test experimental procedure is quite straightforward but needs to be executed correctly to obtain the most accurate results. The steps are given in table format below. All detail specimen preparation and insertion processes were done according to the ASTM D3039 standards.

Table 4-2: Experimental procedure steps

Steps:	Description
1	Ensure that the operating computer together with the necessary software is ready.
2	Ensure that the clamps are in the desired position.
3	Secure the specimen in the correct position (use tabs to indicate gripping locations).
4	Close the clamps with a force equal to 5 MPa.
5	Begin with the test by activating the software on the computer.
6	When the specimen breaks, stop the data capturing software.
7	Save the raw data (tensile force and extension in mm) for further processing.
8	Open clamps.
9	Remove specimen and insert next. Repeat steps 2 to 8.

[1]

Chapter 4 discussed the specimen dimensions and the variables that change (such as the internal orientated layout of the specimens), in addition to giving some information about the test machine used as well as a brief overview of the experimental procedure. Chapter 5 discusses the results of all the experiments executed.

CHAPTER 5

RESULTS AND DISCUSSIONS

Chapters 1 to 4 dealt with the introduction, the literature review, the theory behind obtaining the material properties, and the execution process of the experiments. This chapter discusses all these experimental results in depth, as they are the focal area of the whole dissertation. All calculations were done by using Microsoft Excel and MATLAB®. Only a summary of the experimental data is shown in this chapter. For detailed results please see Appendix A. Chapter 6 investigates whether CFF materials can be considered as laminate composites or not by comparing the results obtained in this chapter with LAP.

5.1 Summary of all material properties

This section provides the results of all four (unidirectional 90°, 45°, and 30° combinations) layout combination categories in respect of the elastic modulus, yield strength, and ultimate tensile strength. The boxplots function in MATLAB® was used to represent the data in an accurate statistical fashion.

5.1.1 Modulus of elasticity

The modulus of elasticity is the first parameter given in all result tables under Appendix A and therefore it is also the first to be summarised. All summarized boxplots for parameters are shown according to the layout categories – starting with the unidirectional layout.

5.1.1.1 Unidirectional

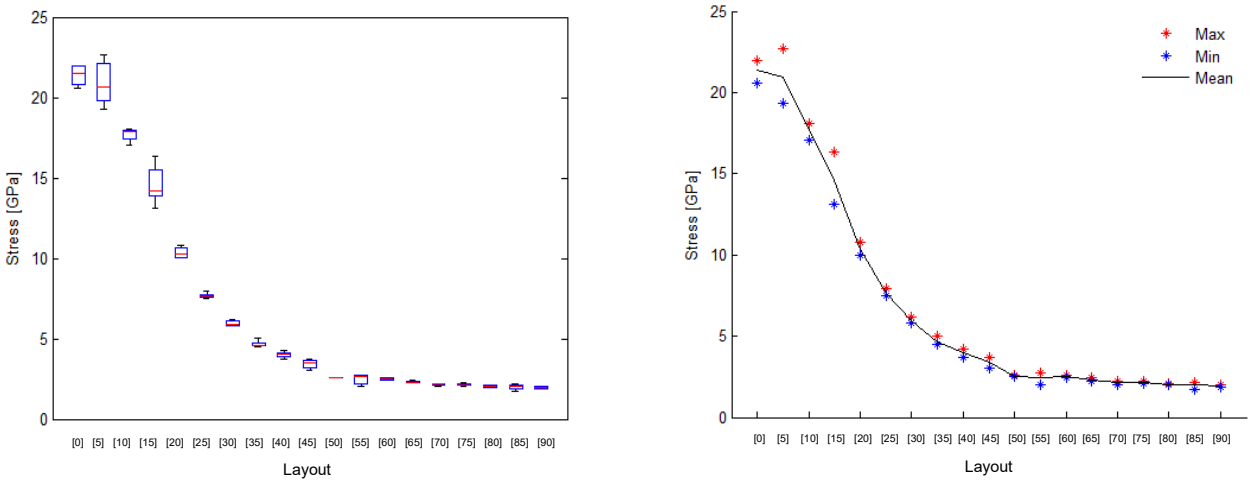

Figure 5-1: Elastic modulus of unidirectional layout (boxplot and line graph)

All 19 subcategories' moduli of elasticity can be seen in Figure 5-1 above in the form of a boxplot. It is clear that there are no outliers at any degree, indicating that the experimental data is trustworthy and a possible trend line can be constructed. Note the movement of the graph from $[0]_R$ up to $[90]_R$. This tendency can be seen more clearly when a line graph of the maximum, mean, and minimum values of the boxplots are constructed (right-hand side of Figure 5-1).

Note that the modulus of elasticity is relatively high at the lower angles, emphasising that the strength of the specimen depends on the direction of the strands. It is further interesting to observe that after about $[50]_R$ the graph converges towards the final strength of the $[90]_R$ layout combination. Note also the spike at the $[5]_R$ (see Section A.1.2 for an explanation of this occurrence). The narrowness at $[50]_R$ is a result of only three tests being conducted (see Figure A-13). Overall, this figure is similar to usual fibre composite material property graphs. The unidirectional layout indicates a potential laminate composite.

5.1.1.2 90° Combination

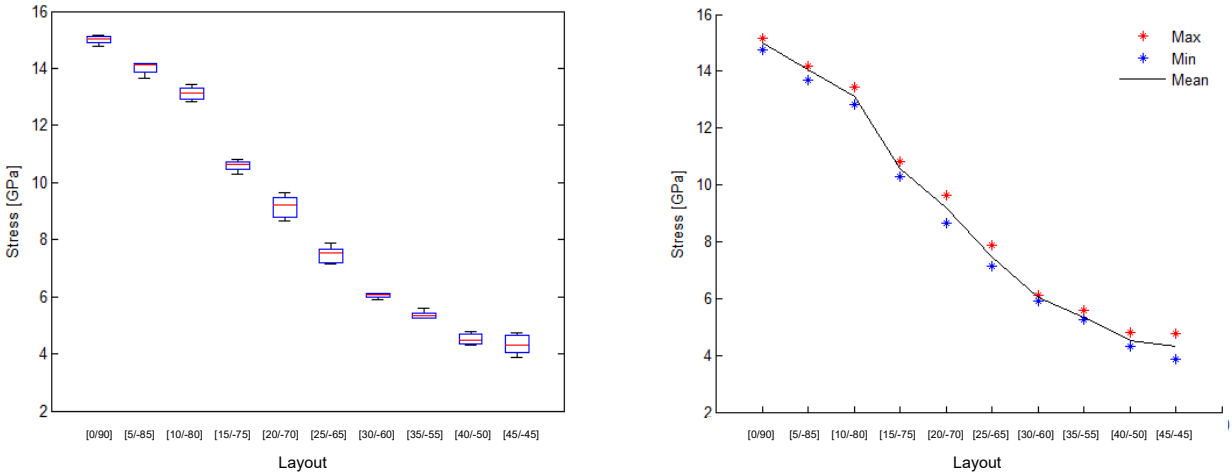

Figure 5-2: Elastic modulus of 90° combination (boxplot and line graph)

The magnitude of the range between the highest value (at the $[0/90]_R$ layout) and the lowest value (at the $[45/-45]_R$ layout) decreases when compared with the graph of the unidirectional layout. This is expected as the angles between the preceding and succeeding layers decrease. Notice again that there are no outliers. An easier-to-comprehend representation of this boxplot graph can be seen on the right-hand side of Figure 5-2 above.

One can clearly see that a good trend line can be constructed from the boxplot graph. It is however interesting to observe that either the $[10/-80]_R$ layout values are too high, or the $[5/-85]_R$ layout values are too low, or the $[0/90]_R$ layout values are also too high. This may be attributed to the placement of the specimens within the MTS Landmark®. However, had this been the case the impact of such inaccurate experiments would have been more notable when comparing all three

material property graphs. Thus, it can be concluded that although human error does play a role, the influence can be seen as negligible when all the results are considered as a whole.

Furthermore, this graph is similar to a usual Young's modulus versus the angle between fibre directions of other fibre composite materials. Therefore, along with the unidirectional layout this combination might also be seen as a laminate composite that complies with the CLT.

5.1.1.3 45° Combination

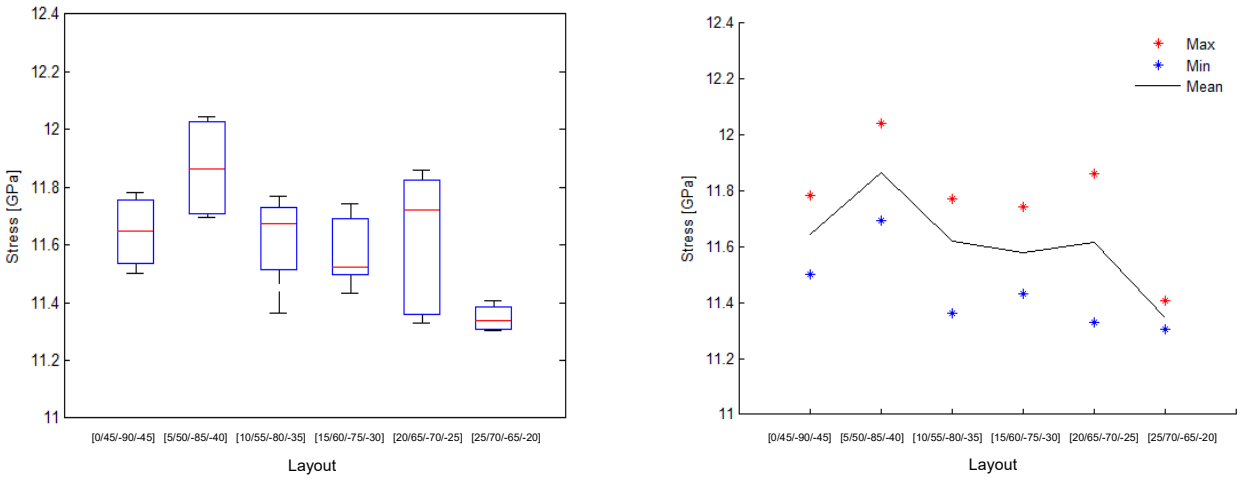

Figure 5-3: Elastic modulus of 45° combinations (boxplot and line graph)

As the angles between the preceding and succeeding layer decrease, so the variances of all the different layout combinations within each category decrease. This is evident from the above boxplot. Again, no outliers can be seen. It is interesting to note that the $[5/50/-85/-40]_R$ layout delivered the highest overall modulus of elasticity, which can be contributed to the fact that there are not one $[90]_R$ (weakest) layer and two $[5]_R$ (almost the strongest) layers – whereas the $[0/45/-90/-45]_R$ layout has two $[90]_R$ layers and also only two strongest layers. Figure 5-3 above shows no apparent trend-line other than a widespread letter 'M' (see right-hand side of the figure).

This seemingly no-trend-line graph can be explained by reasoning that the only two odd data points, which ensure a gradual decrease in the graph, are those of $[5/50/-85/-40]_R$ and $[20/65/70/-25]_R$ (both too high). The same explanation in the previous paragraph can be used for high moduli of elasticity for these two layouts. Note how the last two layout combinations, $[20/65/70/-25]_R$ and $[25/70/-65/-20]_R$, may have been expected to have the same results, but did not. This proves that the layer sequence plays an essential role within the CFF technology.

5.1.1.4 30° Combination

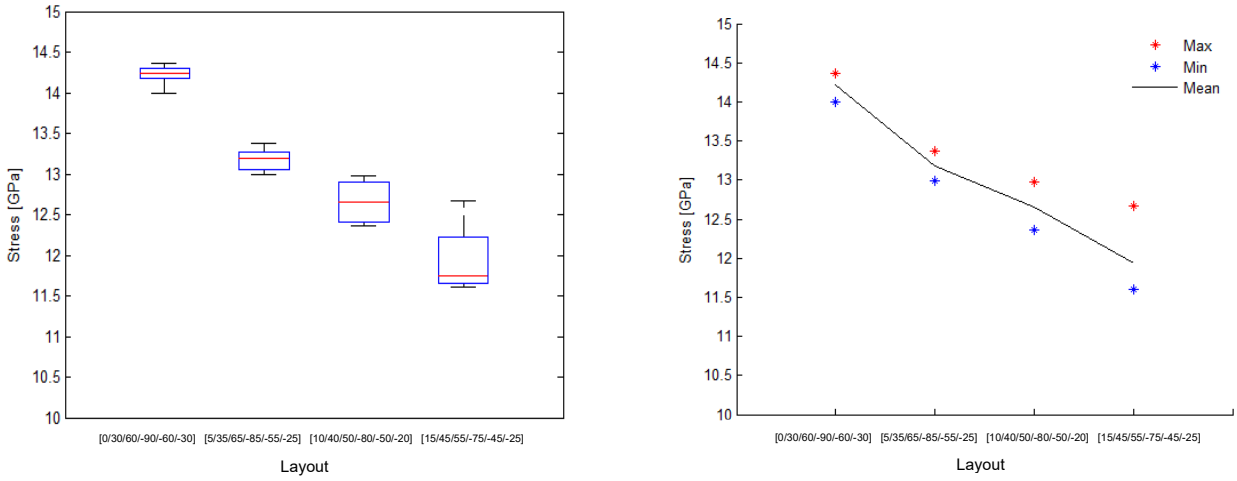

Figure 5-4: Elastic modulus of 30° combinations (boxplot and line graph)

Notice the observable decrease in the graph. This shows that the first two layers, and ultimately the last two layers (as these angles are repeated), had a noticeable impact on the results. The reason for that statement is the fact that angles of the two layers increase (away from 0°) and henceforth the strength also decreases. This almost linear decrease can be seen in the figure on the right-hand side. This ends the discussion on the modulus of elasticity. Next, the yield strength of all four different combination categories are discussed.

5.1.2 Yield strength

The yield strength and the modulus of elasticity result trend lines will not always be directly related to one another. Upon examining Figure 3-1 it is clear that the yield point can be located at different points on either a linear or non-linear graph. This means that no directly proportionate relationships can be pinpointed to match the previous section's graphs, which follow below.

5.1.2.1 Unidirectional

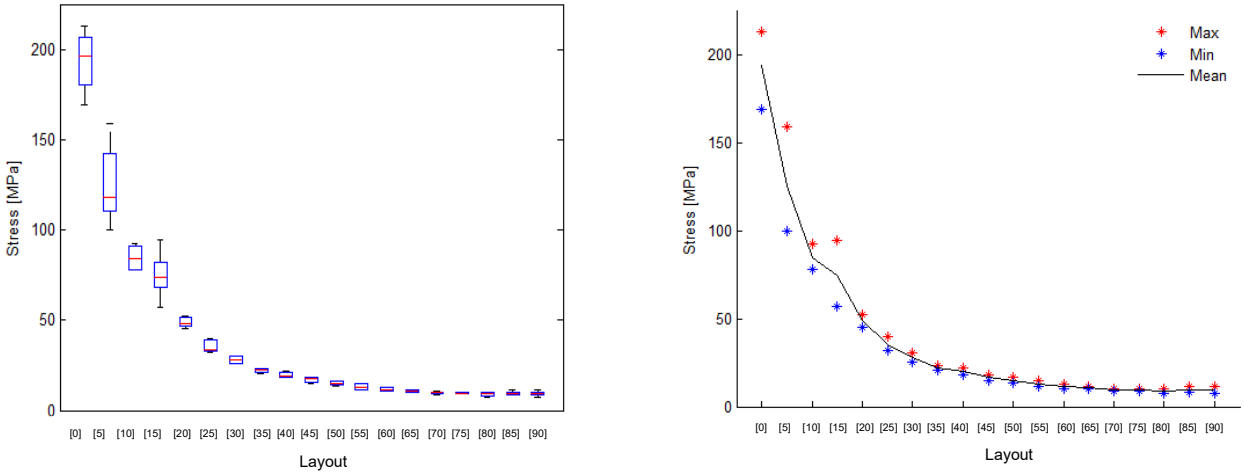

Figure 5-5: Yield strength of unidirectional layout (boxplot and line graph)

The same explanation and reasons for the x-axis, outliers, boxplot, and trend-lines can be given when comparing this graph with Figure 5-1. Note how the YS values begin to diverge also from $[50]_R$ and onward. It is clear from the figure above that the only possible problematic layer combination is that of $[15]_R$. Upon examining Figure A-9 (under section A.1.4) it is clear that varied yield strength values are present. See the cited section for a detailed explanation. Other than this layer combination, the graphs appear to be smooth.

5.1.2.2 90° Combination

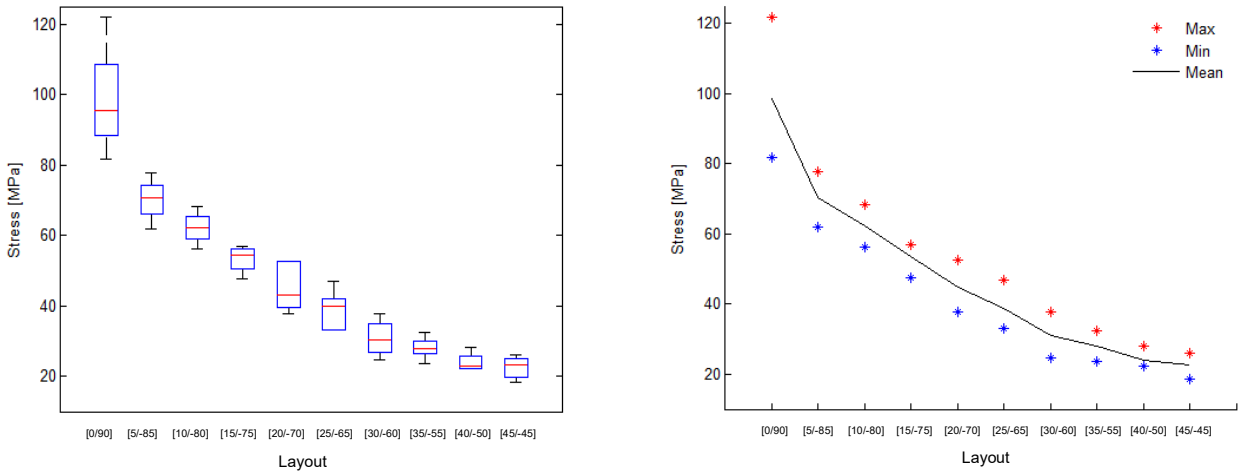

Figure 5-6: Yield strength of 90° combination (boxplot and line graph)

The same comments apply to this graph as with the previous two – decrease in YS is evident and is directly proportionate to the stronger direction of the strands (those closest to 0°). Thus, this graph is similar to the modulus of elasticity within the same layout combination category in the sense that it decreases. When the above graphs are compared with the modulus of elasticity

(Figure 5-2), it seems as though the layout combination with the biggest influence is the first one (furthest on the left side). This indicates that CFF material is also direction-dependent.

5.1.2.3 45° Combination

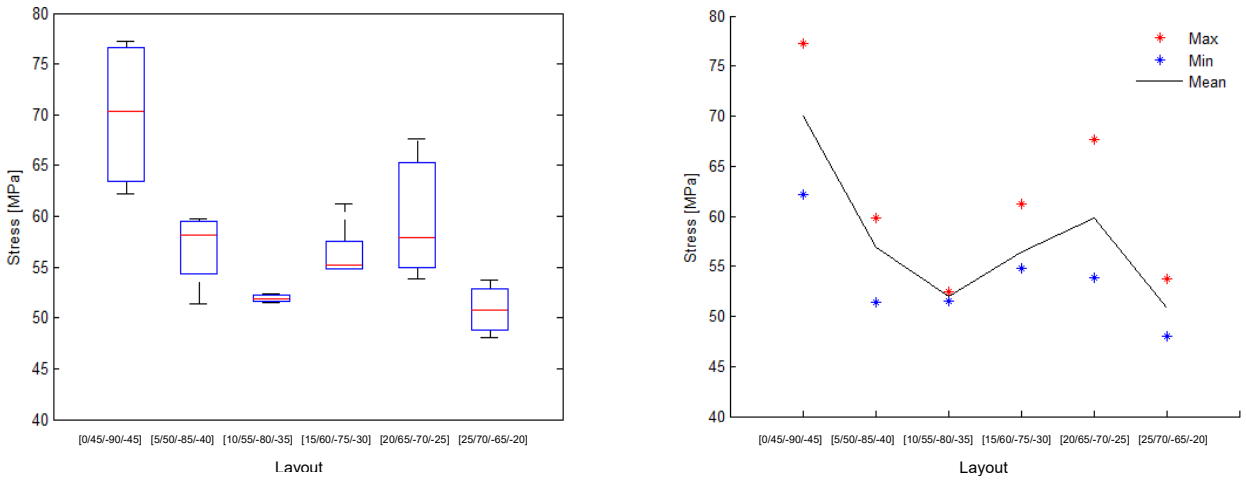

Figure 5-7: Yield strength of the 45° combination (boxplot and line graph)

The same tendency under subsection 5.1.1.3 in respect of the variances in the results can be observed here. Note also the shape of the trend-line graph on the right-hand side.

5.1.2.4 30° Combination

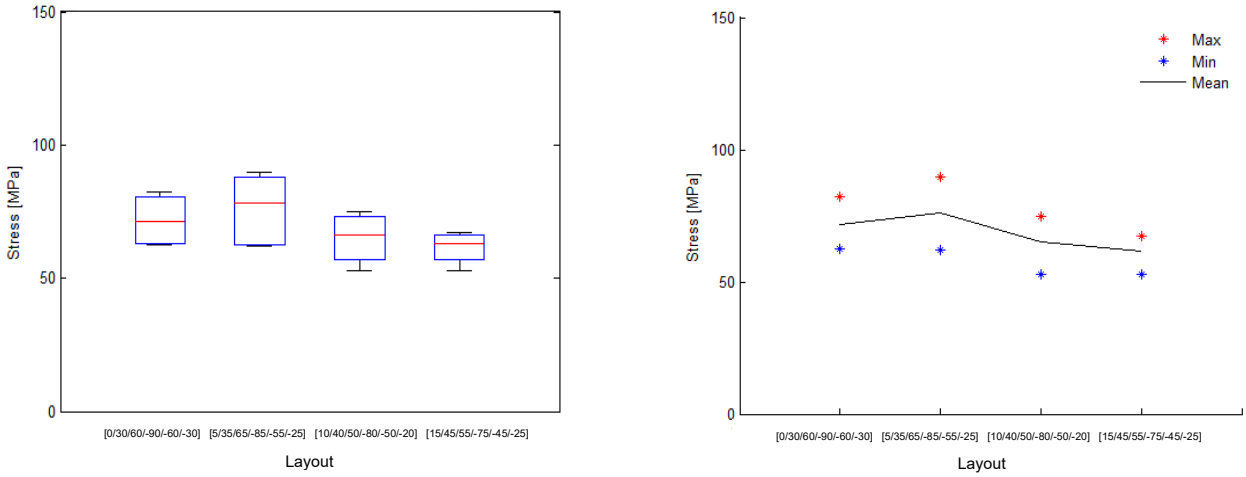

Figure 5-8: Yield strength of the 30° combination (boxplot and line graph)

The YS for all the layout combinations within the 30° combination category seem to be almost identical, proving that a decrease in layer-to-layer angles will produce less variance within the strength results. This almost-horizontal line is evident in the graph on the right-hand side. Note how nearly linear this graph is as well as the modulus of elasticity for the same layout combination (Figure 5-4).

5.1.3 Ultimate tensile strength

The UTS and the YS graph patterns correspond. This observation can be made when Figure 3-1 under subsection 3.1.3 is examined, and it is also evident when the graphs under this section are compared with the previous YS graphs accordingly. The patterns of the first three graphs are exactly like the YS of the respective layout combinations, while the last graph (30° combination) is the only one for which this statement is not valid. However, the latter graph's pattern appears to be the same as that of its modulus of elasticity graph.

All relative explanations and discussions in respect of the x-axis, outlier, boxplot, and trend-lines can again be concluded as in the case with the previous two main material property headings. The UTS results are used as input values for LAP and are henceforth the only material parameter compared with the CLT. Results obtained from this comparison automatically indicate whether the YS values match (because of the similarity in the graphs' trend-lines), and eventually whether the same conclusion can be made with Young's modulus.

5.1.3.1 Unidirectional

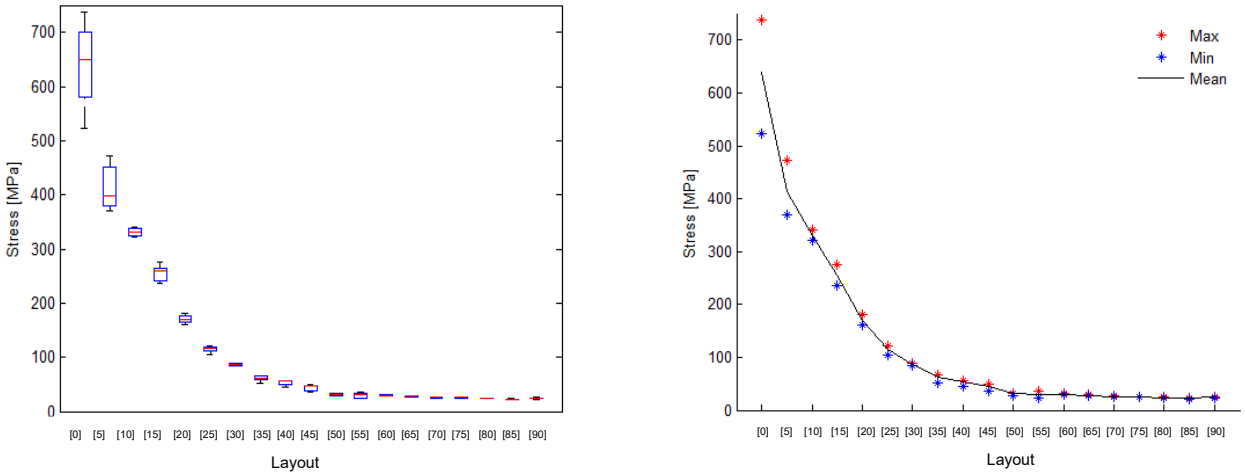

Figure 5-9: UTS of the unidirectional layout (boxplot and line graph)

When the above figure is compared with the YS of the same layout (see Figure 5-5), a clear similarity in the trend-lines can be seen. Notice how the graph also seems to converge after $[50]_R$. The above trend-line graph shows a smooth flow with only the $[5]_R$ layout combination's value appearing to be too low.

When calculating the UTS of the pure carbon fibre layers (without nylon) based on the predictable mathematical model (see Chapter 7), it is clear that a layer combination between 40° and 45° matches the UTS of pure nylon (being 48.76 MPa). Every CFF (whole specimen, with nylon) UTS value above 45° is higher than its corresponding UTS value without nylon, while every CFF UTS

value below 40° is lower than its corresponding UTS value without nylon. This can be explained by the fact that the nylon both strengthens and weakens the overall UTS of the specimens respectively. This is better explained with the aid of the following table (UTS values are in MPa):

Table 5-1: CFF specimen UTS values with and without nylon

Degree	Mean UTS with nylon (Whole specimen)	Mean UTS without nylon (Unidirectional layer CFF)	% Stronger (Without vs with nylon)
0	639.90	787.69	1.23
5	450.00	550.31	1.22
10	331.14	401.74	1.21
15	240.00	287.81	1.20
20	170.60	201.06	1.18
25	120.00	137.81	1.15
30	86.42	95.84	1.11
35	66.00	70.31	1.07
40	**53.22**	**54.34**	**1.02**
45	**43.86**	**42.64**	**0.97**
50	38.00	35.31	0.93
55	33.50	29.69	0.89
60	29.99	25.30	0.84
65	27.50	22.19	0.81
70	25.40	19.56	0.77
75	24.00	17.81	0.74
80	23.00	16.56	0.72
85	23.20	16.81	0.72
90	24.55	18.50	0.75

5.1.3.2 90° Combinations

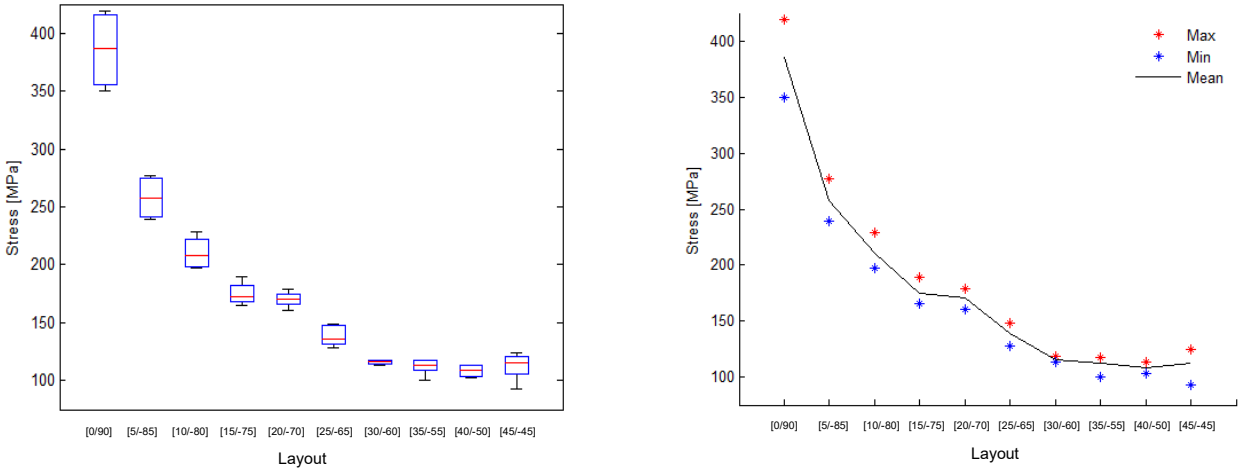

Figure 5-10: UTS of the 90° combination (boxplot and line graph)

The above graph illustrates a decrease in the UTS as the strongest direction (closest to 0°) moves away from 0°. This trend-line can also be seen with the YS of this specific layout combination category. Observe from the figure above how the $[0/90]_R$ and $[20/-70]_R$ UTS values appear to be

too high. The first-mentioned layout can be attributed to the fact that it contains four layers with a strand direction of 0°. The $[20/-70]_R$ layout combination made for interesting results in general (see section A.2.5) and can be seen as the transition phase between the first four layout combinations and the last five within this category.

5.1.3.3 45° Combination

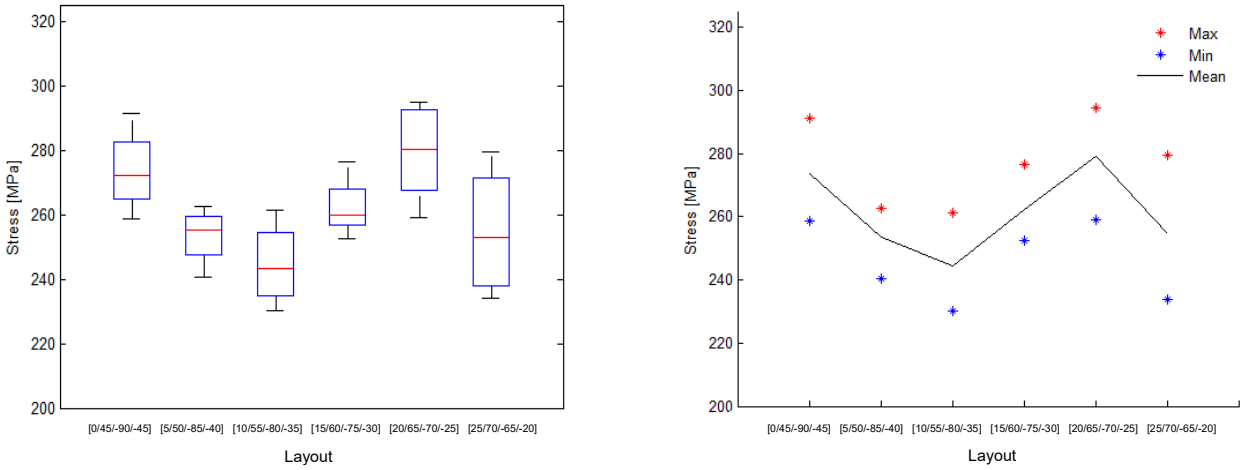

Figure 5-11: UTS of the 45° combination (boxplot and line graph)

These results, represented in the boxplot graph above, have the same pattern as the YS of the same layout combination category (see Figure 5-7) – especially when the trend-line graphs are considered. Observe how the $[20/65/-70/-25]_R$ seems to have the highest UTS values rather than the $[0/45/-90/-45]_R$ (without test 1's results reflected). This can be explained by examining Figure 5-9, for which the $[20/65/-70/-25]_R$ layout has two layers of 20° and two of 25° and the remaining four layers all being greater than 50°. Thus, this layout can be expected to have a higher UTS than the $[0/45/-90/-45]_R$ layout because the latter layout has two layers that are far from the 50° convergence mark.

5.1.3.4 30° Combination

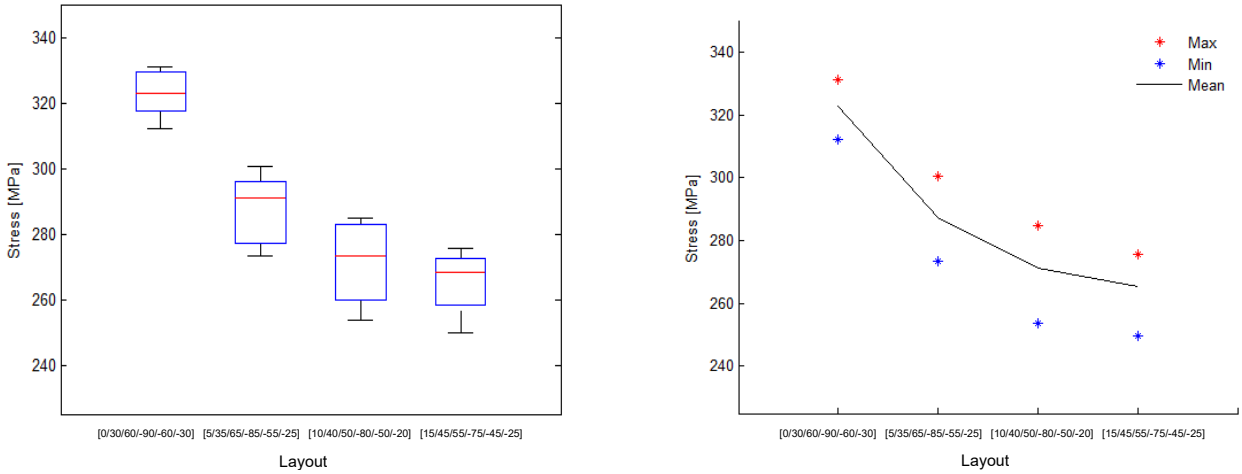

Figure 5-12: UTS of the 30° combination (boxplot and line graph)

The UTS of the 30° combination yielded insightful results when compared with its YS graph. Observe in the above graph how it decreases but with the YS graph it almost remains horizontal. This UTS graph looks similar to its modulus of elasticity graph (see Figure 5-4). More details and explanation can be seen under section A.4.

Chapter 5 provided a summary of the three main material property results with the four different layout combination categories. These results included the modulus of elasticity, yield strength, ultimate tensile strength, and relevant discussions. Chapter 6 investigates whether these results do comply with classical laminate theory.

CHAPTER 6

COMPARISON OF CONTINUOUS FIBRE FABRICATION RESULTS WITH THE CLASSICAL LAMINATE THEORY

This chapter compares the results in Chapter 5 with the classical laminate theory to investigate whether CFF materials can be regarded as laminate materials. This is done using LAP with the most applicable experimental data as input values.

6.1 LAP

In short, LAP (Laminated Analysis Program) is a software tool for the design and analysis of composite laminate material and the solution algorithms employed are based on the classical laminate theory [48]. This software forms part of the verification aspect of this dissertation, as it is used to investigate whether CFF material complies with CLT or not. The following subheadings deal with the input values and the overall interface of LAP.

6.1.1 Materials

The first parameter input value within LAP discussed is that of the materials. In LAP the material properties can be either linear or non-linear (see Figure 6-1 below).

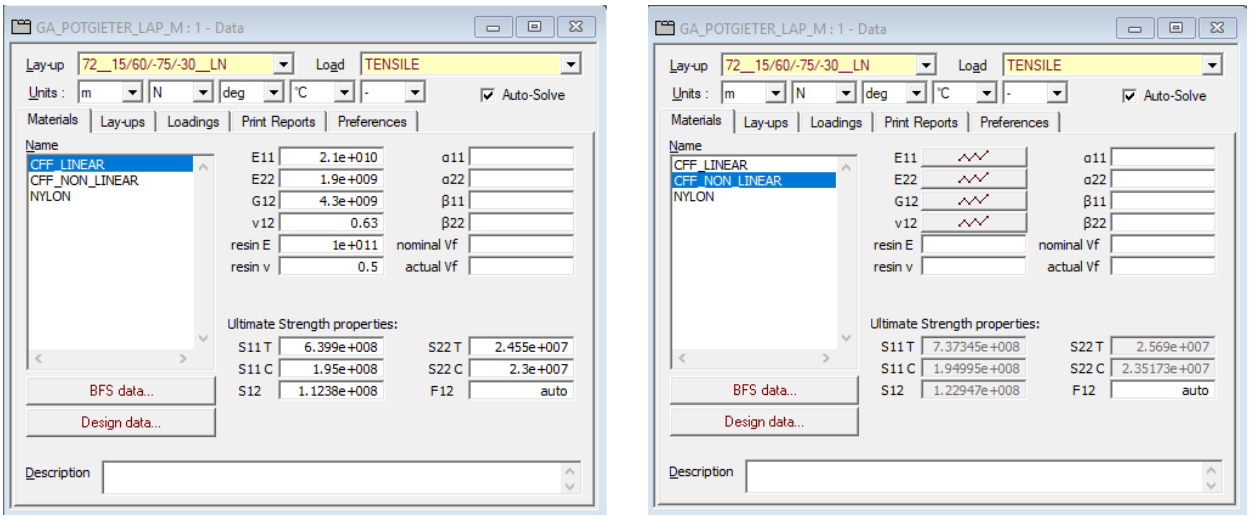

Figure 6-1: Material inputs in LAP

When the CFF material is assumed to be linear, only set values are necessary. These values can be seen on the left-hand side of the figure above and it includes values such as the E11, E22, G12 (stiffness moduli), v12 (Poisson's ratio), resin E and v (resin stiffness modulus and Poisson's ratio), S11T, S22T (UTS and UCS of $[0]_R$), S11C, S22C (UTS and UCS of $[90]_R$), S12 (UTS of

$[45/-45]_R$) and F12 (force of $[45/-45]_R$). The parameters that are left empty include the a11 and a22 (thermal expansion coefficient in the $[0]_R$ and $[90]_R$), B11 and B22 (moisture expansion coefficients), and the nominal and actual vf (fibre volume fractions). These values were not calculated during the experiments performed as they have little to no effect on the final UTS values of the results in LAP. The average results from Chapter 5 were used as input values.

When the CFF material is assumed to be non-linear, only the first four parameters (E11, E22, G12, and v12) are needed for a complete investigation. However, in this case no set values can be given for these parameters and need to be given in a non-linear fashion. Moreover, with LAP the non-linear properties must always be defined as secant. It is important to note that, unlike the linear input values, the maximum values of the single $[0]_R$, $[45/-45]_R$, and $[90]_R$ were used. This is done to ensure an accurate representation of the secant property value versus the stress. It is not possible or accurate to take an average value for these inputs. Figure 6-2 below shows a typical graph representing all direction 22's secant values.

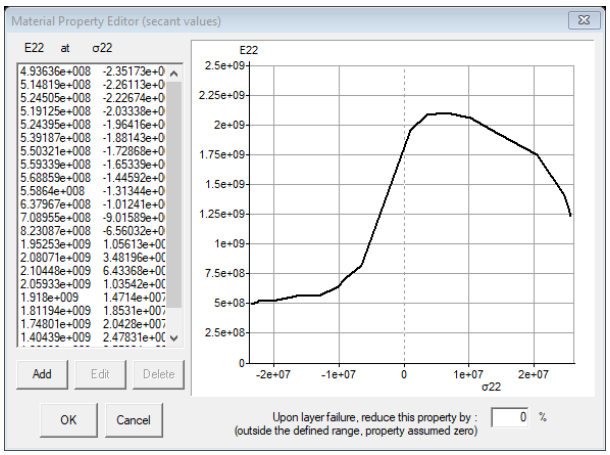

Figure 6-2: Typical non-linear graph constructed within LAP

Note that the graph displays negative as well as positive values of the σ22 stress. The former were obtained with compression tests according to the ASTM D695 standard while the latter values are the tensile strength results for the unidirectional $[90]_R$ combination category (see Section 5.1 and A.2.1 for details). From these values together with the E11, G12, and v12 values, the S11T up to the S12 values are automatically calculated in LAP (see right-hand side of Figure 6-1). G12 values are calculated using the following equation:

$$G_{12} = \frac{4}{\frac{4}{E_{12}} - \frac{1}{E_1} - \frac{1}{E_2} + \frac{2\nu_{12}}{E_1}} \qquad \text{Equation 6-1}$$

The other material seen in Figure 6-1 is nylon. The properties of this material are required for lay-up purposes (see subsection 6.1.2). The nylon material properties are assumed to also be linear, however, these values have little to no effect on the final results in LAP, as only the first and last layers (0.000125 m in thickness) consist of nylon (see Section 4.1).

6.1.2 Lay-ups

The lay-up tab is used to view and edit the lay-up properties. It is here where the internal layout of the carbon fibres (subsection 4.2.1) is defined. The following figures show typical layouts of a linear and non-linear approach.

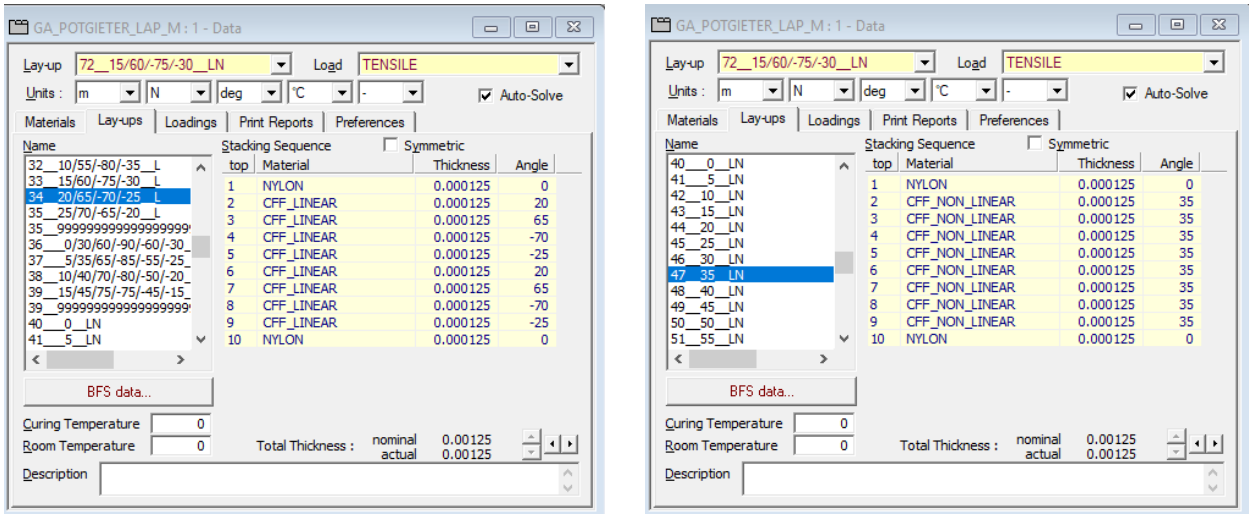

Figure 6-3: Layup inputs in LAP

Observe that layers one and ten are nylon, while the eight layers in the middle are considered to be either CFF linear or CFF non-linear (material properties under subsection 6.1.1). The thickness was set on 0.125 mm (layer height of the Markforged Mark Two), while the angle is simply the layout angles with respect to 0°.

6.1.3 Loadings

Within the loading tab all possible loadings can be edited. These loadings include the strain, force, and moment in all three directions. However, only the strain within the x-direction (the tensile testing direction) are used and it is set at a value of 30% (the maximum for all tests). This was determined by examining the results with a force in the x-direction against that of a strain in the same direction. The results show that a strain type of loading input is more accurate and was therefore used. The steps-field defines the number of equal increments used to carry out a non-linear solution and was set to be 20. This number of steps is sufficient once a strain loading is given [48]. The following figure shows the visual display of the loadings tab:

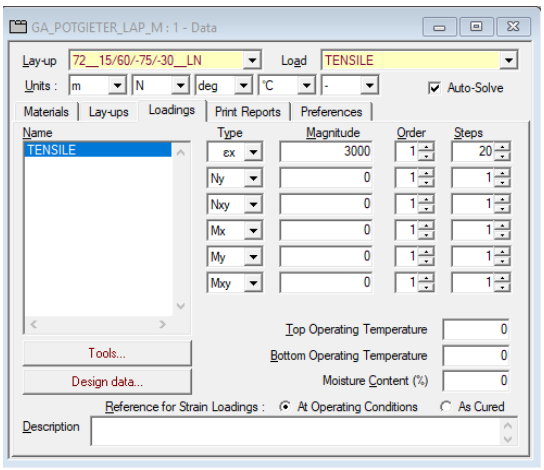

Figure 6-4: Loading inputs in LAP

Notice that no order, top operating temperature, bottom operating temperature, or moisture content is needed. It is difficult to determine these values as they vary throughout the whole printing process.

6.1.4 Preference

The strength calculations, thickness and stiffness corrections, and the non-linear solutions all form part of the preference tab in LAP. The rule of mixtures is set to be the volume fraction correction method while the failure criteria used to track local failure are the most important variable used during the comparison process. These criteria include Tsai-Wu, Tsai-Hill, Hoffman, maximum stress, and maximum strain. All LAP results are shown according to these five different criteria for thorough comparisons in the sections to follow. The next figure shows the display with the failure criteria set on Hoffman:

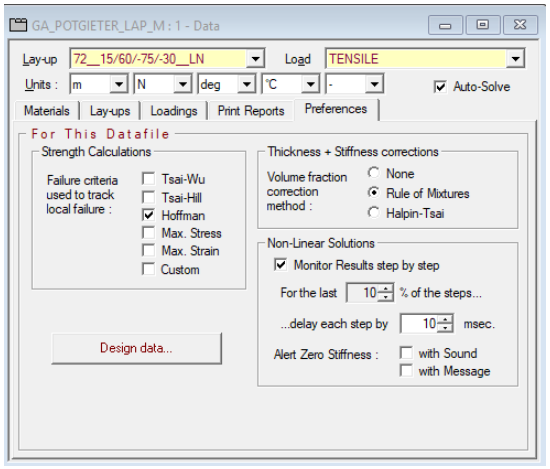

Figure 6-5: Different failure criteria within LAP

6.1.5 General results window

The general results window shows all the general results calculated by LAP. These results include the effective stiffness, effective coefficients, expected strengths, load vector, strain vector, biaxial flexural strength (BFS) criterion results, ABD matrix, and the inverse ABD matrix. Only the '+Nx' (ultimate load in the x-direction) value under the expected strength was used because only the UTS values were used for verification purposes and inputs in LAP. Figure 9-9 below shows the results of the non-linear $[15/60/-75/-30]_R$ layout combination with maximum strain as the failure criteria:

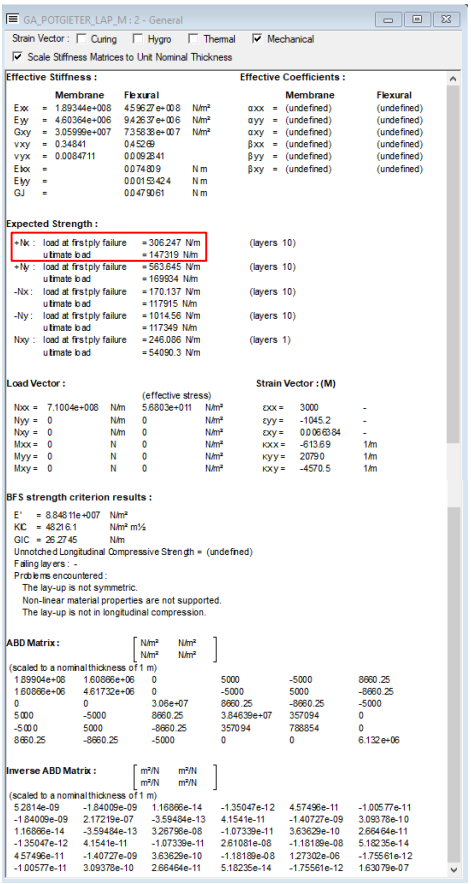

Figure 6-6: General results window in LAP

Notice that the strain vector (at the top of the window) is set on mechanical. The other three options (curing, hygro, and thermal) have no influence on the ultimate load in the +Nx direction.

6.2 Results

All possible results, 390 in total, are given in table and graph format under the following headings. These results are compared with the values calculated in Chapter 5, followed by relevant discussions.

6.2.1 All 390 results

All the results are given in Table 6-1 below are colour-coded within each layout category and failure criterion (with green being the highest value and red the lowest) for visual comparison (notice that numbers are without decimals for layout-fitting purposes).

Table 6-1: All 390 specimens' UTS results

			Linear (all values in MPa)						Non-Linear (all values in MPa)					
		Deg	Mean	Tsai-Wu	Tsai-Hill	Hoffman	Max Stress	Max Strain	Max	Tsai-Wu	Tsai-Hill	Hoffman	Max Stress	Max Strain
Unidirectional		$[0]_R$	640	640	640	640	640	404	737	737	737	737	737	2e6
		$[5]_R$	413	660	570	609	645	470	473	765	648	703	743	0
		$[10]_R$	331	640	407	495	657	657	340	746	448	566	719	0
		$[15]_R$	255	458	264	335	366	449	276	521	284	374	384	0
		$[20]_R$	171	271	175	215	210	350	181	298	186	234	220	0
		$[25]_R$	115	168	123	144	137	186	121	180	130	154	144	0
		$[30]_R$	86	113	91	102	98	118	89	121	96	109	103	0
		$[35]_R$	61	83	71	77	75	84	67	87	75	82	78	0
		$[40]_R$	53	64	57	61	59	65	57	67	60	64	62	0
		$[45]_R$	44	52	48	50	49	52	50	54	50	53	51	0
		$[50]_R$	31	43	41	42	42	44	33	46	43	45	44	0
		$[55]_R$	30	38	36	37	37	38	35	39	38	39	38	0
		$[60]_R$	28	33	32	33	33	33	29	35	34	35	34	0
		$[65]_R$	30	30	30	30	30	30	31	32	31	31	31	0
		$[70]_R$	25	28	28	28	28	28	26	29	29	29	29	0
		$[75]_R$	26	26	26	26	26	26	27	28	27	28	28	0
		$[80]_R$	22	25	25	25	25	25	24	27	26	27	26	0
		$[85]_R$	24	25	25	25	25	25	25	26	26	26	26	0
		$[90]_R$	25	25	25	25	25	25	26	26	26	26	26	375
Combinations	90°	$[0/...]_R$	386	289	208	206	203	256	419	285	285	285	285	760
		$[5/...]_R$	258	271	143	175	202	258	277	273	254	272	287	0
		$[10/...]_R$	210	232	132	158	175	254	229	244	202	240	278	0
		$[15/...]_R$	175	191	120	142	170	170	190	210	159	205	187	0
		$[20/...]_R$	170	157	120	137	154	154	179	178	148	172	169	0
		$[25/...]_R$	139	142	122	127	140	154	148	170	137	160	163	0
		$[30/...]_R$	116	140	125	133	146	166	118	166	143	156	178	0
		$[35/...]_R$	112	151	128	141	153	179	118	185	151	170	185	0
		$[40/...]_R$	108	165	133	150	166	208	114	209	160	188	212	0
		$[45/...]_R$	112	182	140	162	181	225	124	239	173	209	246	0
	45°	$[0/...]_R$	274	143	106	127	132	150	291	89	107	96	113	174
		$[5/...]_R$	253	143	112	132	131	185	263	93	106	99	115	226
		$[10/...]_R$	245	163	120	136	142	203	261	109	111	115	117	199
		$[15/...]_R$	262	165	129	144	151	179	276	115	118	121	119	147
		$[20/...]_R$	279	194	136	154	170	186	295	138	135	131	135	128
		$[25/...]_R$	255	194	136	154	170	186	280	138	135	131	135	128
	30°	$[0/...]_R$	323	297	194	213	252	257	331	133	118	142	123	201
		$[5/...]_R$	287	260	183	183	234	251	300	109	98	120	103	160
		$[10/...]_R$	271	223	142	169	200	230	285	91	85	96	88	138
		$[15/...]_R$	265	201	132	160	173	198	276	94	78	91	79	124

From the above table a few conclusions can be made. First, within the unidirectional layout almost all failure criteria displayed behaviour in a likewise manner with the exception of the maximum strain in the non-linear approach. This trend weakens as the combinations increase from 90° to 30°. To better visualise these results, graphs are constructed to compare the five failure criteria with the experimental results (linear approach – mean values, and non-linear approach – maximum values).

6.2.2 Graphs and percentage difference

As discussed in the previous paragraph, graphs are constructed together with the percentage differences of the five failure criteria to thoroughly compare the relative results.

6.2.2.1 Unidirectional

The following two figures show all six UTS graphs in one in respect of the respective linear and non-linear approaches, with the percentage differences between each of the five failure criteria with respect to the mean or maximum UTS values to follow.

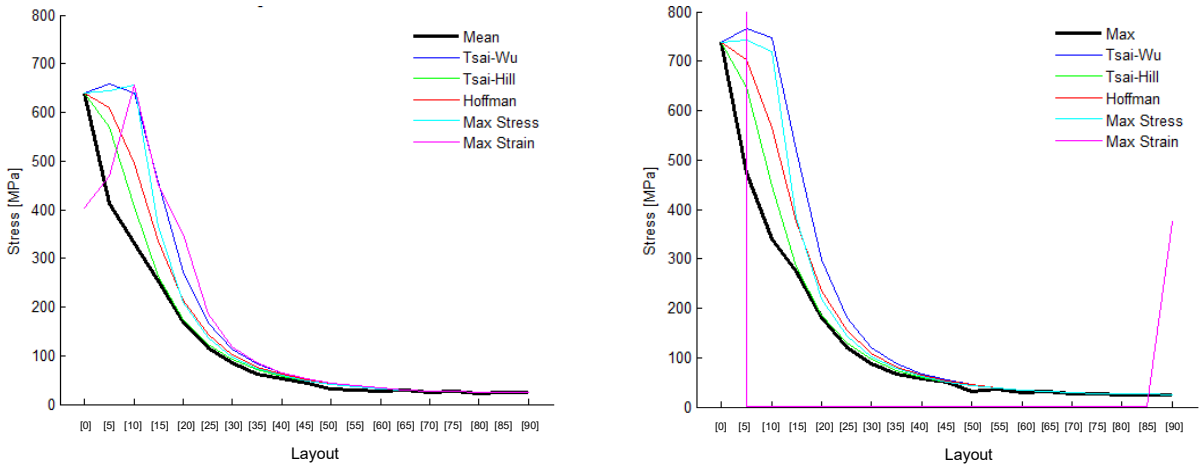

Figure 6-7: (a) Linear and (b) Non-linear unidirectional layout combination LAP results

The two graphs in Figure 6-7 above reveal that almost all the failure criteria have the same trend line, with the Tsai-Hill being the closest to the black graph (the mean or maximum). This is also evident in examining the percentage difference table:

Table 6-2: LAP percentage difference of unidirectional UTS values of all failure criteria

	Deg	Linear (all values in Mpa)						Non-Linear (all values in Mpa)					
		Tsai-Wu	Tsai-Hill	Hoffman	Max Stress	Max Strain	Average % Difference	Tsai-Wu	Tsai-Hill	Hoffman	Max Stress	Max Strain	Average % Difference
Unidirectional	$[0]_R$	0	0	0	0	37	0	0	0	0	0	100	0
	$[5]_R$	60	38	47	56	14	50	62	37	49	57	100	51
	$[10]_R$	93	23	50	98	98	66	119	32	66	111	100	82
	$[15]_R$	80	3	32	44	76	40	89	3	36	39	100	42
	$[20]_R$	59	3	26	23	105	28	65	3	30	21	100	30
	$[25]_R$	45	7	25	19	62	24	49	7	27	18	100	25
	$[30]_R$	31	6	18	14	37	17	36	9	23	16	100	21
	$[35]_R$	34	16	26	21	37	24	31	12	22	17	100	21
	$[40]_R$	20	8	14	12	21	14	19	6	13	9	100	12
	$[45]_R$	18	9	14	12	19	13	9	0	5	2	100	4
	$[50]_R$	41	34	38	36	42	37	40	33	37	35	100	36
	$[55]_R$	26	22	24	23	27	24	12	8	10	9	100	10
	$[60]_R$	19	16	18	17	19	17	21	18	20	19	100	19
	$[65]_R$	1	1	0	0	1	1	1	0	1	0	100	1
	$[70]_R$	10	9	10	10	10	10	14	13	13	13	100	13
	$[75]_R$	3	2	2	2	3	2	3	2	3	3	100	3
	$[80]_R$	13	13	13	13	13	13	13	12	13	12	100	12
	$[85]_R$	3	3	3	3	3	3	3	3	3	3	99	3
	$[90]_R$	0	0	0	0	0	0	0	0	0	0	100	0
Average:		29	11	19	21	33	20.1	31	10	19	20	100	20.2

Please note that the last column of both the linear and non-linear sections are calculated without the maximum strain values because of the final average of this failure criteria being the highest in both, especially in the non-linear group, and are thus disregarded in both when the overall average is calculated. When both groups (linear and non-linear) have the same weakest failure criteria, those criteria are disregarded when calculating the average percentage difference. This table and Figure 6-7 clearly indicate the first three best-suited failure criteria within a specific group as follows (in descending order): Tsai-Hill in non-linear, Tsai-Hill in linear, and Hoffman in linear. Furthermore, observe that the overall percentage difference of the linear group is 20.1% while the non-linear group's value is 20.2%. This means that CFF material may tend more towards being linear than non-linear.

6.2.2.2 90° Combination

From the main table (see Table 6-1) it is clear that all five failure criteria had different tendencies in the values than the mean and maximum values within the two groups. Again, the maximum strain column within the non-linear group seems to be the oddest and not close to the other. This is evident when the two group's graphs are compared.

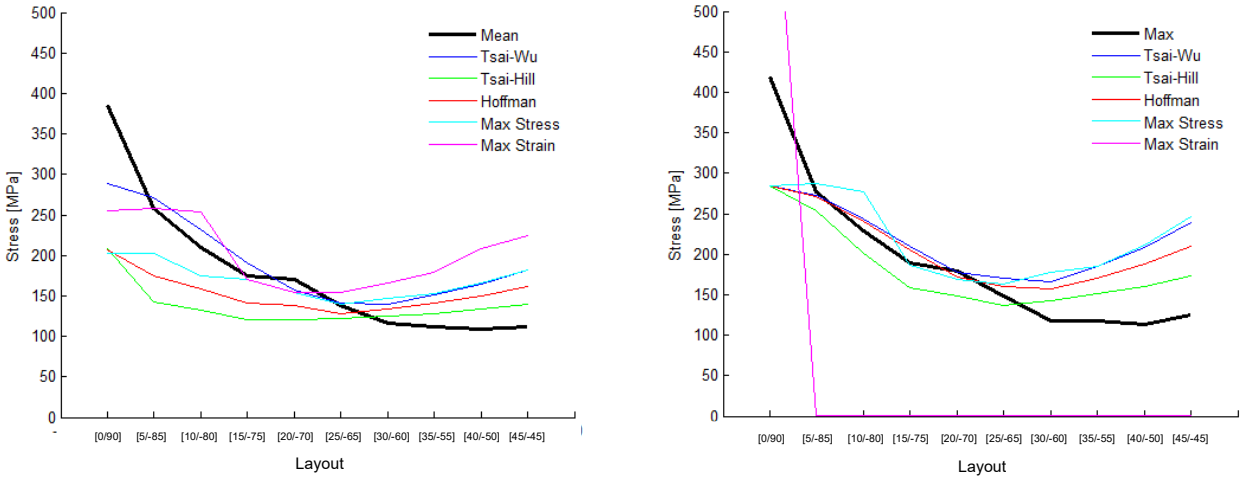

Figure 6-8: (a) Linear and (b) non-linear 90° layout combination LAP results

The same conclusion can be made for the trend line as those of the unidirectional layout's graphs. However, here it is somewhat more difficult to allocate the best failure criteria based only on the graphs. Table 6-3 below provides greater clarity.

Table 6-3: Percentage difference of 90° UTS values of all failure criteria within LAP

	Deg	Linear (all values in %)						Non-Linear (all values in %)					
		Tsai-Wu	Tsai-Hill	Hoffman	Max Stress	Max Strain	Average % Difference	Tsai-Wu	Tsai-Hill	Hoffman	Max Stress	Max Strain	Average % Difference
90° Combination	$[0/90]_R$	25	46	47	47	34	41	32	32	32	32	81	32
	$[5/-85]_R$	5	45	32	22	0	26	2	8	2	3	100	4
	$[10/-80]_R$	10	37	25	17	21	22	6	12	5	21	100	11
	$[15/-75]_R$	9	31	19	3	3	16	11	16	8	2	100	9
	$[20/-70]_R$	8	29	19	9	9	17	1	17	4	6	100	7
	$[25/-65]_R$	2	12	8	1	11	6	14	8	8	10	100	10
	$[30/-60]_R$	21	8	15	26	43	17	41	21	33	51	100	36
	$[35/-55]_R$	34	15	26	36	60	28	57	28	44	57	100	46
	$[40/-50]_R$	52	23	39	53	92	42	84	41	65	86	100	69
	$[45/-45]_R$	62	25	44	61	100	48	92	39	68	98	100	74
Average:		23	27	27	28	37	26.2	34	22	27	37	98	29.9

Table 6-3 above reveals that the maximum strain column is again the weakest in both groups and is therefore disregarded when the average percentage difference is calculated. The first three best-suited combinations of failure criteria and groups are (again in descending order): Tsai-Hill in non-linear, Tsai-Wu in linear, and Hoffman in non-linear. From this it might appear as though the 90° layout combination category behaves more as a non-linear material. However, calculating the average percentage differences (without the maximum strain values) yields a value of 26.2 % for the linear group while the non-linear group has a value of 29.9%. This indicates that the CFF material might be regarded as a linear material.

6.2.2.3 45° Combination

From Figure 6-9 it is clear that the first four failure criteria have the same tendency while the maximum strain is again the odd one out in respect of the tendency but not the percentage difference (see Table 6-4). This is displayed in the following two graphs:

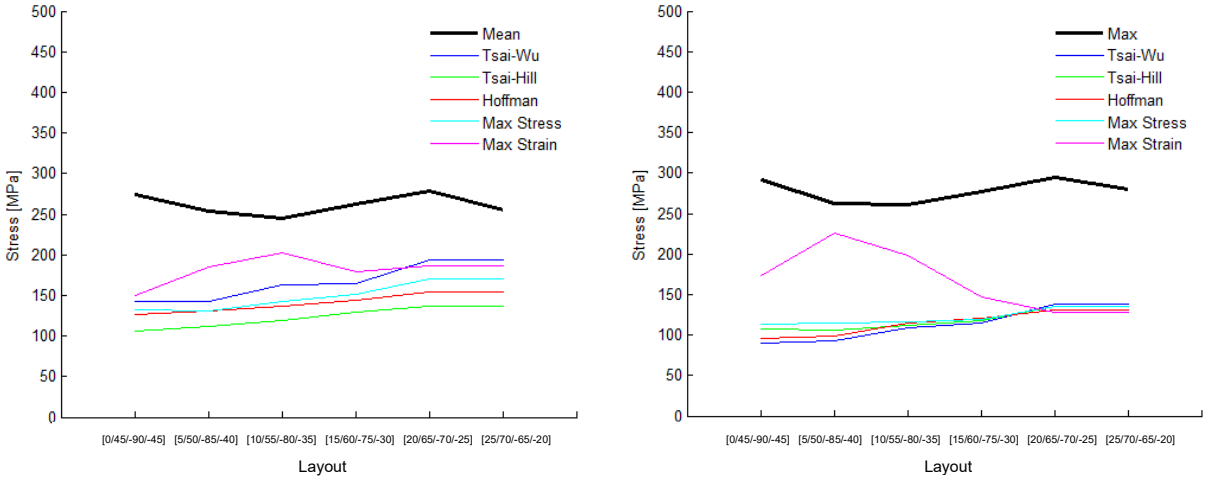

Figure 6-9: (a) Linear and (b) non-linear 45° layout combination LAP results

The graphs in Figure 6-9 above show that all five the failure criteria are not close to the experimental data (black line). However, in both cases the maximum strain is closer to this black line than the other four. Notice how the linear results are overall closer to the experimental results than the non-linear results. This is demonstrated in Table 6-4 below:

Table 6-4: Percentage difference of 45° UTS values of all failure criteria within LAP

		Linear (all values in %)						Non-Linear (all values in %)					
	Deg	Tsai-Wu	Tsai-Hill	Hoffman	Max Stress	Max Strain	Average % Difference	Tsai-Wu	Tsai-Hill	Hoffman	Max Stress	Max Strain	Average % Difference
45° Combination	$[0/45/-90/-45]_R$	48	61	54	52	45	52	69	63	67	61	40	60
	$[5/50/-85/-40]_R$	43	56	48	48	27	45	65	60	62	56	14	51
	$[10/55/-80/-35]_R$	33	51	44	42	17	37	58	57	56	55	24	50
	$[15/60/-75/-30]_R$	37	51	45	43	32	41	58	57	56	57	47	55
	$[20/65/-70/-25]_R$	30	51	45	39	33	40	53	54	55	54	56	55
	$[25/70/-65/-20]_R$	24	46	40	33	27	34	50	52	53	52	54	52
Average:		36	53	46	43	30	41.5	59	57	58	56	39	54

Notice that the weakest failure criteria within the linear case are those of Tsai-Hill and within the non-linear case Tsai-Wu. This means that no failure criteria are disregarded when calculating the average percentage difference. Table 6-4 above shows that the three best situations (in descending order) are: maximum strain in linear, Tsai-Wu in linear, and maximum strain in non-

linear. Again, this shows that the CFF material might be seen as a linear material. This is also evident when the two averages of the average percentage differences are compared (41.5% in linear with 54.0% in non-linear).

6.2.2.4 30° Combination

From Table 6-1 it is clear that all five failure criteria have the same tendency. This is also evident in examining the two graphs in Figure 6-10 below:

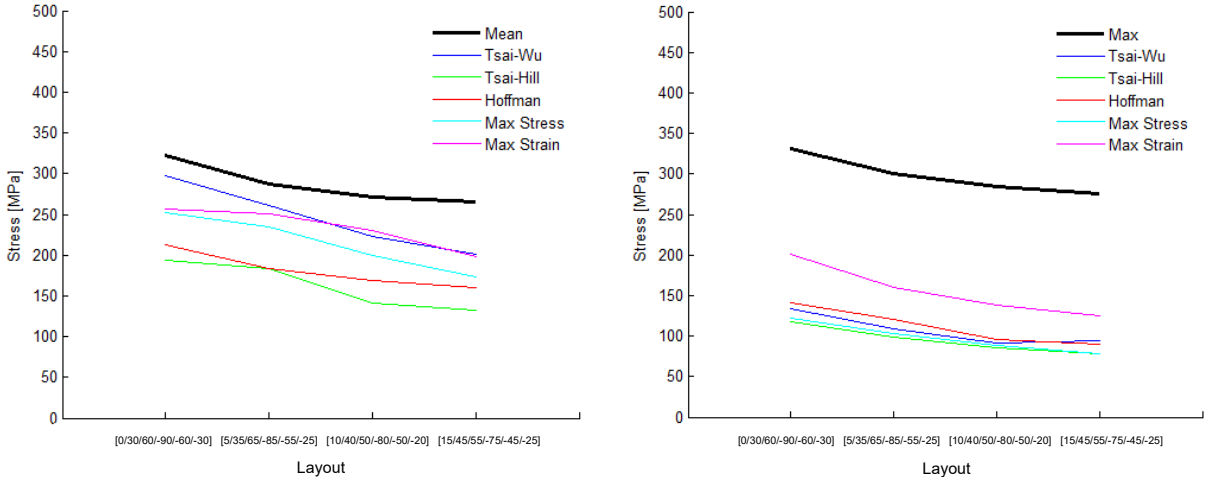

Figure 6-10: (a) Linear and (b) non-linear 30° layout combination LAP results

Notice how the linear results are closer to the black line than the non-linear results. From this the linear results are expected to have the least percentage difference on average. Furthermore, it seems as though the Tsai-Wu criteria are the best within the linear group and the maximum strain within the non-linear group. This can be seen in Table 6-5 below:

Table 6-5: Percentage difference of 30° UTS values of all failure criteria within LAP

	Deg	Linear (all values in %)						Non-Linear (all values in %)					
		Tsai-Wu	Tsai-Hill	Hoffman	Max Stress	Max Strain	Average %	Tsai-Wu	Tsai-Hill	Hoffman	Max Stress	Max Strain	Average %
30° Comb	$[0/30/60/-90/-60/-30]_R$	8	40	34	22	20	21	60	64	57	63	39	55
	$[5/35/65/-85/-55/-25]_R$	9	36	36	19	13	19	64	67	60	66	47	59
	$[10/40/70/-80/-50/-20]_R$	18	48	38	26	15	24	68	70	66	69	52	64
	$[15/45/75/-75/-45/-15]_R$	24	50	40	35	26	31	66	72	67	72	55	65
Average:		15	44	37	25	18	24	64	68	63	67	48	61

Notice that the weakest failure criteria within both groups are those of Tsai-Hill, which are therefore not considered when calculating the average percentage difference. The table shows that overall, the linear results are almost three times more accurate than the non-linear results.

The three best-suited results are therefore (in descending order): Tsai-Wu in linear, maximum strain in linear, and maximum stress in linear. This implies that the CFF material can be regarded as a linear material when the layout of each succeeding layer is 30° from the other.

6.2.3 Summary

In conclusion to the LAP results, Table 6-6 is constructed with discussions to follow:

Table 6-6: Summary of all percentage difference values

	Linear (all values in %)						Non-Linear (all values in %)					
	Tsai-Wu	Tsai-Hill	Hoffman	Max Stress	Max Strain	Average % Difference	Tsai-Wu	Tsai-Hill	Hoffman	Max Stress	Max Strain	Average % Difference
Average of all 39 results:	27	25	27	27	32	28	39	27	32	35	85	41
Average of all four categories:	26	34	32	29	30		47	40	42	45	71	
Overall average:	26	29	30	28	31	28	43	33	37	40	78	38
	No changes:						With possible corrections:					
Average of all 39 results:	27	25	27	27	32	28	37	25	30	33	80	39
Average of all four categories:	26	34	32	29	30		45	38	40	43	67	
Overall average:	26	29	30	28	31	28	41	31	35	38	73	36

The table above shows all percentage differences of all results in a nutshell. The ‘average of all 39 results’ is the average of all unidirectional, 90°, 45°, and 30° combinations within a certain failure criterion. The ‘average of all four categories’ is the average calculated from only the four final average percentage differences of the four different layout categories, while the ‘overall average’ is then calculated as the average of these two values.

One might conclude that the reason for the non-linear results being less accurate than the linear results is that the non-linear inputs are obtained from the maximum experimental values while the linear inputs to LAP are obtained from the mean experimental values. For this reason, the average ratio between the maximum and mean values of the experimental results are calculated and the non-linear values are decreased by that ratio – hence the extra rows and values of the non-linear group labelled ‘with possible corrections’.

The average ratio of the unidirectional layout is calculated as 1.071 – this means that on average, the maximum experimental results are 1.071 times greater than the average results within the

unidirectional layout category. The 90°, 45°, and 30° ratios are 1.066, 1.062, and 1.040 respectively. When these values are taken into consideration by the non-linear results, the bottom right-side of Table 6-6 is obtained. This reveals that it does not make a difference in the overall average results and that the CFF material tends more to behave as a linear material than a non-linear material.

Furthermore, one may come to the obvious conclusion that Tsai-Wu is the best failure criteria in general to use, followed by max stress, and then Tsai-Hill. However, a profounder investigation is required to determine the best suitable failure criteria rather than only considering the average values seen in the table. For this, the number of occurrences of each category's three best results is considered. Table 6-7 below is constructed and shows the number of occurrences of each group (linear or non-linear) together with the five failure criteria within the final top three best-suited results for each category:

Table 6-7: Determination of linearity and failure criteria

	Position:			Total
	1	2	3	
Determination of Linear or Non-Linear:				
Linear	2	4	2	16
Non-Linear	2	0	2	8
Determination of failure criteria:				
Tsai-Wu	1	2	0	7
Tsai-Hill	2	1	0	8
Hoffman	0	0	2	2
Max Stress	0	0	1	1
Max Strain	1	1	1	6

The first position has a value of three points, the second position has a value of two points, and the third position a value of one point. This simple table shows that the behaviour of the CFF material is more likely to be linear and that the best overall failure criteria are that of Tsai-Hill, followed by Tsai-Wu, and then max strain.

Chapter 6 investigated the similarities between the results obtained in Chapter 5 and CLT. The results show that CFF material behaviour is more linear than non-linear, with Tsai-Hill being the best overall failure criteria to use.

CHAPTER 7

MATHEMATICAL MODEL

Chapter 7 discusses a possible solution towards the prediction of the UTS of the CFF material manufactured with the Markforged Mark Two printer. This solution may be used for further investigation to construct a verifiable mathematical model for all CFF materials.

7.1 Mathematical equation

The specimens used for this dissertation had ten layers in total in the middle (see Section 4.1), with the first and last layer being solid nylon. With suitable tensile testing the nylon UTS value was 48.76 MPa throughout the experiments. When the latter value is assumed to remain constant throughout all other CFF constructed specimens, a plausible conclusion can be made in respect of each layer's strength by virtue of the theory that the overall average strength of the specimen is simply the product of all internal layers' strengths added up and divided by the total number of layers, with some explanation supplemented within the formula itself. The following mathematical equation was constructed with explanations to follow. These explanations are dealt with in detail under the appropriate headings.

$$UTS = \frac{(\#_{CM} \cdot UTS_{CM}) + (\#_{comp\ set} \cdot UTS_{theo})}{(\#_{CM} + \#_{comp\ set})} \qquad \text{Equation 7-1}$$

Where:

$\#_{CM}$ - Number of the core material (two nylon layers – see Section 4.1 for details);

UTS_{CM} - UTS of the core material;

$\#_{comp\ set}$ - Number of the complete sets of carbon fibre before repeating;

UTS_{theo} - Theoretical UTS calculated as follows:

$$UTS_{theo} = (UTS_{0^\circ} \cdot A)(cos\alpha + cos\alpha' + cos\alpha'' + \cdots) + (UTS_{90^\circ} \cdot B)(cos\beta + cos\beta' + cos\beta'' + \cdots) \qquad \text{Equation 7-2}$$

with - The number of α and β = $Rounddown\left(\frac{90}{Layout\ Combination}\right) + 1$ Equation 7-3

$$\propto + \beta \ = 90^\circ \qquad \text{Equation 7-4}$$

$$A + B = 1 \qquad \text{Equation 7-5}$$

All values of A can be obtained from the $\frac{UTS_{All\ Single\ Combinations}}{UTS_{0°}}$ graph (Figure 7-2)

where the x coordinates on this graph can be calculated as follows:

$$x_{coordinate} = Mean\ Degree - Ratio\ Degree \quad \text{Equation 7-6}$$

Values of ratio degree can be obtained from Figure 7-6

7.1.1 Number of complete sets of carbon fibre

The number of completed sets of carbon fibre is the number of times the specific layout combination will repeat itself within the limited eight layers. Thus, for instance, within the 90° combination layout category there will be four complete sets of carbon fibre within the eight layers. Table 7-1 below shows all the layout combination categories together with the number of completed sets of carbon fibre within each combination – including the 75°, 60°, and 15° layout combinations specifically selected to construct a complete mathematical model.

Table 7-1: Number of completed sets

Layout Combination Category	Number of completed sets
Unidirectional	8.00
90°	4.00
75°	3.33
60°	2.67
45°	2.00
30°	1.33
15°	0.67

Upon careful examination of the values of the completed sets in Table 7-1 above it is noted that the number is equal to the layout combination divided by 22.5°.

7.1.2 Theoretical UTS calculated

To obtain the internal layers' strengths for the specimen, Figure 7-1 needs to be considered first. It is assumed that the theoretical UTS will eventually be the product of only two main unidirectional layout combination values – the strongest (0°) and the weakest (90°). With these values, the vertical component (UTS theoretical) value can be calculated by using basic trigonometry. The angle between the 0° UTS and the result component is set to be α while β will be the angle between the latter and the 90° UTS line.

The 90° UTS represents the force needed to separate two adjacent strands in a perpendicular manner (marked with a red circle), while the 0° UTS represents the ultimate tensile strength of

the strands in the direction of the fibres. From this, together with the two angles, the theoretical UTS is given by Equation 7-2:

$$UTS_{theo} = (UTS_{0^\circ} \cdot A)(cos\alpha + cos\alpha' + cos\alpha'' + \cdots) + (UTS_{90^\circ} \cdot B)(cos\beta + cos\beta' + cos\beta'' + \cdots)$$

where the number of the αs and βs is explained under subsection 7.1.2.1, and the ratio of A and B are explained under section 7.1.2.2.

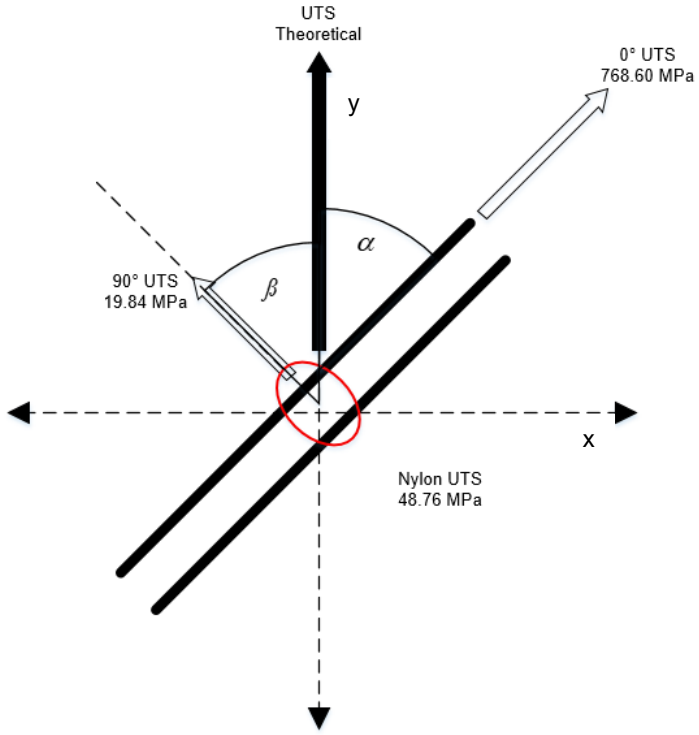

Figure 7-1: Trigonometry representation of the theoretical UTS

7.1.2.1 Alpha and beta

The angles α and β are the angles between the strengths of the strongest and weakest strands with respect to the y-axis (the result component line). For the unidirectional layout there is only one α and one β angle, as all the layers are directly on top of one another. However, during the 90° combination there are two αs and βs, as the succeeding layer has its own two angles. This was the case for all the combination categories. However, it is important to note that only the first two quadrants were acceptable areas for the mathematical model, with the y-axis being the starting point for angle measurements.

Furthermore, it is important to note that a value of 95° is the same as -85°, and because the y component is the only component of interest in the individual layer strand's strength, this value

should be absolute, hence 85°. This means that the values of all the αs and βs will always be positive and less than or equal to 90°. To find the number of αs and βs it is crucial to account for the angles that will repeat themselves more often than the completed sets discussed under subsection 7.1.1. The solution can be found in Equation 7-3:

$$Number\ of\ \alpha\ and\ \beta = Rounddown\left(\frac{90}{Layout\ Combination}\right) + 1$$

To illustrate, a 90° combination will have a number of αs and βs set as two, which means that there will be an α and β as well as an α′ and β′, with α′ and β′ being a certain angle from the preceding α and β based on the layout combination category. It is also important to note that the sum of α and β will always be 90°. The other variable within the theoretical UTS equation is that of an A and B. These ratios and their determination are explained under subsection 7.1.2.2.

7.1.2.2 Ratio A

From Figure 5-9 it is clear that the 0° UTS is much stronger than the 90° UTS and that it decreases in an exponential manner because of the fibre directions. This means that a purely analytical and trigonometric approach will be symmetric and will not do justice to the final UTS value of the specimen. This means that an external element needs to be implemented within the equation and it is done in the form of A and B, with A + B = 1.

The value of A can be obtained from a graph where all the unidirectional layout combinations' UTS values are divided by the strongest UTS value within that layout combination category – which is $[0]_R$ (see Figure 7-2). The values range from 1 to about 0.02 from left to right. Each layout combination within each layout category has its own value for A and all these values can be obtained on this graph. Under the subheading 7.1.2.2.1 the method for calculating the exact location of each ratio A value is shown.

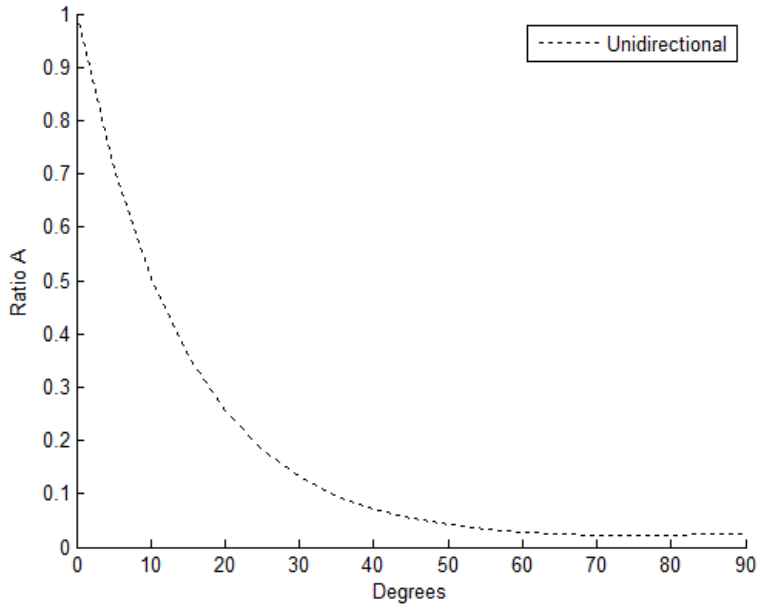

Figure 7-2: $UTS_{unidirectional}/UTS_{0°}$ Graph

7.1.2.2.1 x-coordinates and the ratio degree

All ratio A values of the 90°, 45°, and 30° layout combination categories were obtained by an optimisation process based on the actual curved fitted experimental results. These values were plotted on the same graph as Figure 7-2 with the flowing figure as the result:

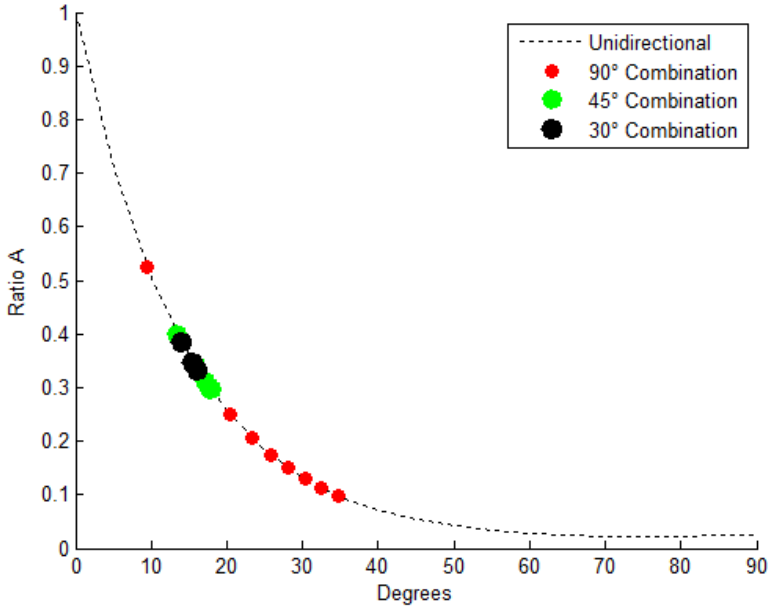

Figure 7-3: Ratio A vs mean degree of four layout combinations

From this graph it is clear that there exists a tendency between the ratio A values and the layout combination categories. The range in which the values are positioned decreases as the layout combination category decreases. The ratio A value converges towards a value of 0.35. To prove this correlation, a process of finding the exact x-coordinates of the different layout combination categories on the above figure was implemented. To find these x-coordinates in the graph from Figure 7-3, Equation 7-6 are expanded and used:

$$x_{coordinate} = Mean\ Degree - Ratio\ Degre$$
$$= \left(\frac{Layout\ Combination\ Category}{2} - First\ Layer\ Degree\right) - Ratio\ Degree$$

where the 'first layer degree' represents the first layer of a particular layout combination within any layout category. This is better explained by the hands of Table 7-2. The ratio degree is a set value that is obtained through the built-in goal seek function in Excel with all other columns remaining fixed.

Table 7-2: All values necessary for ratio A value (experimental data)

Layout Combination Category	First Layer Degree	Mean Degree	Ratio Degree	$x_{coordinate}$	Ratio A
90	0	45	35.55	9.16	0.53458372
90	5	40	26.62	13.51	0.39790096
90	10	35	17.87	17.47	0.30429289
90	15	30	9.56	20.92	0.24126423
90	20	25	1.72	23.89	0.19797359
90	25	20	-5.75	26.49	0.16673260
90	30	15	-13.04	28.88	0.14259475
90	35	10	-20.29	31.19	0.12273581
90	40	5	-27.54	33.50	0.10595964
90	45	0	-34.65	35.71	0.09226033
45	0	22.5	9.04	13.07	0.40989189
45	5	17.5	1.74	16.03	0.33543389
45	10	12.5	-4.67	17.43	0.30511523
45	15	7.5	-10.33	17.94	0.29484515
45	20	2.5	-15.40	17.90	0.29570378
45	25	-2.5	-20.01	17.27	0.30846570
30	0	15	0.98	14.12	0.38161543
30	5	10	-5.51	15.65	0.34405441
30	10	5	-11.16	16.16	0.33245671
30	15	0	-16.16	16.13	0.33311396

The graph of the ratio degree values vs the $x_{oordinate}$ values was constructed and can be seen in the Figure 7-4 below:

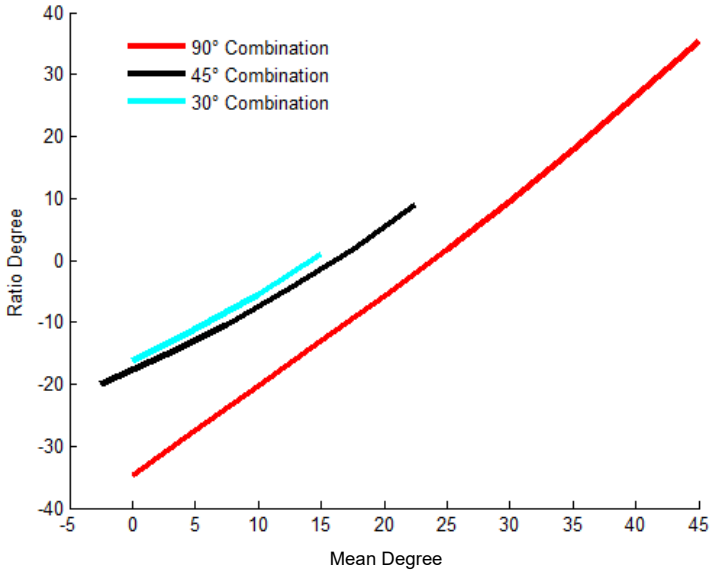

Figure 7-4: Ratio degree vs $x_{coordinate}$ of ratio A vs mean degree graph

To verify whether this mathematical model approach could work, the ratio degrees (and eventually the ratio A values) of the 75°, 60° (interpolation), and 15° (extrapolation) values within the above figure were found based on a similarity optimisation process between the ratio A values and the theoretical UTS values. Figure 7-5 was then constructed with the dotted lines representing the interpolation and extrapolation values based on the other set values. These values were used to construct a 3D graph in MATLAB® (using the built-in curve fitting tool function) to find all other ratio degree values for the completion purpose of the mathematical model.

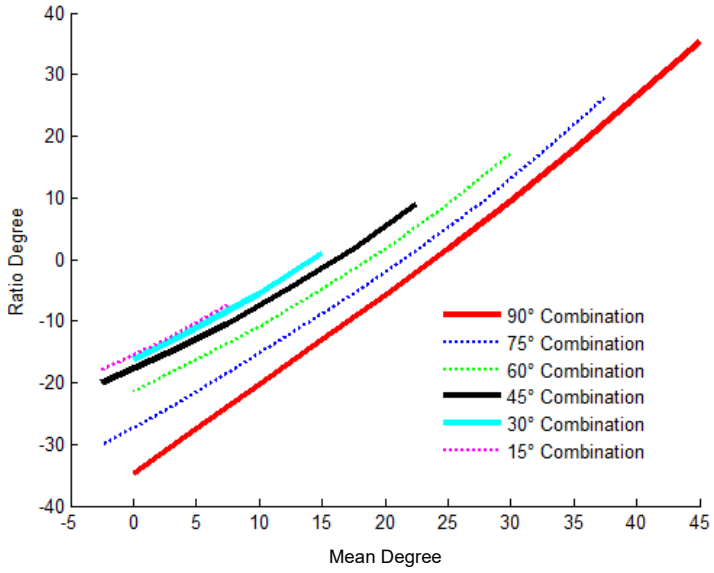

Figure 7-5: Ratio degree vs $x_{coordinate}$ of ratio A graph (inter and extrapolation)

The 3D graph was constructed by using the built-in curve fitting tool of MATLAB® with the layout category, the mean degree, and the ratio degree on the x-, y- and z-axis respectively. A polynomial of degrees 4 (x) and 5 (y) was selected, and the final graph with the equation are displayed in Figure 7-6 below. The selected point shows that within a layer combination category of 75° and a mean degree of about 15° the ratio degree will be -8.64.

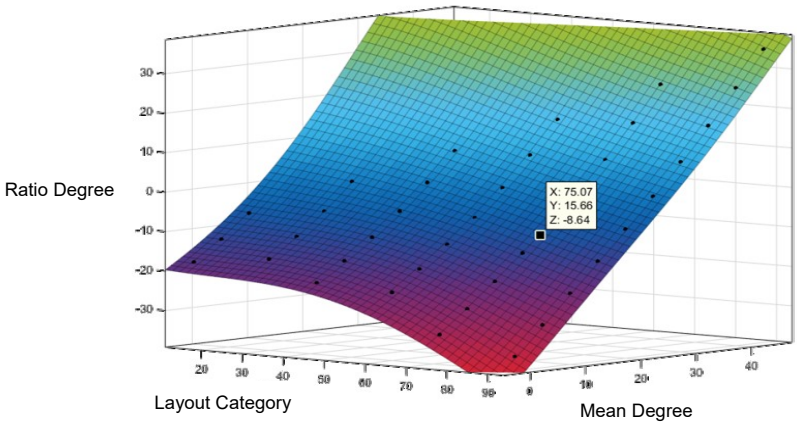

Figure 7-6: 3D constructed graph – layer combination vs $x_{coorditnates}$ vs ratio degree

$$f(x,y) = p00 + p10x + p01y + p20x^2 + p11xy + p02y^2 + p30x^3 + p21x^2y + p12xy^2 + p03y^3 + p40x^4 + p31x^{3y} + p22x^2y^2 + p13xy^3 + p04y^4 + p41x^4y + p32x^3y^2 + p23x^2y^3 + p14xy^4 + p05y^5$$ Equation 7-7

with:

Table 7-3: 3D graph's polynomial equation values

Variable	Optimised Value	MATLAB® values with the R-square value of 1
p00	-13.98472926	-13.44 (-15.22, -11.67)
p01	0.922477747	0.9373 (0.7547, 1.12)
p02	0.015204173	0.01524 (-0.005239, 0.03573)
p03	0.000313508	0.0003139 (-0.0008433, 0.001471)
p04	9.238422E-07	9.139e-07 (-2.718e-05, 2.901e-05)
p05	-2.19E-07	-2.193e-07 (-4.682e-07, 2.963e-08)
p10	-0.200480484901	-0.2226 (-0.4118, -0.03345)
p11	0.01075	0.01075 (-0.01067, 0.03218)
p12	-0.0002295	-0.0002295 (-0.001569, 0.00111)
p13	-3.31E-06	-3.307e-06 (-4.74e-05, 4.079e-05)
p14	2.50E-07	2.496e-07 (-2.56e-07, 7.553e-07)
p20	0.008671912	0.00872 (0.002279, 0.01516)
p21	-0.000576502	-0.0005765 (-0.00136, 0.0002066)
p22	2.07E-06	2.065e-06 (-2.791e-05, 3.204e-05)
p23	-9.49E-08	-9.487e-08 (-5.543e-07, 3.646e-07)
p30	-0.0001704	-0.0001704 (-0.0002577, -8.315e-05)
p31	9.27E-06	9.271e-06 (-2.1e-06, 2.064e-05)
p32	-1.32E-09	-1.318e-09 (-2.147e-07, 2.121e-07)
p40	7.83E-07	7.836e-07 (3.743e-07, 1.193e-06)
p41	-3.95E-08	-3.959e-08 (-9.728e-08, 1.811e-08)

These ratio degree values were used to calculate the final x-coordinates for all the ratio A values, which can be seen in Figure 7-3 and the final graph in Figure 7-7 below:

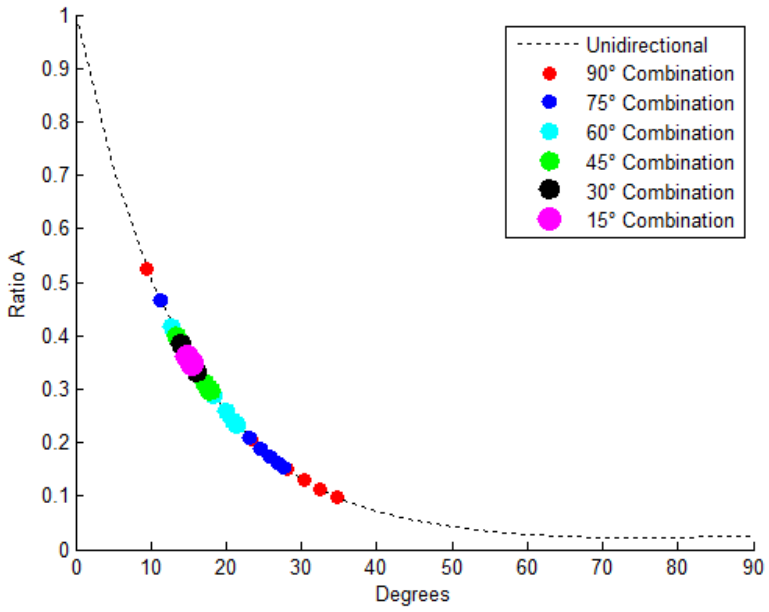

Figure 7-7: Ratio A vs degree ($UTS_{unidirectional}/UTS_{0°}$) – seven layout combinations

Note the assumption that the range in which the value is positioned decreases as the layout combination category decreases and the ratio A value converges to a value of 0.35, which can easily be made from Figure 7-7 above. All final values of the layer combination, first layer degree, mean degree, ratio degree, x-coordinates, and ratio A are summarised in Table 7-4 below:

Table 7-4: All values necessary for Ratio A values (verification data)

Layout combination category	First layer degree	Mean degree	Ratio degree	$X_{coordinate}$	Ratio A
90	0	45	35.55	9.16	0.53458372
90	5	40	26.62	13.51	0.39790096
90	10	35	17.87	17.47	0.30429289
90	15	30	9.56	20.92	0.24126423
90	20	25	1.72	23.89	0.19797359
90	25	20	-5.75	26.49	0.16673260
90	30	15	-13.04	28.88	0.14259475
90	35	10	-20.29	31.19	0.12273581
90	40	5	-27.54	33.50	0.10595964
90	45	0	-34.65	35.71	0.09226033
75	0	37.5	26.29	10.80	0.47821812
75	5	32.5	17.39	15.60	0.34526058
75	10	27.5	9.09	19.10	0.27265032
75	15	22.5	1.48	21.65	0.22978528
75	20	17.5	-5.54	23.61	0.20174971
75	25	12.5	-12.11	25.25	0.18094101
75	30	7.5	-18.39	26.75	0.16388743
75	35	2.5	-24.45	28.10	0.14999468

Layout combination category	First layer degree	Mean degree	Ratio degree	$X_{coordinate}$	Ratio A
75	40	-2.5	-30.17	29.05	0.14095629
60	0	30	17.19	11.97	0.44166175
60	5	25	9.01	16.22	0.33122886
60	10	20	1.66	18.79	0.27844656
60	15	15	-4.91	20.31	0.25143478
60	20	10	-10.86	21.23	0.23638966
60	25	5	-16.35	21.79	0.22768090
60	30	0	-21.46	21.95	0.22522809
45	0	22.5	9.04	13.07	0.40989189
45	5	17.5	1.74	16.03	0.33543389
45	10	12.5	-4.67	17.43	0.30511523
45	15	7.5	-10.33	17.94	0.29484515
45	20	2.5	-15.40	17.90	0.29570378
45	25	-2.5	-20.01	17.27	0.30846570
30	0	15	0.98	14.12	0.38161543
30	5	10	-5.51	15.65	0.34405441
30	10	5	-11.16	16.16	0.33245671
30	15	0	-16.16	16.13	0.33311396
15	0	7.5	-7.40	14.69	0.36734801
15	5	2.5	-13.04	15.53	0.34687704
15	10	-2.5	-17.96	16.24	0.33063436

7.2 Summary of the verification of model results

With a possible mathematical approach towards the prediction of the UTS values of CFF material, it is important to verify the model's values against the experimental values. All four layout combination categories (unidirectional, 90°, 45°, and 30°) together with the extra three (75°, 60°, and 15°) UTS values were compared with the model's values and can be seen in the tables in Appendix B. In those tables the α and β angles, the ratio A and B, the theoretical values, the true values, the cftool values of MATLAB® (only for the unidirectional) and the experimental values (for every other layout combination category), and finally the percentage error are shown. The following table shows the average percentage error of the proposed mathematical model's results against the experimental results:

Table 7-5: Summary of mathematical model verification values

Layout combination	Average % error
Unidirectional	7.68
90	6.35
75	10.10
60	11.14
45	8.21
30	0.60
15	21.75
Average	9.41

The overall percentage error average of the proposed mathematical model approach can be seen in the above table to be 9.41%. This is lower than both linear and non-linear approaches with LAP which had values of 28.33% and 36.09% respectively. However, the average of the light purple shaded rows (the chosen layout combination categories for verification purposes) is 14.33%, which is still lower than the LAP results. These results show that the mathematical model is, in fact, plausible and may be used for future references.

Chapter 7 discussed the possible mathematical model that can be used for the prediction of the UTS values of any given layout combination within the CFF material printed with the Markforged Mark Two printer. The verification of this model showed promising results. Chapter 8 concludes this dissertation along with recommendations for future work.

CHAPTER 8

CONCLUSION AND RECOMMENDATIONS

The foundational reason behind this study was to obtain material properties for CFF technology prominently used by Markforged in their Mark Two printer, as such data does not exist. In addition, was another aspect which involved investigating whether this technology could be simulated according to existing analysis programs, and if not, a characterisation process would need to be followed and constructed.

After characterising the anisotropic mechanical properties of carbon fibre-reinforced thermoplastic composites analysing its comparison with classical laminate theory (by using LAP), it is clear that it complies only to the unidirectional layout combination, and that it does not comply statistically sufficiently with the other layout combinations which include the 90°, 45°, and 30° layout combinations.

Everything considered, the results obtained from LAP show that CFF material tends more toward being linear than non-linear, especially when the angles between a layer and its successive layer decreases. This is true when one considers the fact that the CFF material behaves both linearly and non-linearly within the single combination category, after which it tends more to be linear.

The verification process of this dissertation shows that the lack of material property data of the CFF material (validation of the dissertation) is, in fact, a problem that could not just be solved by assuming that the material complies with CLT. Therefore, a possible mathematical model needs to be implemented to predict the ultimate tensile strengths of CFF material. The analytical approach towards predicting the ultimate tensile strength of the CFF material showed promising results as the values are closer to the actual experimental values than the CLT through LAP. Future investigation can be done to optimise such a mathematical model approach – especially in the line of the ratio degree section of the proposed model.

REFERENCES

[1] G. A. Potgieter, “Modification of Polymer Testing Station and Evaluation of FDM Materials for use on BAJA car and AHRLAC,” no. 1, 2016.

[2] Joseph Arthur, *Purpose of Tensile Test.* [Online] Available: https://bizfluent.com/info-12146439-purpose-tensile-test.html. Accessed on: Jan. 15 2017.

[3] J. R. Davis, *Tensile testing,* 2nd ed. Materials Park, Ohio: ASM International, 2004.

[4] D. van Huynh, S. K. Jain, and S. R. López-Permouth, Eds., *Algebra and its applications: Tension Test*. Providence, R.I.: American Mathematical Society, 2006.

[5] *Tensile Testing - Instron.* [Online] Available: http://www.instron.us/en-us/our-company/library/test-types/tensile-test. Accessed on: 16-Jan-17.

[6] *Tensile Test.* [Online] Available: https://www.testresources.net/applications/test-types/tensile-test/. Accessed on: 16-Jan-17.

[7] *Tensile Testing - Theory, Applications and Systems.* [Online] Available: https://www.azom.com/article.aspx?ArticleID=5551. Accessed on: 09-Aug-18.

[8] *Tensile Testing.* [Online] Available: http://me.aut.ac.ir/staff/solidmechanics/alizadeh/Tensile%20Testing.htm. Accessed on: 09-Aug-18.

[9] Solid Concepts, *Fused Deposition Modeling (FDM) Technology: Watch the latest FDM video from Stratasys Direct Manufacturing*, 2013.

[10] Dr. Anine Jordaan, *SEM*. Senior Subject Specialist Laboratory for Electron Microscopy CRB North West University Potchefstroom Campus, 2017.

[11] Al Dean, “Markforged Mark Two,” 2016.

[12] A.S. Jonker, *Laminate Analysis of Composite Materials*. Potchefstroom North West, 2003.

[13] H. L. Tekinalp *et al.,* “Highly oriented carbon fiber–polymer composites via additive manufacturing,” *Composites Science and Technology*, vol. 105, pp. 1–7, 2014.

[14] Michael Montero, Shad Roundy, Dan Odell, Sung-Hoon Ahn, and Paul K. Wright, “Material Characterization of Fused Deposition Modeling (FDM) ABS by Designed Experiments,” p. 1.

[15] J.-P. Kruth, M. C. Leu, and T. Nakagawa, “Progress in Additive Manufacturing and Rapid Prototyping,” *CIRP Annals*, vol. 47, no. 2, pp. 525–540, 1998.

[16] Q. Sun, G. M. Rizvi, C. T. Bellehumeur, and P. Gu, “Effect of processing conditions on the bonding quality of FDM polymer filaments,” *Rapid Prototyping Journal*, vol. 14, no. 2, pp. 72–80, 2008.

[17] S. Guessasma, S. Belhabib, and H. Nouri, “Significance of pore percolation to drive anisotropic effects of 3D printed polymers revealed with X-ray μ-tomography and finite element computation,” *Polymer*, vol. 81, pp. 29–36, 2015.

[18] A. Bagsik, “Mechanical properties of fused deposition modeling parts manufactured with Ultem*9085,”

[19] L. Li, Q. Sun, C. Bellehumeur, and P. Gu, “Composite Modeling and Analysis for Fabrication of FDM Prototypes with Locally Controlled Properties,” *Journal of Manufacturing Processes*, vol. 4, no. 2, pp. 129–141, 2002.

[20] Robert Sayre III, “A Comparative Finite Element Stress Analysis of Isotropic and Fusion Deposited 3D Printed Polymer,” 2014.
[21] A. R. Torrado *et al.,* “Characterizing the effect of additives to ABS on the mechanical property anisotropy of specimens fabricated by material extrusion 3D printing,” *Additive Manufacturing*, vol. 6, pp. 16–29, 2015.
[22] P. Gu and L. Li, “Fabrication of Biomedical Prototypes with Locally Controlled Properties Using FDM,” *CIRP Annals*, vol. 51, no. 1, pp. 181–184, 2002.
[23] Bin Huang, Ed., *Alternate Slicing and Deposition Strategies for Fused Deposition Modelling*. Hoboken, NJ, USA: John Wiley & Sons, Inc, 2005.
[24] J. T. Belter and A. M. Dollar, “Strengthening of 3D printed fused deposition manufactured parts using the fill compositing technique,” (eng), *PloS one*, vol. 10, no. 4, e0122915, 2015.
[25] Vedansh Chaturvedi, “Parametric Optimization of Fused Deposition Modeling using Response Surface Methodology: A thesis submitted in partial fulfillment for the requirement for the degree of Master of Technology in Production Engineering,” vol. 8, 2009.
[26] R. J. Zaldivar *et al.,* “Influence of processing and orientation print effects on the mechanical and thermal behavior of 3D-Printed ULTEM® 9085 Material,” *Additive Manufacturing*, vol. 13, pp. 71–80, 2017.
[27] W. C. Smith and R. W. Dean, “Structural characteristics of fused deposition modeling polycarbonate material,” *Polymer Testing*, vol. 32, no. 8, pp. 1306–1312, 2013.
[28] S. Ahn, M. Montero, D. Odell, S. Roundy, and P. K. Wright, “Anisotropic material properties of fused deposition modeling ABS,” *Rapid Prototyping Journal*, vol. 8, no. 4, pp. 248–257, 2002.
[29] R. Matsuzaki *et al.,* “Three-dimensional printing of continuous-fiber composites by in-nozzle impregnation,” (eng), *Scientific reports*, vol. 6, p. 23058, 2016.
[30] F. Ning, W. Cong, J. Qiu, J. Wei, and S. Wang, “Additive manufacturing of carbon fiber reinforced thermoplastic composites using fused deposition modeling,” *Composites Part B: Engineering*, vol. 80, pp. 369–378, 2015.
[31] K.-i. Mori, T. Maeno, and Y. Nakagawa, “Dieless Forming of Carbon Fibre Reinforced Plastic Parts Using 3D Printer,” *Procedia Engineering*, vol. 81, pp. 1595–1600, 2014.
[32] M. Chapiro, “Current achievements and future outlook for composites in 3D printing,” *Reinforced Plastics*, vol. 60, no. 6, pp. 372–375, 2016.
[33] G. W. Melenka, B. K. Cheung, J. S. Schofield, M. R. Dawson, and J. P. Carey, “Evaluation and prediction of the tensile properties of continuous fiber-reinforced 3D printed structures,” *Composite Structures*, vol. 153, pp. 866–875, 2016.
[34] Rodriguez JF, Thomas JP, Renaud JE, “Characterization of the mesostructure of fused-deposition acrylonitrile- butadine- styrene materials.,” vol. J 2000, no. 6:175-86.
[35] X. Yao, C. Luan, D. Zhang, L. Lan, and J. Fu, “Evaluation of carbon fiber-embedded 3D printed structures for strengthening and structural-health monitoring,” *Materials & Design*, vol. 114, pp. 424–432, 2017.
[36] X. Tian, T. Liu, C. Yang, Q. Wang, and D. Li, “Interface and performance of 3D printed continuous carbon fiber reinforced PLA composites,” *Composites Part A: Applied Science and Manufacturing*, vol. 88, pp. 198–205, 2016.

[37] N. Li, Y. Li, and S. Liu, “Rapid prototyping of continuous carbon fiber reinforced polylactic acid composites by 3D printing,” *Journal of Materials Processing Technology*, vol. 238, pp. 218–225, 2016.
[38] M. Chapiro, “Current achievements and future outlook for composites in 3D printing,” *Reinforced Plastics*, vol. 60, no. 6, pp. 372–375, 2016.
[39] X. Tian, T. Liu, C. Yang, Q. Wang, and D. Li, “Interface and performance of 3D printed continuous carbon fiber reinforced PLA composites,” *Composites Part A: Applied Science and Manufacturing*, vol. 88, pp. 198–205, 2016.
[40] M. Eiasswad, S. Alfayad, K. Khalil, F. B. Ouezdou, “Development of a new deformable flexible active foot for hydroïd robot using 3d printing of composite,”
[41] Stewart Bland, “MarkForged develops 3D printer for carbon fibre,” *Reinforced Plastics*, vol. 59, no. 1, p. 12, 2015.
[42] X. Tian *et al.,* “Recycling and remanufacturing of 3D printed continuous carbon fiber reinforced PLA composites,” *Journal of Cleaner Production*, vol. 142, pp. 1609–1618, 2017.
[43] F. Ning, W. Cong, J. Qiu, J. Wei, and S. Wang, “Additive manufacturing of carbon fiber reinforced thermoplastic composites using fused deposition modeling,” *Composites Part B: Engineering*, vol. 80, pp. 369–378, 2015.
[44] Y. Zhang, W. de Backer, R. Harik, and A. Bernard, “Build Orientation Determination for Multi-material Deposition Additive Manufacturing with Continuous Fibers,” *Procedia CIRP*, vol. 50, pp. 414–419, 2016.
[45] G. W. Melenka, B. K. Cheung, J. S. Schofield, M. R. Dawson, and J. P. Carey, “Evaluation and prediction of the tensile properties of continuous fiber-reinforced 3D printed structures,” *Composite Structures*, vol. 153, pp. 866–875, 2016.
[46] Jones Rm, *Mechanics of composite materials*: Washington: Scripta Book Co, 1975.
[47] ASTM International, “D 3039/D 3039M – 00: Standard Test Method for Tensile Properties of Polymer Matrix Composite Materials,” 2004.
[48] Anaglyph Ltd, “LAP User Manual Rev5,” 2010.

APPENDIX A – ALL EXPERIMENTAL RESULTS

Appendix A shows all experimental results in detail with discussions and explanations where necessary. These results include stress-vs-strain graphs, final breakage display, SEM pictures of breakage, and tables of material properties (modulus of elasticity, yield strength, ultimate tensile strength, and strain).

A.1 Unidirectional

As discussed in subsection 4.2.1, all 19 possible combinations within this category (interval of 5°) were subjected to a tensile test at least 3 times per combination set. The raw data (load and extension in mm) were gathered and processed using Microsoft Excel and MATLAB®. The stress-vs-strain graphs of each set are displayed, followed by possible explanations and findings. This is also the conduct for all the experimental results.

A.1.1 $[0]_R$

The first orientation combination discussed is the one where all eight layers consist of carbon fibre strands that are orientated at 0°. The stress-vs-strain graph is shown first with further insights to follow.

A.1.1.1 Stress vs strain graph for $[0]_R$

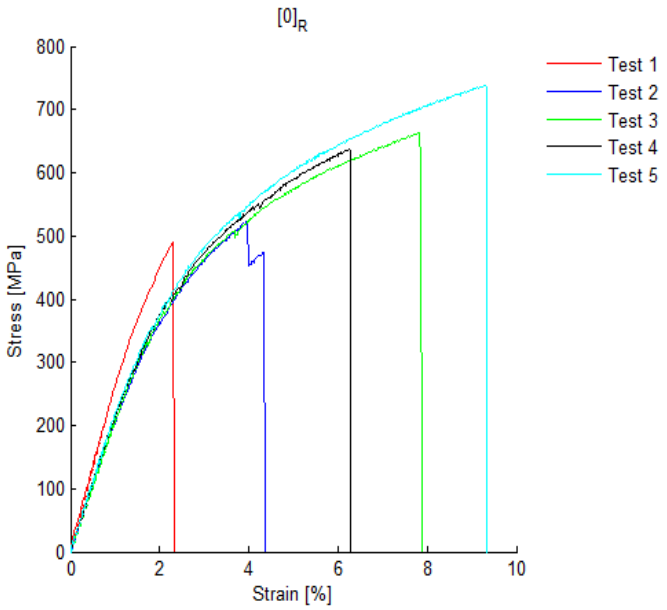

Figure A-1: Stress vs strain graph for $[0]_R$ layout combination

From Figure A-1 it is clear that four of the five tests have the same modulus of elasticity for up to 4 % strain. Test 1 was not executed on the same date as the rest and also not according to the speed of the ASTM standard (it was set to 2 mm/s and not 2 mm/min) and was therefore not used for further data processing. Furthermore, it is clear that the specimens had a linear tendency up until a strain value of about 1.8 % where after they tended to behave as a non-linear material.

Also observable is that this orientation combination of strands caused the specimen to break brittlely and is not ductile, since there is no non-uniform plastic deformation region. Test 2 seems to have broken in segments, which happens when only some of the strands break simultaneously while the rest break just after that. Figure A-2 shows test 5's final breakage. Please note that the specimen did not break into two pieces and was done manually afterwards for inspection purposes and will not be done with all the specimens. The MTS Landmark® and constructed graph shows a complete failure, however, it is only the carbon fibre strands that failed and not the surrounding nylon. This is evident throughout all the results.

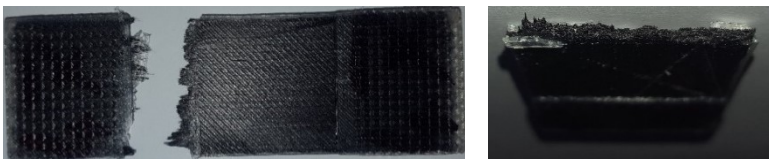

Figure A-2: Breakage of $[0]_R$ – Test 5

From the above figure, it is clear that the specimen did not break in the middle, making it appear as though dimensions and/or procedures were not followed correctly. However, other orientation combination category specimens did break within the desired location (see Section A.3.2) and therefore it would be difficult to have one specimen that will break in the middle regardless of the internal structures. Consequently, breakage depends on the internal structure.

It is important to note that the strength of the CFF material lies within the individual continuous fibre strands (see Figure 2-2) and not the resin between these individual strands or the adhesion (nylon) between adjacent combined strands. From this it is assumed that the $[0]_R$ combination will have the highest UTS, as the strands themselves need to break for a complete breakage of the specimen. This phenomenon can be better explained by examining SEM pictures of the breakage. Only certain specimens ($[0]_R$, $[35]_R$, $[90]_R$, and $[0/45]_R$) were selected to be viewed under a SEM microscope.

A.1.1.2 SEM Pictures of $[0]_R$ breakage

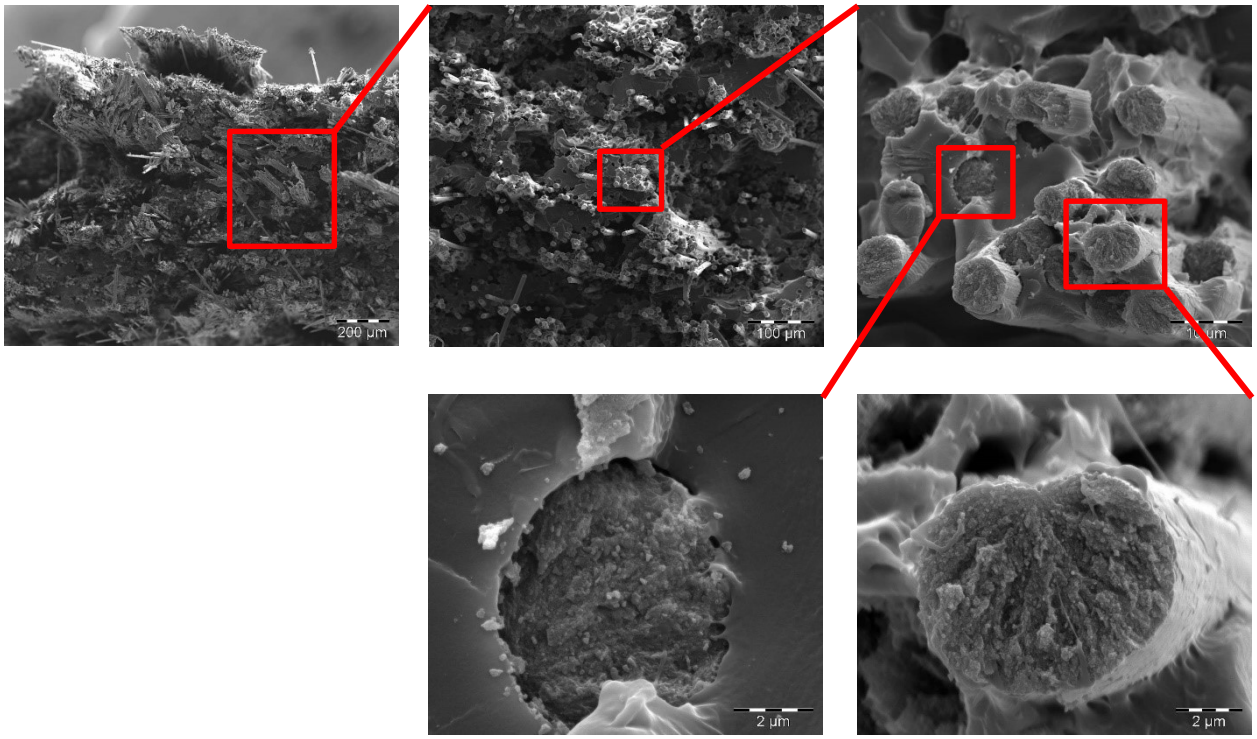

Figure A-3: SEM pictures of $[0]_R$ Breakage [10]

From the SEM pictures in Figure A-3 above it is evident that the individual strands had a complete brittle breakage with little to no shear. The material properties of the resin between these strands are not known and therefore a possible mathematical module will be helpful in predicting the results (see Chapter 7 for further details). The bottom right picture reveals that the strand sheared to one point, however, the picture on the bottom left shows that it was a brittle break. A possible cause for this occurrence might the that all the individual strands might not have been perfectly parallel.

A.1.1.3 Material properties of $[0]_R$

All necessary material properties of the $[0]_R$ combination are given as a maximum, average, and minimum, which are tabulated:

Table A-1: Material properties of $[0]_R$

Material parameter	Value		Unit
Modulus of elasticity ($E_{[0]R}$)	Max	21.94	[GPa]
	Mean	21.36	[GPa]
	Min	20.57	[GPa]
Yield strength ($YS_{[0]R}$)	Max	212.75	[MPa]
	Mean	193.49	[MPa]
	Min	169.02	[MPa]

Material parameter	Value		Unit
Ultimate Tensile Strength ($UTS_{[0]R}$)	Max	737.34	[MPa]
	Mean	639.90	[MPa]
	Min	489.82	[MPa]
Strain ($\varepsilon_{[0]R}$)	Max	9.32	[%]
	Mean	6.96	[%]
	Min	4.36	[%]

A.1.2 $[5]_R$

Each layer consists of carbon strands that are 5° with respect to the specimen's side length. It is expected (as discussed in section A.1.1) that the specimen will fail within the resin and not the carbon strands themselves. From this it is also predictable that the maximum UTS will be much lower than the $[0]_R$ combination.

A.1.2.1 Stress-vs-strain graph of $[5]_R$

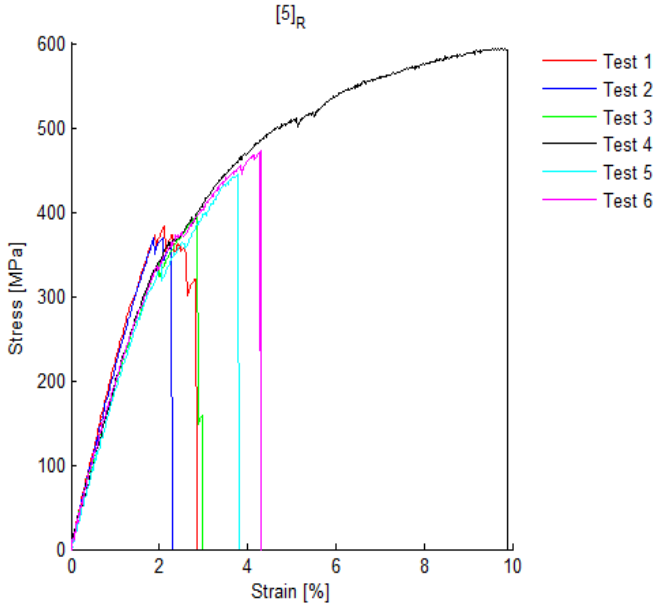

Figure A-4: Stress vs Strain Graph of $[5]_R$ layout combination

Again, in Figure A-4, just as in Figure A-1, there is an outlier – this time it is test 4 and it was also not used for further data processing. A possible explanation could that the specimen was not correctly inserted vertically, which would cause the tensile force to act along the strands just as in the case of a $[0]_R$ combination. Another explanation could be that the strands within the specimen had rearranged themselves due to the loading and henceforth became straight and thus also stronger. Both explanations can clearly be seen in the final appearance of the specimen (see Figure A-5). Also apparent is that all tests broke as a brittle material and the elastic moduli

of all are almost the same. Tests 1 and 2 have a similar breakage as test 2 in the $[0]_R$ category. It shows that the strands broke into segments and not all at once.

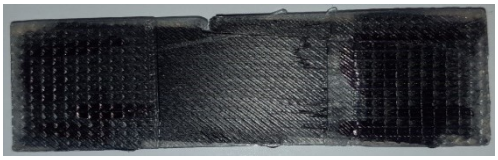

Figure A-5: Breakage of $[5]_R$ – test 4

It is clear that the specimen broke in the same manner as the $[0]_R$ combination for almost the entire width. When this occurrence is compared with the rest of the specimens one can conclude that test 4 is not valid. Figure A-6 shows test 2's final appearance, and all other specimens broke in the same manner.

Figure A-6: Breakage of $[5]_R$ – test 2

It is evident that the specimen did not break into two pieces but only sheared off between the combined strands, proving the statement made in Section A.1.1. From here on this incident can be seen with all unidirectional layouts.

A.1.2.2 Material properties of $[5]_R$

Again all necessary material properties of the $[5]_R$ combination can be seen in Table A-2:

Table A-2: Material Properties of $[5]_R$

Material parameter	Value		Unit
Modulus of elasticity ($E_{[5]R}$)	Max	22.67	[GPa]
	Mean	20.91	[GPa]
	Min	19.30	[GPa]
Yield strength ($YS_{[5]R}$)	Max	158.87	[MPa]
	Mean	125.59	[MPa]
	Min	99.77	[MPa]
Ultimate tensile strength ($UTS_{[5]R}$)	Max	472.72	[MPa]
	Mean	413.44	[MPa]
	Min	369.55	[MPa]
Strain ($\varepsilon_{[5]R}$)	Max	4.32	[%]
	Mean	3.25	[%]
	Min	2.30	[%]

A.1.3 $[10]_R$

The $[10]_R$ combination is 5° more than the previously discussed orientation and it was again expected that the UTS would be lower.

A.1.3.1 Stress-vs-Strain Graph of $[10]_R$

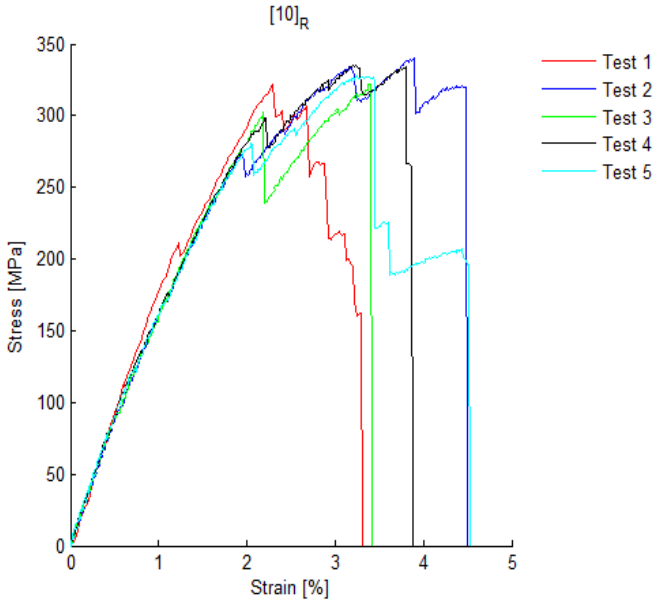

Figure A-7: Stress vs Strain Graph of $[10]_R$ layout combination

From Figure A-7 above it is clear that this combination's test results are consistent and almost precise, as is evident also from the boxplots (see Figure 5-1, Figure 5-5, and Figure 5-9). In all five tests the specimens seemed to break into segments and are partially brittle as the strands sheared from one another. This can easily be explained when considering the layout of the carbon strands – there is more room for inter-strand shearing. By comparing the previous three stress-vs-strain graphs a great decrease in the UTS can be seen – this is suspected and well observed throughout this category of orientation. The following figure shows test 1's final appearance (the same shear-between-strands occurrence can be seen):

Figure A-8: Breakage of $[10]_R$ – Test 1

A.1.3.2 Material properties of $[10]_R$

Table A-3: Material Properties of $[10]_R$

Material parameter	Value		Unit
Modulus of elasticity ($E_{[10]R}$)	Max	18.06	[GPa]
	Mean	17.72	[GPa]
	Min	17.05	[GPa]
Yield strength ($YS_{[10]R}$)	Max	92.17	[MPa]
	Mean	84.67	[MPa]
	Min	77.76	[MPa]
Ultimate tensile strength ($UTS_{[10]R}$)	Max	340.37	[MPa]
	Mean	331.14	[MPa]
	Min	321.56	[MPa]
Strain ($\varepsilon_{[10]R}$)	Max	4.53	[%]
	Mean	3.93	[%]
	Min	3.31	[%]

From Table A-3 it is clear that the $[10]_R$ combination's data are close to one another as is also evident from Figure A-7.

A.1.4 $[15]_R$

This orientation served for interesting results as seen under the next two headings. The most explicable reason is the influence of the nylon on the test results. Where the nylon did not have such an influence on the previous three orientations, from here on its influence is apparent.

A.1.4.1 Stress-vs-strain graph of $[15]_R$

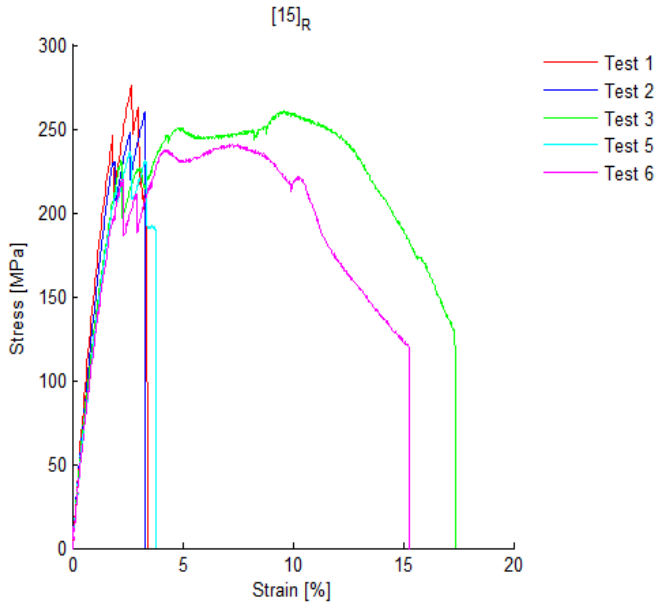

Figure A-9: Stress vs strain graph of $[15]_R$ layout combination

Figure A-9 shows that tests 3 and 6 had a much higher strain value than the other three tests. This can be attributed to the fact that the external adhesion between the strands (nylon) kept the strands intact (nylon has a much larger strain capacity as carbon fibre), or that the breakage between the strands did not break as suddenly as the other three tests, resulting in the MTS Landmark® not presenting it as a total failure (see explanation under section A.1.1). This occurrence is also evident from Figure A-13 under subsection A.1.6.1.

Furthermore, notice the three spikes around 2-3% strain. This shows that the specimen broke in segments: one strand broke first, then another one, followed by another until the specimen overall could not withstand the increasing tensile force. This occurrence can be seen when examining Figure A-10. The same singularity can be seen in almost all the other unidirectional orientations with different degrees of magnitudes.

Figure A-10: Breakage of $[15]_R$ – Test 2

A.1.4.2 Material properties of $[15]_R$

Table A-4: Material properties of $[15]_R$

Material Parameter	Value		Unit
Modulus of elasticity ($E_{[15]R}$)	Max	16.35	[GPa]
	Mean	14.61	[GPa]
	Min	13.15	[GPa]
Yield strength ($YS_{[15]R}$)	Max	94.20	[MPa]
	Mean	74.97	[MPa]
	Min	56.99	[MPa]
Ultimate tensile strength ($UTS_{[15]R}$)	Max	275.80	[MPa]
	Mean	254.92	[MPa]
	Min	236.59	[MPa]
Strain ($\varepsilon_{[15]R}$)	Max	17.35	[%]
	Mean	8.64	[%]
	Min	3.31	[%]

A.1.5 $[20]_R$

From the 20° orientation the dependability on the strands orientation is magnificent and can clearly be seen when examining all the stress-vs-strain graphs all at once.

A.1.5.1 Stress-vs-strain graph of $[20]_R$

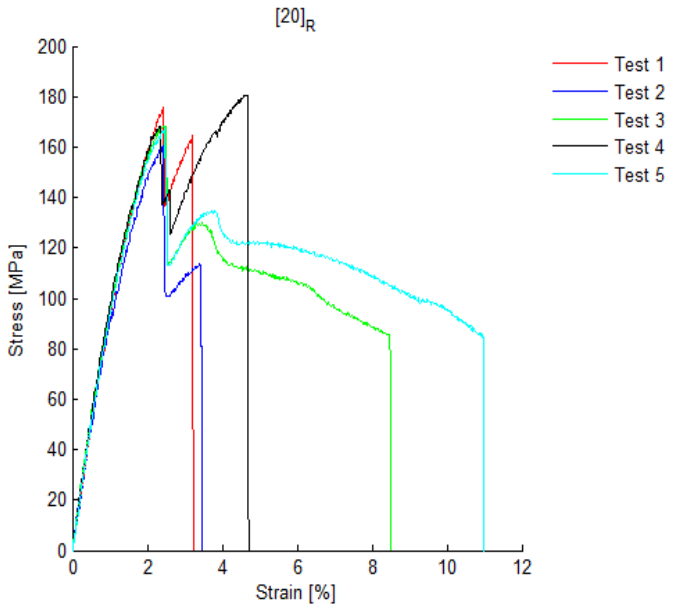

Figure A-11: Stress vs Strain Graph of $[20]_R$ layout combination

Just like the case with the results of the $[15]_R$ combination, it is clear that there are spikes between 2% and 5% strain in the above graph. It shows that once one or two strands have sheared from one another, the whole specimen basically fails, resulting from there not being any other strands within a reasonable orientation to support the overall strength of the specimen (like the previous four orientations). Furthermore, it is also clear that tests 3 and 5 also underwent higher strain rates than the other tests. The explanation is the same as the $[15]_R$ combination's. Figure A-12 presents test 5's final appearances.

Figure A-12: Breakage of $[20]_R$ – Test 5

From the above figure it is clear that after the strands had already sheared from one another (the MTS Landmark® did not recognise it as a sudden failure), the nylon within the specimen still kept the specimen intact.

A.1.5.2 Material properties of $[20]_R$

Table A-5: Material Properties of $[20]_R$

Material parameter	Value		Unit
Modulus of elasticity ($E_{[20]R}$)	Max	10.79	[GPa]
	Mean	10.32	[GPa]
	Min	10.00	[GPa]
Yield strength ($YS_{[20]R}$)	Max	52.01	[MPa]
	Mean	48.87	[MPa]
	Min	45.04	[MPa]
Ultimate tensile strength ($UTS_{[20]R}$)	Max	180.83	[MPa]
	Mean	170.60	[MPa]
	Min	160.27	[MPa]
Strain ($\varepsilon_{[20]R}$)	Max	11.00	[%]
	Mean	6.18	[%]
	Min	3.24	[%]

Table A-5 shows that the results from the $[20]_R$ combination is consistent with little variation.

A.1.6 $[25]_R$ – $[90]_R$

The discussions of all the unidirectional orientation results follow a similar pattern and all possible applicable occurrences have already been addressed. From here on only the stress-vs-strain and the material properties are shown for all the remaining specimens within the unidirectional orientation group. Note how the UTS, E, and YS decreases while the strain increases as the angle increases. This is ascribed to the fact that the nylon begins to play a much bigger role as the strength of the specimen becomes less and less dependent on the carbon fibre strands.

A.1.6.1 Stress-vs-Strain of $[25]_R$ – $[90]_R$

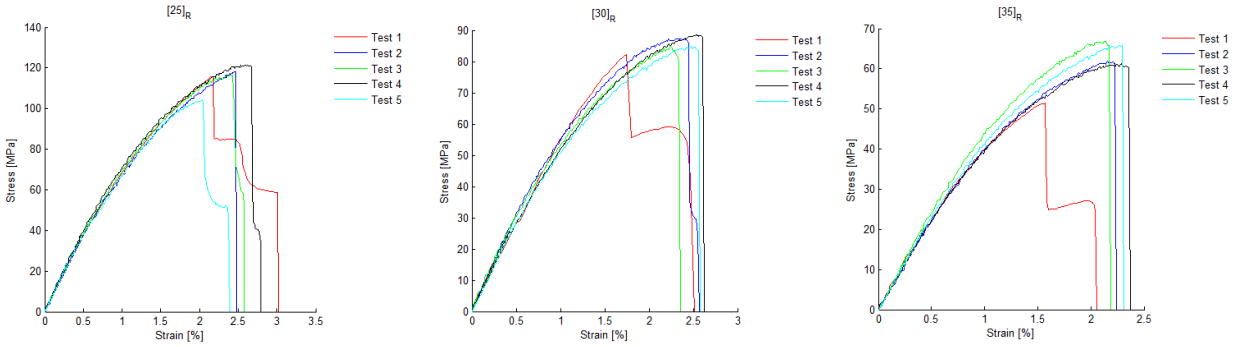

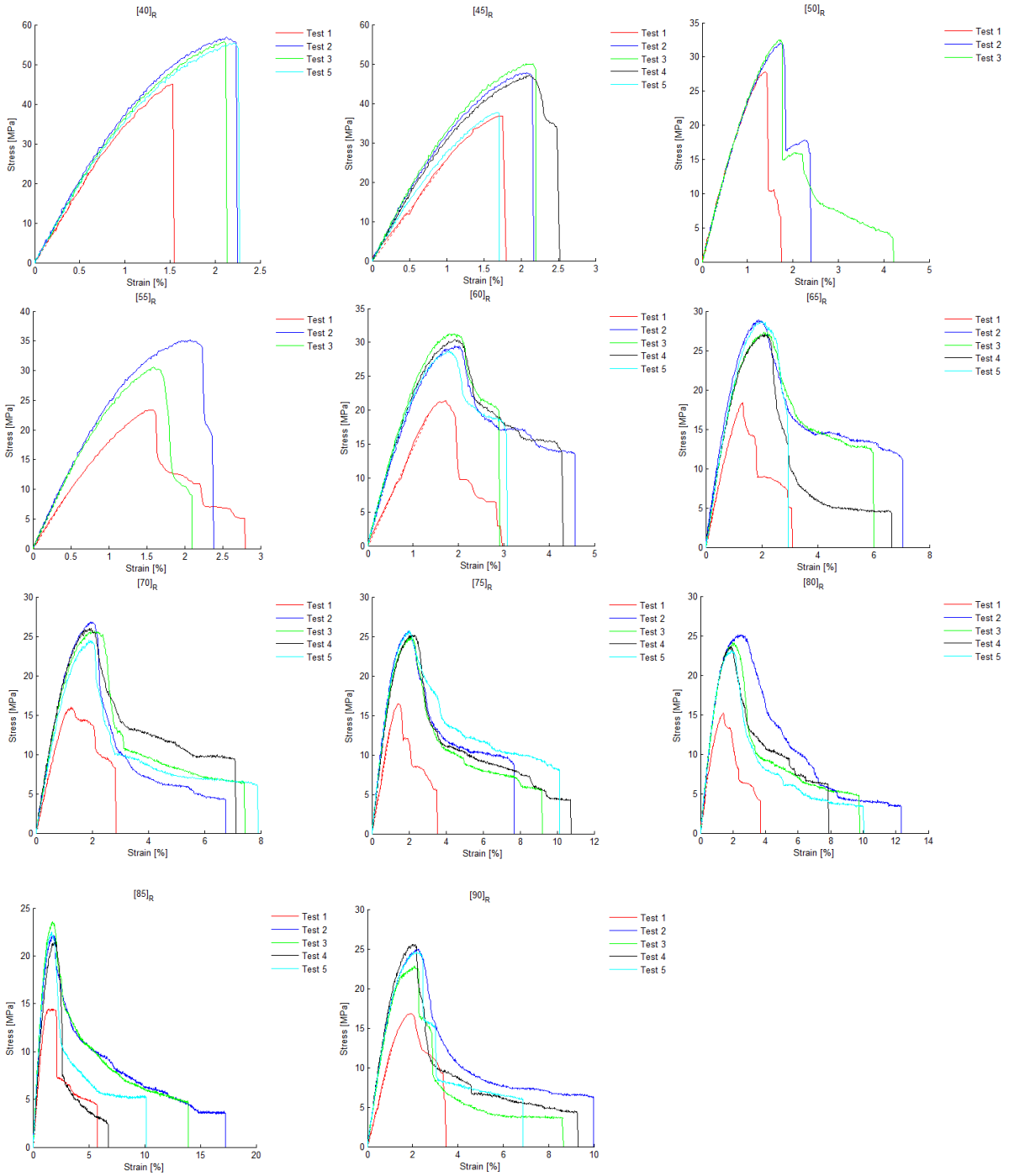

Figure A-13: Stress vs Strain Graphs of $[25]_R$ – $[90]_R$

From the above figures it is clear that the strength of the specimen reduced as the angle increased. Note that test 1's (red) results do not match with the other results, and this is simply due to the incorrect test rate (see subsection A.1.1.1). Furthermore, it is evident that from the $[60]_R$ combination onward the nylon is responsible for the high strain rate and hence the ductility of the specimen. The last 10 angles show a converging result towards the final angle's ($[90]_R$) results.

Only the latter specimen's zoomed graph and final appearance are shown as all the other orientations have a similar appearance, with only the magnitude and angle from which the strands sheared from one another being different.

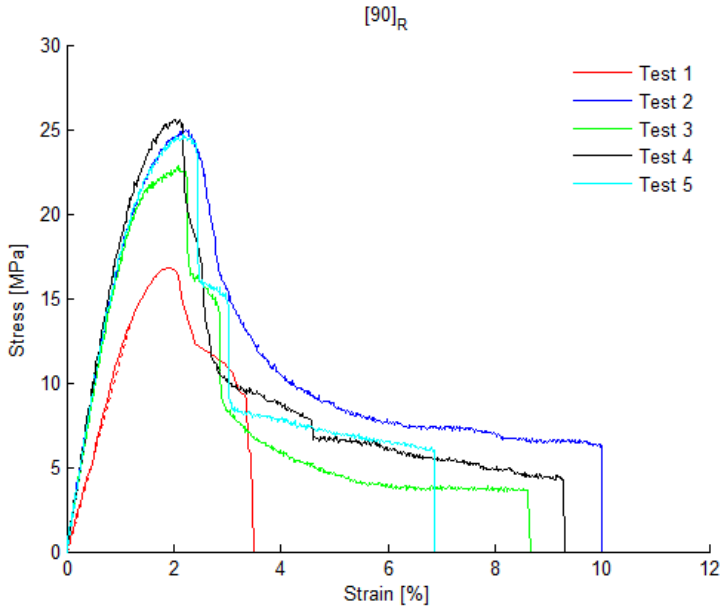

Figure A-14: Zoomed in Stress vs Strain Graph of $[90]_R$ layout combination

It is clear from Figure A-14 that the material most definitely has a linear region (modulus of elasticity) up until about 1% strain. The specimen did not break suddenly and has a large plastic region which indicates that the material behaves like a ductile material when approaching larger angles. Again, the nylon plays a big role in the material's behaviour. The following specimen is test 3 from the $[90]_R$ group.

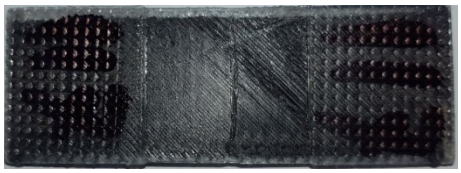

Figure A-15: Breakage of $[90]_R$ – Test 3

The specimen completely broke internally (where the carbon fibre strands are laid) and not on the sides where the nylon is situated. As opposed to the remarks on the $[0]_R$ strength, this orientation shows the maximum perpendicular strength between two adjacent strands, in other words, the bonding force between the strands during printing. This strength together with the UTS of the $[0]_R$ can be combined to obtain all other unidirectional angle strengths (see Chapter 7).

A.1.6.2 SEM Pictures of $[45]_R$ and $[90]_R$ Breakage

The SEM pictures of the $[45]_R$ and the $[90]_R$ are shown and discussed below respectively.

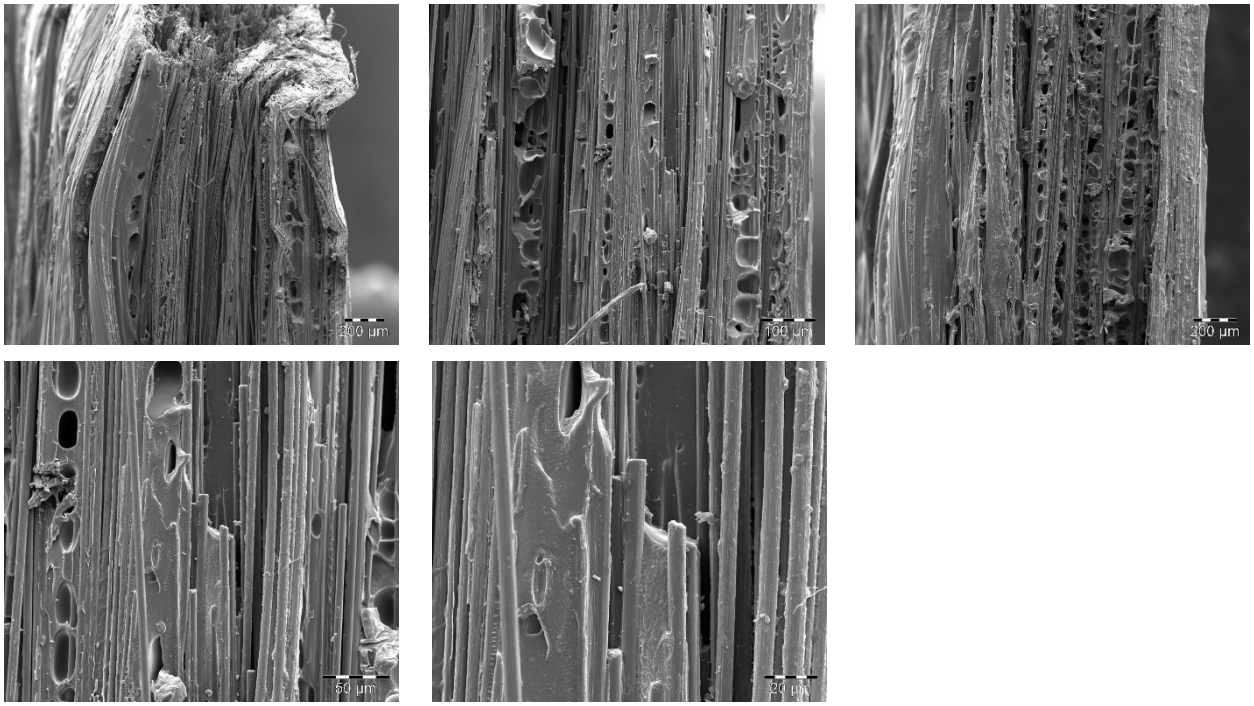

Figure A-16: SEM pictures of $[45]_R$ breakage [10]

The figures in A-16 show that the strands did shear from one another with minimum breakage within the strands themselves. It is also evident that each strand within the CFF filament consists of multiple other continuous strands. The voids within the resin can also be observed and contribute towards weak points within the specimen. Unfortunately, these voids cannot be controlled during the printing process.

Almost no strand breakage can be observed when the $[90]_R$ specimen is inspected (see figures below). Only strands tearing from one another can be seen. This further proves the point that the strands should be in the direction of the force for maximum strength.

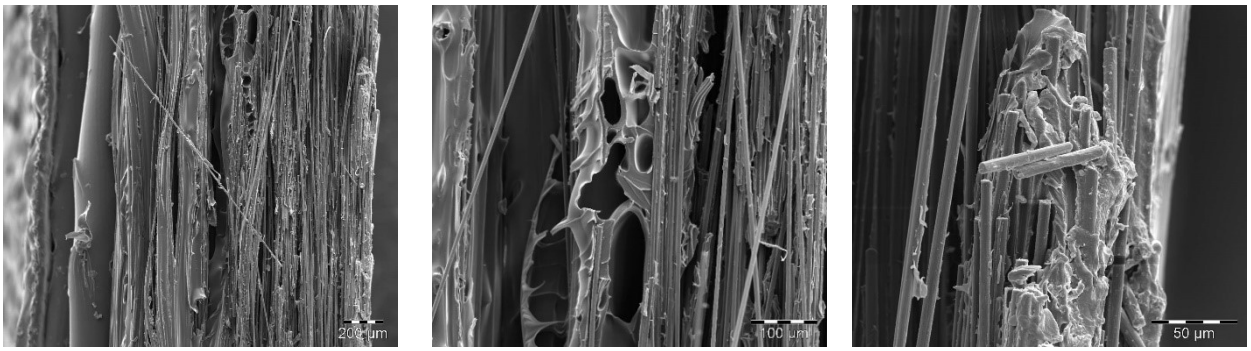

Figure A-17: SEM pictures of $[90]_R$ Breakage

A.1.6.3 Material properties of $[25]_R$ to $[90]_R$

All previous fourteen specimens' results are tabulated and can be seen below:

Table A-6: Material Properties of $[25]_R$ to $[90]_R$

Material Parameter		Value														Unit
		25	30	35	40	45	50	55	60	65	70	75	80	85	90	
E	Max	8	6	5	4	4	3	3	3	2	2	2	2	2	2	[GPa]
	Mean	8	6	5	4	3	3	2	2	2	2	2	2	2	2	[GPa]
	Min	7	6	4	4	3	3	2	2	2	2	2	2	2	2	[GPa]
YS	Max	40	30	24	22	18	17	15	13	12	10	10	10	11	11	[MPa]
	Mean	35	28	22	20	17	15	13	12	11	10	10	9	10	9	[MPa]
	Min	32	26	21	18	15	14	11	10	10	9	9	7	8	8	[MPa]
UTS	Max	121	89	67	57	50	33	35	31	29	27	26	25	24	26	[MPa]
	Mean	115	86	61	53	44	31	30	30	28	26	25	24	22	25	[MPa]
	Min	104	85	51	45	37	28	23	29	27	24	25	23	22	23	[MPa]
ε	Max	3	3	2	2	3	4	3	5	7	8	11	12	17	10	[%]
	Mean	3	3	2	2	2	3	2	4	5	6	8	9	11	8	[%]
	Min	2	2	2	2	2	2	2	3	3	3	4	4	6	3	[%]

A.2 90° Combination

The next layout category discussed is that of the 90° combinations, where each successive layer is offset by 90° from the previous one. Again, the intervals were at 5° until the layout repeated itself. Thus, only 10 possible combinations could be constructed. Furthermore, the same test procedure and data analysis method were used as discussed under Section A.1.1.

A.2.1 $[0/90]_R$

The first orientation combination discussed is the layout in which four of the eight layers are orientated just like the $[0]_R$ combination and the other four the same as the $[90]_R$ combination. From the results of the unidirectional layouts this combination was expected to have the highest UTS within this category for the fact that the dependent layers are those with an angle closest to 0°.

A.2.1.1 Stress-vs-Strain Graph of $[0/-90]_R$

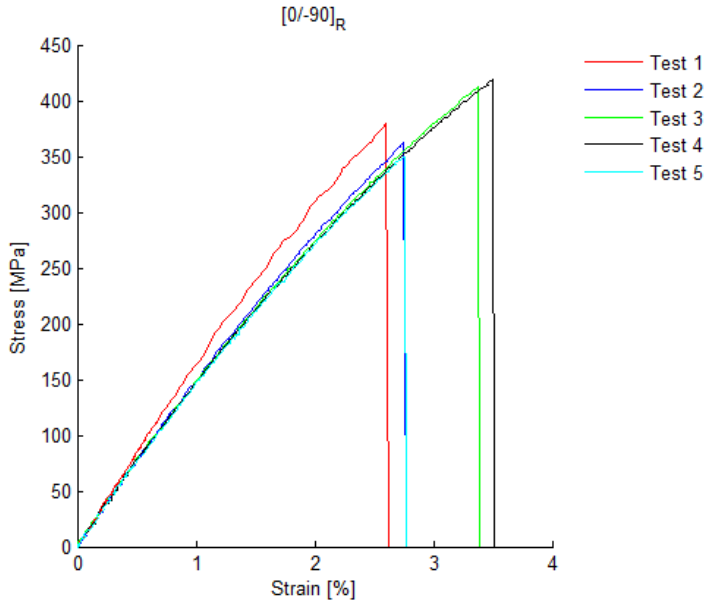

Figure A-18: Stress vs Strain Graph of $[0/-90]_R$

From Figure A-18 it is clear that the specimen exhibited a brittle behaviour. Again, test 1 is the odd one out in terms of the modulus of elasticity. Note that, unlike the $[0]_R$ combination, this graph shows a larger percentage of linear behaviour. It is only at up to about 60-70% of the total strain that the specimen tended to act as a non-linear material (compared that to 25% of the $[0]_R$ – see Section A.1.1).

As usual, a final appearance of a specimen (in this case, test 5) can be seen in Figure A-19 below. Once more, the specimen did not break into two parts but was taken apart afterwards for visual inspection. All eight layers are nearly distinguishable when examining the left side of the figure. This result is virtually a combination of the $[0]_R$ and $[90]_R$ final appearances with no breakage angle between 0° and 90°. Furthermore, observe the nylon on both sides of the specimen.

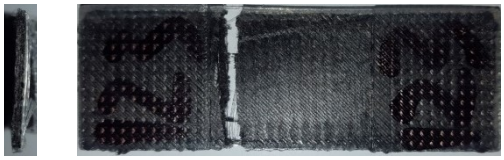

Figure A-19: Breakage of $[0/-90]_R$ – Test 5

A.2.1.2 Material properties of $[0/-90]_R$

Table A-7: Material Properteis of $[0/-90]_R$

Material parameter	Value		Unit
Modulus of elasticity ($E_{[0/-90]R}$)	Max	15.18	[GPa]
	Mean	15.00	[GPa]
	Min	14.75	[GPa]
Yield strength ($YS_{[0/-90]R}$)	Max	121.84	[MPa]
	Mean	98.55	[MPa]
	Min	81.67	[MPa]
Ultimate tensile strength ($UTS_{[0/-90]R}$)	Max	418.91	[MPa]
	Mean	385.77	[MPa]
	Min	349.81	[MPa]
Strain ($\varepsilon_{[0/-90]R}$)	Max	3.51	[%]
	Mean	3.02	[%]
	Min	2.63	[%]

A.2.2 $[5/-85]_R$

The next combination of orientations is that of 5° and -85°. The reason for the negative degree is the fact that 95° is the same as -85°. From previous results it can be assumed that the stress-vs-strain graph will look similar to the one for $[0/-90]_R$, as the dependable strands are only 5° from 0°.

A.2.2.1 Stress-vs-Strain Graph of $[5/-85]_R$

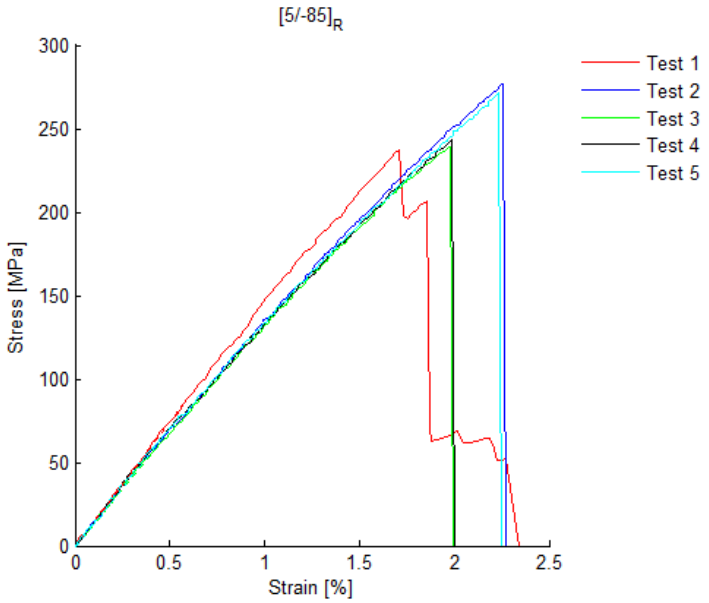

Figure A-20: Stress vs Strain Graph of $[5/-85]_R$

As expected, the specimens displayed similar behaviour as the previous combination of layers. Notice the linearity, brittleness, and sudden breakage in the graph. This shows that as soon as one 5° layer tears of its adjacent strands, the whole specimen fails.

From the visual presentation of the specimen after the experiment (see Figure A-21 below), one can clearly see that the specimen broke at the location with the least amount of carbon fibre per width. This location demonstrates that the specimen fails as soon as the tensile force exceeds the adhesion force between the strands.

Figure A-21: Breakage of $[5/-85]_R$ – Test 5

A.2.2.2 Material properties of $[5/-85]_R$

Table A-8: Material Properties of $[5/-85]_R$

Material parameter	Value		Unit
Modulus of elasticity ($E_{[5/-85]R}$)	Max	14.19	[GPa]
	Mean	14.04	[GPa]
	Min	13.67	[GPa]
Yield strength ($YS_{[5/-85]R}$)	Max	77.84	[MPa]
	Mean	70.30	[MPa]
	Min	61.90	[MPa]
Ultimate tensile strength ($UTS_{[5/-85]R}$)	Max	277.16	[MPa]
	Mean	257.81	[MPa]
	Min	239.19	[MPa]
Strain ($\varepsilon_{[5/-85]R}$)	Max	2.34	[%]
	Mean	2.17	[%]
	Min	1.99	[%]

A.2.3 $[10/-80]_R$

From this combination of layer orientations and onward, the influence of the nylon and weaker angles (the ones closest to 90°) can be observed and increased as the combinations approach the $[45/-45]_R$ category.

A.2.3.1 Stress-vs-Strain Graph of $[10/-80]_R$

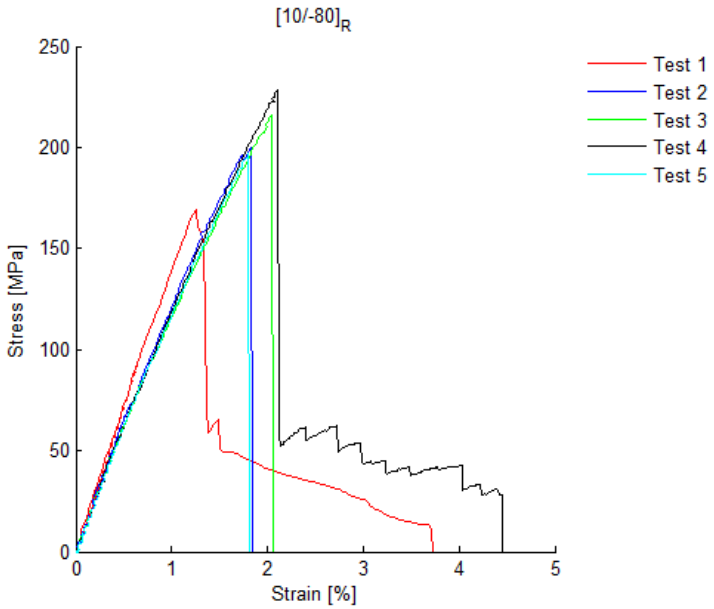

Figure A-22: Stress vs Strain of $[10/-80]_R$

Once more, test 1 (red) is the odd one out and it is only displayed to show the importance of the correct test speed. Figure A-22 shows how the linearity of the specimen begins to diverge from linear to non-linear when compared with the previous two stress-vs-strain graphs. It is also evident that after test 4 had broken, it still had a few strands that kept the specimen intact before breaking completely. The spikes can be explained as the individual carbon fibre strands that tore from one another in sequence.

The final appearance of a specimen shows a clear break at the most desired location (in the middle of the gauge length). It is also evident that the failure type in the specimen begins to tend towards a more lateral behaviour than an angled type for most of the previous specimens (please refer to a chart of typical failure modes in tensile tests of composites). This can be attributed to the fact that the dependent layers (the one with the closest angle to 0°) start to have a lesser influence while the independent layers (those closest to 90°) start to have a higher influence as they approach an angle closer to 0°.

Figure A-23: Breakage of $[10/-80]_R$ – Test 4

A.2.3.2 Material properties of $[10/-80]_R$

Table A-9: Material Properties of $[10/-80]_R$

Material parameter	Value		Unit
Modulus of elasticity ($E_{[10/-80]R}$)	Max	13.46	[GPa]
	Mean	13.13	[GPa]
	Min	12.83	[GPa]
Yield strength ($YS_{[10/-80]R}$)	Max	68.27	[MPa]
	Mean	62.27	[MPa]
	Min	56.28	[MPa]
Ultimate tensile strength ($UTS_{[10/-80]R}$)	Max	228.68	[MPa]
	Mean	210.35	[MPa]
	Min	197.09	[MPa]
Strain ($\varepsilon_{[10/-80]R}$)	Max	4.47	[%]
	Mean	2.78	[%]
	Min	1.82	[%]

A.2.4 $[15/-75]_R$

The 90° combinations made for interesting results, with this specific orientation not being any different. This whole layout category displays a trend towards the final $[45/-45]_R$ result.

A.2.4.1 Stress-vs-Strain Graph of $[15/-75]_R$

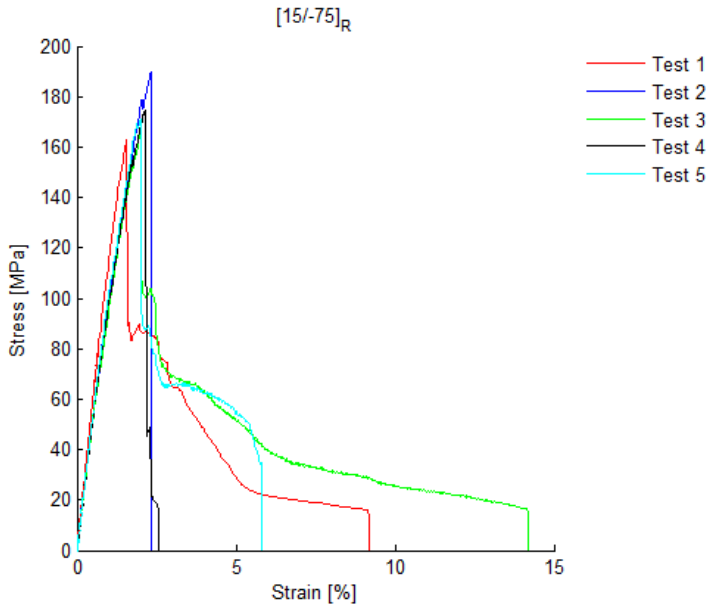

Figure A-24: Stress vs Strain Graph of $[15/-75]_R$

It is clear from the Figure A-24 above that three of the tests had a large non-uniform plastic deformation region. This phenomenon already started with the previous layout and will increase as the layouts approach $[45/-45]_R$. This can easily be explained when Figure A-1 and Figure A-14

are examined simultaneously. The above figure is basically a combination of the latter two figures. It is expected that the specimens' plastic region will increase.

Notice how, when test 1 is disregarded, two out of the remaining four tests have little to no plastic regions, while the other two have plastic regions. The reason is the same as under subsection A.1.4.1. The difference between these two situations can also clearly be seen in the next final appearance of each. The top specimen is test 3 which had an lateral inside grip/tap (LI) failure, while the bottom one is test 2 which had a Grip/tap at grip/tab (GA) failure.

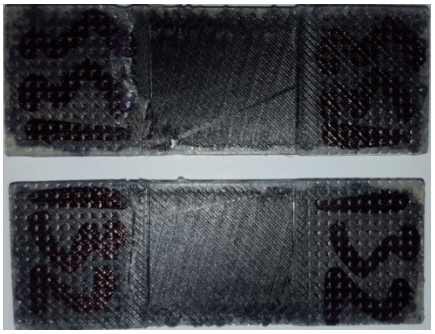

Figure A-25: Breakage of $[15/-75]_R$ – Test 3 (top) and Test 2 (bottom)

A.2.4.2 Material properties of $[15/-75]_R$

Table A-10: Material Properties of [15/-75]R

Material parameter	Value		Unit
Modulus of elasticity ($E_{[15/-75]R}$)	Max	10.82	[GPa]
	Mean	10.59	[GPa]
	Min	10.29	[GPa]
Yield strength ($YS_{[15/-75]R}$)	Max	57.03	[MPa]
	Mean	53.43	[MPa]
	Min	47.53	[MPa]
Ultimate tensile strength ($UTS_{[15/-75]R}$)	Max	189.58	[MPa]
	Mean	175.14	[MPa]
	Min	165.23	[MPa]
Strain ($\varepsilon_{[15/-75]R}$)	Max	14.20	[%]
	Mean	6.82	[%]
	Min	2.35	[%]

A.2.5 $[20/-70]_R$ – $[45/-45]_R$

Just like under subsection A.1.6.1, the last six layout combinations within the 90° combination category are summarised as a group with discussions to follow.

A.2.5.1 Stress-vs-Strain Graphs of $[20/-70]_R$ – $[45/-45]_R$

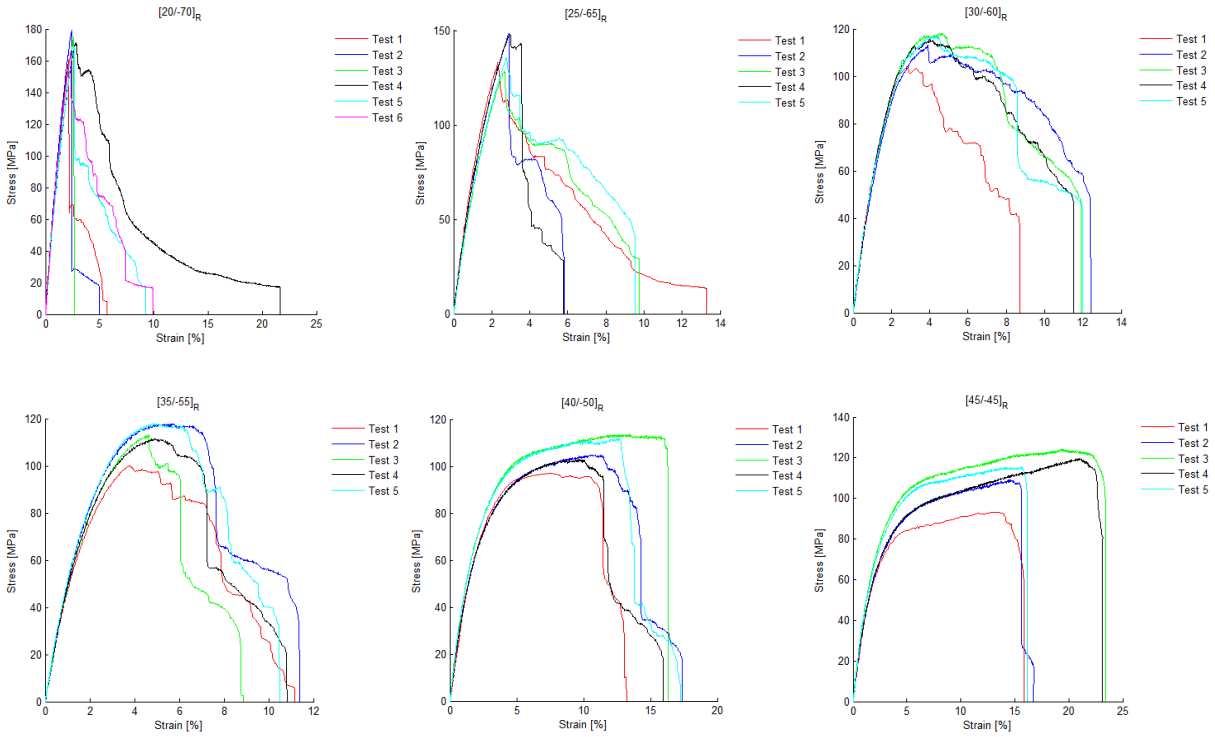

Figure A-26: Stress vs Strain Graphs of $[20/-70]_R$ to $[45/-45]_R$

From Figure A-26 above it is clear that the linearity decreased while the elastic region increased. The UTS decreased up until the second last combination before increasing at the last combination. The UTS position in respect of the strain moved more to the right side, producing an interesting uniform plastic deformation region change from the first up to the last figure with no pattern.

In the $[20/-70]_R$ and $[25/-65]_R$ can be seen that within this plastic region are still some remaining strands tearing from one another in segments, with only the magnitude differing between the two. Furthermore, both graphs show that the specimens' type of failure as a combination of brittleness and ductility. From $[30/-60]_R$ to $[35/-55]_R$ the amount of major adjacent strand tearing is limited to only one, while the plastic region decreases. Here the specimens tend to fail in more of a ductile manner than a brittle manner. During the last two figures, one can see that the possibility for tearing of strands within the plastic region is still there, but the overall plastic region dramatically decreases due to the fact that the specimens seem to break a bit more brittlely than ductile once the maximum strain has been reached. The corresponding final appearance of each category is displayed below and shortly discussed:

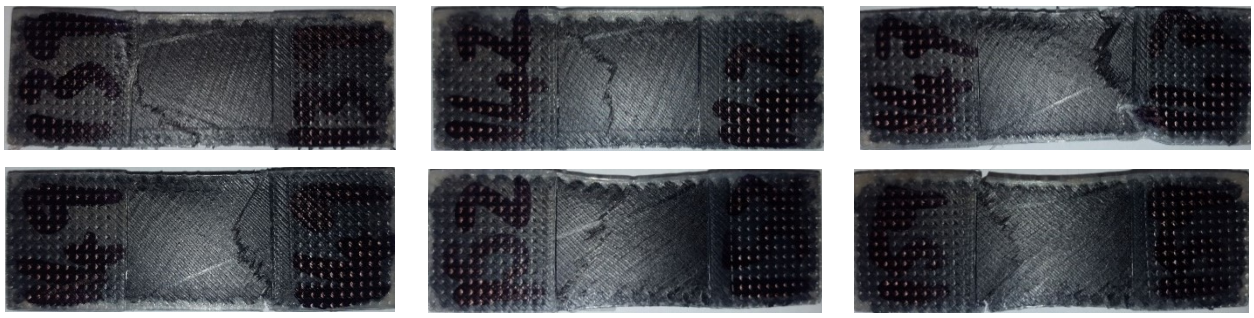

Figure A-27: Breakage of $[20/-70]_R$ to $[45/-45]_R$

When Figure A-26 is compared with Figure A-27 above a few conclusions can be drawn. All six specimens had a more angled type of failure and either at the gage or at the grip. Observe how the breakage angles are basically divided into two parts, showing that all the layers played a role in the final failure. It is also interesting to see that as the orientations approached the $[45/-45]_R$ category, the width of the specimens became narrower, as expected.

A.2.5.2 Material properties of $[20/-70]_R$ to $[45/-45]_R$

All six specimens' results are tabulated in Table A-11 below:

Table A-11: Material properties of $[20/-70]_R$ to $[45/-45]_R$

Material parameter		Value						Unit
		[20/-70]	[25/-65]	[30/-60]	[35/-55]	[40/-50]	[45/-45]	
E	Max	9.6	7.9	6.1	5.6	4.8	4.7	[GPa]
	Mean	9.2	7.5	6.0	5.3	4.5	4.3	[GPa]
	Min	8.7	7.1	5.9	5.2	4.3	3.9	[GPa]
YS	Max	52.5	47.0	37.9	32.4	28.1	26.1	[MPa]
	Mean	44.8	38.7	30.9	28.1	24.1	22.5	[MPa]
	Min	37.8	33.0	24.8	23.6	22.2	18.4	[MPa]
UTS	Max	179.2	148.3	118.1	118.0	113.8	124.3	[MPa]
	Mean	170.2	138.6	115.9	112.1	108.4	112.4	[MPa]
	Min	160.3	128.2	113.1	100.2	103.0	93.3	[MPa]
ε	Max	21.6	13.3	12.4	11.4	17.4	23.4	[%]
	Mean	8.8	8.8	11.3	10.6	16.0	19.1	[%]
	Min	2.6	5.8	8.7	8.9	13.2	15.9	[%]

A.3 45° Combination

The second last category discussed is that of the 45° combinations. The results are expected to commensurate as the preceding and succeeding layers' angles approach each other. In this category are six different layouts, with the last two basically being almost the same.

A.3.1 $[0/45/-90/-45]_R$

In this layout combination are two layers of which the strands are 0°, and because of this these specimens are expected to be the strongest within this category. Notice the naming of the orientations – the negative 90° could have also been positive 90° and only serves a symmetrical purpose.

A.3.1.1 Stress-vs-Strain Graph of $[0/45/-90/-45]_R$

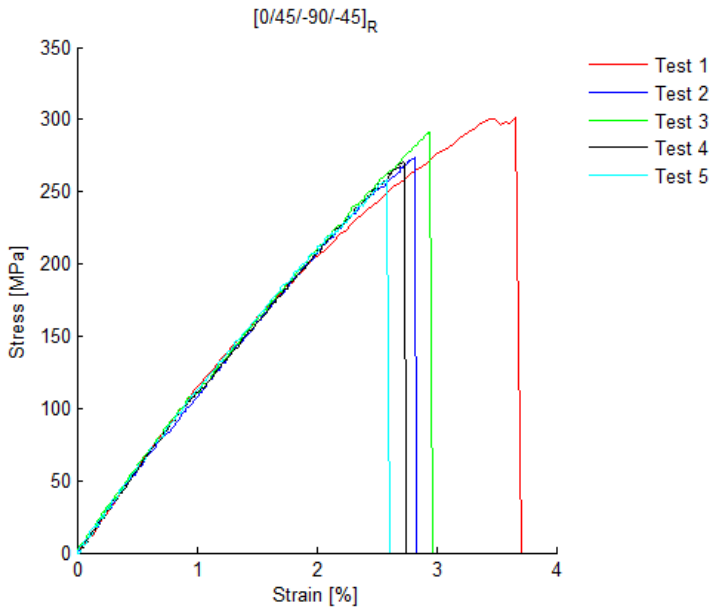

Figure A-28: Stress vs Strain of $[0/45/-90/-45]_R$

From Figure A-28 above test 1 is yet again observed to be the odd one out, and the reason for this is discussed under subsection A.1.1.1. All five specimens broke in a brittle manner as expected due to the fact that the nylon (the more ductile material) and the independent angles (those closest to 90°) begin to have less of an impact on the overall strength of the specimen. Notice the linearity of the graph – it shows more linearity than the $[0/90]_R$ combination (see Section A.2.1). This occurrence is evident from the remaining five tests within this category and are henceforth only summarised under Section A.3.2. The final appearances of the specimens are similar to the last specimens within the $[90]_R$ combination category.

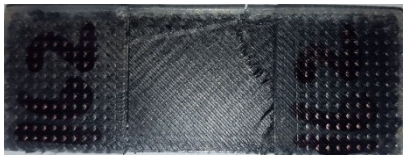

Figure A-29: Breakage of $[0/45/-90/-45]_R$

A.3.1.2 Material properties of $[0/45/-90/-45]_R$

Table A-12: Material Properties of $[0/45/-90/-45]_R$

Material parameter	Value		Unit
Modulus of elasticity ($E_{[0/45/-90/-45]R}$)	Max	11.78	[GPa]
	Mean	11.65	[GPa]
	Min	11.50	[GPa]
Yield strength ($YS_{[0/45/-90/-45]R}$)	Max	77.22	[MPa]
	Mean	70.05	[MPa]
	Min	62.18	[MPa]
Ultimate tensile strength ($UTS_{[0/45/-90/-45]R}$)	Max	291.17	[MPa]
	Mean	273.61	[MPa]
	Min	258.76	[MPa]
Strain ($\varepsilon_{[0/45/-90/-45]R}$)	Max	3.71	[%]
	Mean	2.97	[%]
	Min	2.61	[%]

A.3.2 $[5/50/-85/-40]_R$ – $[25/70/-65/-20]_R$

As mentioned in the previous section, all six different layout combinations within the 45° combination category had similar results and therefore only a summarised presentation is shown with a discussion to follow.

A.3.2.1 Stress-vs-Strain Graphs of $[5/50/-85/-40]_R$ to $[25/70/-65/-20]_R$

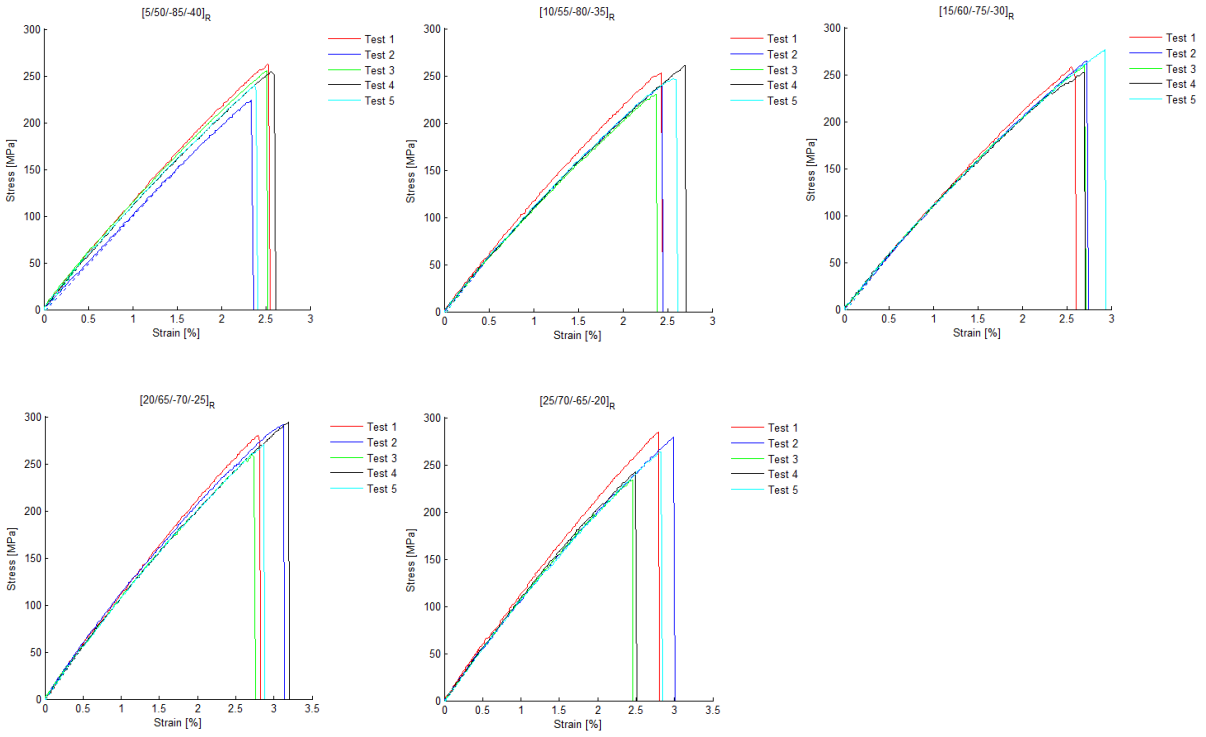

Figure A-30: Stress vs Strain of $[5/50/-85/40]_R$ to $[25/70/-65/-20]_R$

It is clear from Figure A-28 and Figure A-30 that all specimens behaved likewise. Notice the brittleness and linearity of all graphs. The final appearances of the specimens can be seen below. Notice the good failure area of all specimens (all at the gage). This shows that the dimensions of the specimens can be considered to be correct for all testing purposes.

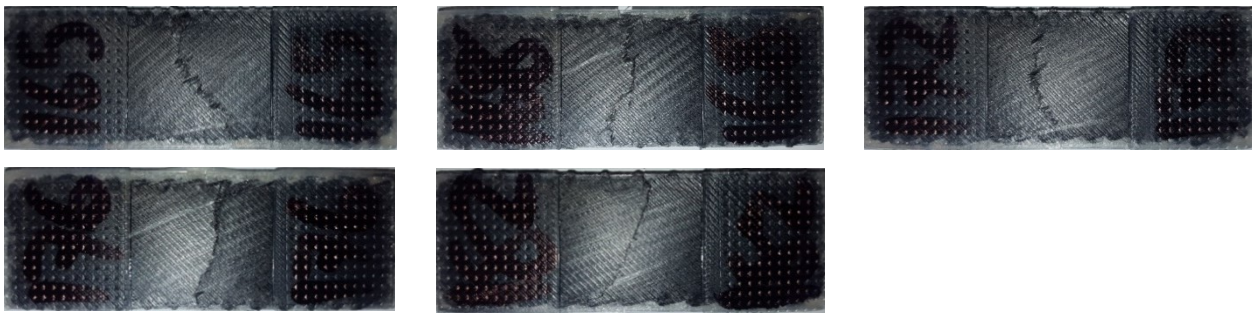

Figure A-31: Breakage of $[5/50/-85/40]_R$ to $[25/70/-65/-20]_R$

A.3.2.2 Material properties of $[5/50/-85/40]_R$ to $[25/70/-65/-20]_R$

Again, all the remaining five specimens' material properties are tabulated in Table A-13 below.

Table A-13: Material properties of $[5/50/-85/40]_R$ to $[25/70/-65/-20]_R$

Material parameter		Value					Unit
		[5/50/-85/-40]	[10/55/-80/-35]	[15/60/-75/-30]	[20/65/-70/-25]	[25/70/-65/-20]	
E	Max	12.0	11.8	11.7	11.4	11.9	[GPa]
	Mean	11.9	11.6	11.6	11.3	11.6	[GPa]
	Min	11.7	11.4	11.4	11.3	11.3	[GPa]
YS	Max	59.8	52.4	61.2	53.7	67.6	[MPa]
	Mean	56.9	51.9	56.5	50.8	59.9	[MPa]
	Min	51.4	51.6	54.8	48.0	53.9	[MPa]
UTS	Max	262.6	261.2	276.5	279.6	294.6	[MPa]
	Mean	253.4	244.5	262.3	254.8	279.2	[MPa]
	Min	240.5	230.2	252.5	233.9	259.1	[MPa]
ε	Max	2.6	2.7	2.9	3.0	3.2	[%]
	Mean	2.5	2.5	2.7	2.7	3.0	[%]
	Min	2.4	2.4	2.6	2.5	2.8	[%]

A.4 30° Combination

The last category discussed is that of the 30° combination. After examining the 45° combination category's results, all four layout combinations within this category are expected to have similar

stress-vs-strain graphs. However, there is a slight difference in the last two graphs and this variance is addressed accordingly.

A.4.1 $[0/30/60/-90/-60/-30]_R$

The previous three combination categories (unidirectional, 90°, and 45°) all had a symmetric aspect within the eight layers of carbon fibre. In this particular case, the symmetrical occurrence does not exist because of the complete circuit of succeeding angled layers being six layers and not four, two, or one as in the cases of the 45°, 90°, and unidirectional layouts respectively. This means that only the first two layers will repeat themselves.

A.4.1.1 Stress-vs-Strain Graph of $[0/30/60/-90/-60/-30]_R$

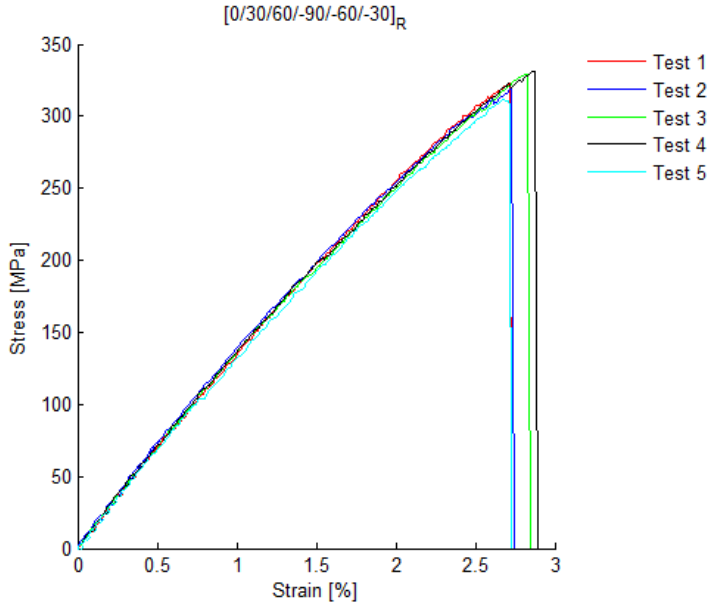

Figure A-32: Stress vs Strain of $[0/30/60/-90/-60/-30]_R$

The precision in the above graph is magnificent. Notice the linearity up until just before the UTS. The specimens had a brittle failure, and this is also true for the remaining three layouts. It was again expected that this combination of layers would have the highest UTS due to the two layers that are 0°-orientated. The final appearance of test 2 can be seen below. Notice the failure type and also the similarity between this specimen and that of the $[0/90]_R$ and $[0/45/-90/-45]_R$.

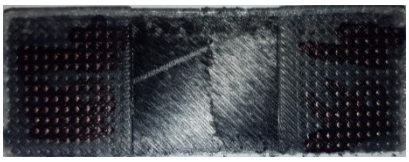

Figure A-33: Breakage of $[0/30/60/-90/-60/-30]_R$ – Test 2

A.4.1.2 Material properties of $[0/30/60/-90/-60/-30]_R$

Table A-14: Material Properties of $[0/30/60/-90/-60/-30]_R$

Material parameter	Value		Unit
Modulus of elasticity ($E_{[0/30/60/-90/-60/-30]R}$)	Max	14.37	[GPa]
	Mean	14.22	[GPa]
	Min	14.00	[GPa]
Yield strength ($YS_{[0/30/60/-90/-60/-30]R}$)	Max	82.28	[MPa]
	Mean	71.87	[MPa]
	Min	62.71	[MPa]
Ultimate tensile strength ($UTS_{[0/30/60/-90/-60/-30]R}$)	Max	331.10	[MPa]
	Mean	322.87	[MPa]
	Min	312.05	[MPa]
Strain ($\varepsilon_{[0/30/60/-90/-60/-30]R}$)	Max	2.89	[%]
	Mean	2.79	[%]
	Min	2.72	[%]

A.4.2 $[5/35/65/-85/-55/-25]_R$ – $[15/45/15/-75/-45/-15]_R$

The likeness between the last three layout combinations is clear and are therefore only summarised.

A.4.2.1 Stress-vs-Strain Graphs of $[5/35/65/-85/-55/-25]_R$ – $[15/45/15/-75/-45/-15]_R$

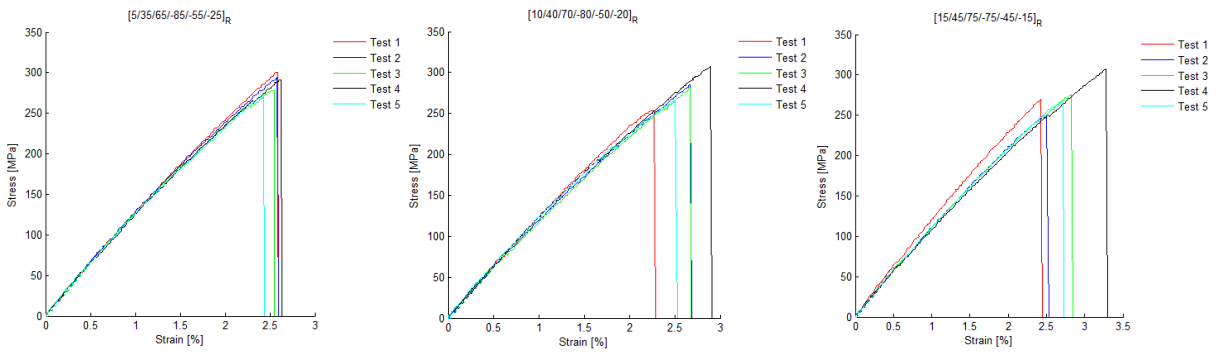

Figure A-34: Stress vs Strain Graphs of $[5/35/65/-85/-55/-25]_R$ – $[15/45/15/-75/-45/-15]_R$

Notice the slight imprecision of the strain at which the specimens broke in the last two graphs. This is ascribed to the closest layout orientation to 0° being only 10° and 15° compared to the first two which are at 0° itself and 5°. The final appearances can once again be seen below. Notice how the failure area starts at the middle (with the first layout combination – $[0/30/60/-90/-60/-30]_R$) and tends towards the grip as it approaches the last layout combination.

Figure A-35: Breakage of $[5/35/65/-85/-55/-25]_R$ – $[15/45/15/-75/-45/-15]_R$

A.4.2.2 Material Properties of $[5/35/65/-85/-55/-25]_R$ – $[15/45/15/-75/-45/-15]_R$

Table A-15: Material Properties of $[5/35/65/-85/-55/-25]_R$ – $[15/45/15/-75/-45/-15]_R$

Material parameter		Value			Unit
		[5/35/65/-85/-55/-25]	[10/40/70/-80/-50/-20]	[15/15/75/-75/-45/-35]	
E	Max	13.4	13.0	12.7	[GPa]
	Mean	13.2	12.7	11.9	[GPa]
	Min	13.0	12.4	11.6	[GPa]
YS	Max	89.8	75.0	67.2	[MPa]
	Mean	76.1	65.0	61.5	[MPa]
	Min	62.1	53.0	52.8	[MPa]
UTS	Max	300.4	284.8	275.6	[MPa]
	Mean	287.5	271.2	265.5	[MPa]
	Min	273.4	253.7	249.8	[MPa]
ε	Max	2.6	2.9	3.3	[%]
	Mean	2.6	2.6	2.8	[%]
	Min	2.4	2.3	2.4	[%]

APPENDIX B – VERIFICATION OF MODEL

Appendix B shows all the proposed mathematical model's values in terms of tables and this acts as the verification purpose of the model. The summary of this section can be seen under Section 7.2.

Table B-1: Mathematical Model Unidirectional Results

Unidirectional							
Degrees		Ratios		Theo Value	True Value	cftool in MATLAB® Values	% Error
α	β	Aα	Bβ				
0	90	0.99996	0.00004	768.57	624.60	624.29	0.05
5	85	0.71027	0.28973	544.34	445.22	446.73	0.34
10	80	0.50500	0.49500	383.95	316.91	320.63	1.16
15	75	0.35960	0.64040	270.26	225.96	231.14	2.24
20	70	0.25669	0.74331	190.44	162.10	167.70	3.34
25	65	0.18393	0.81607	134.96	117.72	122.79	4.13
30	60	0.13256	0.86744	96.84	87.23	91.09	4.24
35	55	0.09641	0.90359	70.98	66.54	68.79	3.27
40	50	0.07107	0.92893	53.69	52.71	53.19	0.91
45	45	0.05344	0.94656	42.33	43.61	42.38	2.91
50	40	0.04132	0.95868	34.99	37.74	34.99	7.87
55	35	0.03316	0.96684	30.33	34.02	30.05	13.19
60	30	0.02785	0.97215	27.41	31.68	26.88	17.83
65	25	0.02462	0.97538	25.54	30.18	24.99	20.76
70	20	0.02295	0.97705	24.25	29.15	24.04	21.27
75	15	0.02244	0.97756	23.20	28.31	23.77	19.11
80	10	0.02285	0.97715	22.14	27.47	24.02	14.35
85	5	0.02401	0.97599	20.90	26.47	24.67	7.32
90	0	0.02581	0.97419	19.33	25.21	25.63	1.61
						Average % Error:	7.68

Table B-2: Mathematical Model 90° Combination Results

90° Combination									
Degrees				Ratios		Theo Value	True Value	Expr UTS (MPa)	% Error
α	α'	β	β'	Aα	Bβ				
0	90	90	0	0.52415	0.47585	412.30	291.12	385.00	24.38
5	85	85	5	0.40122	0.59878	346.95	247.55	261.68	5.40
10	80	80	10	0.31134	0.68866	293.04	211.61	206.82	2.32
15	75	75	15	0.24923	0.75077	252.85	184.82	177.53	4.11
20	70	70	20	0.20621	0.79379	223.33	165.14	158.27	4.34
25	65	65	25	0.17501	0.82499	200.51	149.93	143.37	4.58
30	60	60	30	0.15060	0.84940	181.14	137.01	130.70	4.83
35	55	55	35	0.13014	0.86986	163.34	125.15	119.47	4.76
40	50	50	40	0.11262	0.88738	146.75	114.09	109.30	4.38
45	45	45	45	0.09852	0.90148	132.38	104.50	100.05	4.45
								Average % Error:	6.35

Table B-3: Mathematical Model 75° Combination Results

75° Combination									
Degrees				Ratios		Theo Value	True Value	Expr UTS (MPa)	% Error
α	α'	β	β'	Aα	Bβ				
0	75	90	15	0.46522	0.53478	460.36	306.01	302.98	1.00
5	80	85	10	0.35684	0.64316	334.53	227.37		
10	85	80	5	0.28562	0.71438	251.91	175.73		
15	90	75	0	0.23967	0.76033	196.92	141.36		
20	85	70	5	0.20954	0.79046	186.36	134.76	166.80	19.21
25	80	65	10	0.18878	0.81122	179.35	130.38		
30	75	60	15	0.17344	0.82656	173.99	127.03		
35	70	55	20	0.16179	0.83821	169.56	124.26		
40	65	50	25	0.15430	0.84570	166.96	122.63	141.60	13.40
								Average % Error:	10.10

Table B-4: Mathematical Model 60° Combination Results

60° Combination									
Degrees				Ratios		Theo Value	True Value	Expr UTS (MPa)	% Error
α	α'	β	β'	Aα	Bβ				
0	60	90	30	0.41710	0.58290	490.89	301.41	317.35	5.02
5	65	85	25	0.33627	0.66373	379.78	237.92		
10	70	80	20	0.28705	0.71295	308.48	197.17		
15	75	75	15	0.25825	0.74175	261.12	170.11	206.55	17.64
20	80	70	10	0.24230	0.75770	227.29	150.78		
25	85	65	5	0.23453	0.76547	200.63	135.54		
30	90	60	0	0.23281	0.76719	177.80	122.50	137.27	10.76
								Average % Error:	11.14

Table B-5: Mathematical Model 45° Combination Results

45° Combination											
Degrees						Ratios		Theo Value	True Value	Expr UTS (MPa)	% Error
α	α'	α''	β	β'	β''	Aα	Bβ				
0	45	90	90	45	0	0.39910	0.60090	544.00	296.38	275.36	7.63
5	50	85	85	50	5	0.34149	0.65851	475.61	262.18	253.88	3.27
10	55	80	80	55	10	0.31055	0.68945	437.10	242.93	242.93	0.00
15	60	75	75	60	15	0.29709	0.70291	417.89	233.32	263.39	11.42
20	65	70	70	65	20	0.29555	0.70445	410.98	229.87	276.24	16.79
25	70	65	65	70	25	0.30347	0.69653	412.84	230.80	256.96	10.18
										Average % Error:	8.21

Table B-6: Mathematical Model 30° Combination Results

30° Combination													
Degrees								Ratios		Theo Value	True Value	Expr UTS (MPa)	% Error
α	α'	α''	α'''	β	β'	β''	β'''	Aα	Bβ				
0	30	60	90	90	60	30	0	0.38434	0.61566	727.83	320.39	322.83	0.76
5	35	65	85	85	65	35	5	0.34737	0.65263	650.89	289.61	287.42	0.76
10	40	70	80	80	70	40	10	0.33236	0.66764	609.00	272.86	271.19	0.61
15	45	75	75	75	75	45	15	0.33244	0.66756	588.75	264.76	265.42	0.25
												Average % Error:	0.60

Table B-7: Mathematical Model 15° Combination Results

15° Combination																		
Degrees														Ratios		Theoretical Value	True Value	Expr UTS (MPa)	% Error
α	α'	α''	α'''	α''''	α'''''	α''''''	β	β'	β''	β'''	β''''	β'''''	β''''''	Aα	Bβ				
0	15	30	45	60	75	90	90	75	60	45	30	15	0	0.362	0.638	1 250	349	290	20.6
5	20	35	50	65	80	85	85	70	55	40	25	10	5	0.347	0.653	1 148	324		
10	25	40	55	70	85	80	80	65	50	35	20	5	10	0.349	0.651	1 091	309	252	22.9
																		Average % Error:	21.8